rijksuniversiteit groningen

Intrinsic and extrinsic size effects in metallic glasses

Proefschrift

ter verkrijging van de graad van doctor aan de
Rijksuniversiteit Groningen
op gezag van de
rector magnificus prof. dr. E. Sterken
en volgens besluit van het College voor Promoties.

De openbare verdediging zal plaatsvinden op

vrijdag 21 maart 2014 om 11.00 uur

door

Oleksii Volodymyrovych Kuzmin

geboren op 17 oktober 1986
te Lugansk, Oekraïne

Promotor

Prof. dr. J.Th.M. De Hosson

Copromotor

Prof. dr. Y.T. Pei

Beoordelingscommissie

Prof. dr P. Rudolf
Prof. dr. B. Noheda Pinuaga
Prof. dr. H.A. De Raedt

INTRINSIC AND EXTRINSIC SIZE EFFECTS IN METALLIC GLASSES

Oleksii Kuzmin

PhD thesis
University of Groningen

Zernike Institute PhD thesis series 2014-04
ISSN: ISSN 1570-1530
ISBN: 978-90-367-6859-7 (Printed version)
ISBN: 978-90-367-6858-0 (Electronic version)
Print: Groningen University Press

The research presented in this thesis was performed in the Materials Science group of the Zernike Institute for Advanced Materials at the University of Groningen, the Netherlands.

This work was funded by Foundation of Fundamental Research on Matter (FOM, Utrecht, The Netherlands), which is part of the Netherlands Organization for Scientific Research (NWO) in the framework of the Industrial Partnership Program on Size Dependent Material Properties of the Materials innovation institute (M2i , Delft, The Netherlands), project M62.7.08SDMP013.

university of groningen / faculty of mathematics and natural sciences / zernike insitute for advanced materials

CONTENTS

Chapter 1

Introduction

1.1 Introduction

As far as we know natural glass exists since the starting time of the earth and was formed from rapid solidification of molten rock produced during volcanic eruptions and meteorite impacts. Phoenician merchants were aware of its existence and man-made glass objects from Egypt and Eastern Mesopotamia date back to around 3500 BC.[1] On the other hand man-made metallic glass having an amorphous structure is much younger, i.e. about five decades and functional metallic glasses were realized only during the last decade. The term "amorphous" comes from Greek language (αμορφηουσ) and means "without regular form" [α = not, μορφη = form]. The atoms in an amorphous metal are therefore considered to be arranged without long range order.[2] A glass is any material that can be cooled from a liquid to a solid without crystallizing. Most metals do crystallize as they cool, arranging their atoms into a highly regular spatial pattern called a lattice. But if crystallization does not occur, and the atoms settle into a nearly random arrangement, the final form is a metallic glass.[3]

However, there are several other ways in which amorphous metals can be produced, including physical vapor deposition, solid-state reaction, ion irradiation, melt spinning, and mechanical alloying. Amorphous metals produced by these techniques are, strictly speaking, not glasses. However, materials scientists commonly consider amorphous alloys to be a single class of materials, regardless of how they are prepared. If they are made by rapid solidification they are named metallic glasses. So, it refers rather to the processing rout via rapid quenching than to structure.

Unlike window panes, metallic glasses are not transparent, yet their unusual atomic structure gives them distinctive mechanical and magnetic properties. In contrast to window glass, metallic glass is not brittle. Many traditional metals are relatively easy to "deform," or bend permanently out of shape, because their crystal lattices are riddled with defects. A metallic glass, in contrast, will spring back to its original shape much more readily. They are metastable as far as energy is concerned but they will turn to the crystalline state after a long time, i.e. the kinetics is rather slow.[4]

Due to an absence of microstructural features like grain- or phase-boundaries and related properties (e.g. segregation) that are typical for crystalline materials, metallic glasses (MG) exhibit excellent properties as high yield strength, advantageous soft and hard magnetic properties, high corrosion resistance, biocompatibility, etc.[5] On the other side, there are several limiting factors: high cost of components and processing, brittleness in particular under tension and bending, instability above T_x (T_x stands for temperature of crystallization), etc.

After the industrial revolution, the number of metals that are used by human beings increases significantly through the progresses of refinement and metallurgy techniques.[6] In the 1950s, however, metallurgists learned how to slow the crystallization by mixing certain metals, such as nickel and zirconium. When thin layers of such alloys were cooled at 1 million degrees Celsius per second, a metallic glass was formed.[7]

In the past, small batches of amorphous metals were produced through a variety of quick-cooling methods. For instance, amorphous metal wires have been produced by sputtering molten metal onto a spinning metal disk. The rapid cooling, of the order of millions of degrees a second, is too fast for crystalline order to form and the material is quenched into a glassy state. More recently a number of alloys with critical cooling rates low enough to allow formation of amorphous structure in thick layers (over 1 millimeter) had been produced. These are known as bulk metallic glasses (BMG).

The first reported metallic glass was an alloy (Au_{75} Si_{25}) produced at Caltech by Paul Duwez and collaborators in the sixties of last century. The glass-forming alloys had to be cooled extremely rapidly (of the order of one megakelvin per second, 10^6 K/s) to suppress crystallization. An important consequence of this was that metallic glasses could only be produced in a limited number of forms (typically ribbons, foils, or wires) in which one dimension was small so that heat could be extracted fast enough to achieve the necessary cooling rate. As a result, metallic glass specimens (with a few exceptions) were limited to thicknesses of less than one hundred micrometers.[8]

In 1969, an alloy of 77.5% Pd, 6% Cu, and 16.5% Si was found to have critical cooling rate between 100 K/s to 1000 K/s. In 1976, H. Liebermann and C. Graham developed a new method of manufacturing thin ribbons of amorphous metal on a supercooled fast-spinning wheel.[9] This was an alloy of iron, nickel, phosphorus and boron. The material, known as Metglas, was commercialized in early 1980s and used for low-loss power distribution

transformers. Metglas-2605 is composed of 80% iron and 20% boron, has a Curie temperature of 373 °C and a room temperature saturation magnetization of 125.7 mTesla.

In the early 1980s, glassy ingots with 5 mm diameter were produced from the alloy of 55% palladium, 22.5% lead, and 22.5% antimony, by surface etching followed with heating-cooling cycles. Using boron oxide flux, the achievable thickness was increased to a centimeter. The research in Tohoku University and Caltech yielded multicomponent alloys based on lanthanum, magnesium, zirconium, palladium, iron, copper, and titanium, with critical cooling rates between 1 K/s to 100 K/s, comparable to oxide glasses.

In 1988, alloys of lanthanum, aluminum, and copper ore were found to be highly glass-forming. Metallic materials in a bulk form with thicknesses of over several millimeters had been limited to a crystalline structure. This is due to the inevitable principles of phase transformation and solidification in metals and alloys. In metals and alloys atomic diffusion is extremely easy in a supercooled liquid region at high temperatures just below melting temperature, resulting in instantaneous nucleation and growth reactions of a crystalline phase. The easy transformation had lead to the limited state where bulk metallic materials were composed of only a crystalline structure. In such an enclosed state, it was found around 1990 that the phase transformation from supercooled liquid to crystalline phase was retarded by 8 to 9 orders for special multi-component metallic alloys. The selection of their novel alloy components has enabled us to produce glassy alloys in a bulk form because the transformation of supercooled liquid to crystalline phase for their alloys can be suppressed even at a very low cooling rate of the order 0.01 K/s . By the increase in the stability of supercooled liquid against crystallization by 8 to 9 orders, we can control and utilize the supercooled liquid state in special metallic alloys, leading to the production of various non-equilibrium bulk alloys exhibiting highly functional characteristics as well as unique workability and cast ability. These non-equilibrium bulk alloys have attracted increasing interest as an innovative metal for scientific and technological reasons.

In the 1990s, new alloys were developed that form glasses at cooling rates as low as one Kelvin per second. These cooling rates can be achieved by simple casting into metallic molds. These "bulk" amorphous alloys can be cast into parts of up to several centimeters in thickness (the maximum thickness depending on the alloy) while retaining an amorphous structure. The best

glass-forming alloys are based on zirconium and palladium, but alloys based on iron, titanium, copper, magnesium, and other metals are also known. Many amorphous alloys are formed by exploiting a phenomenon called the "confusion" effect. Such alloys contain so many different elements (often a dozen or more) that upon cooling at sufficiently fast rates, the constituent atoms simply cannot coordinate themselves into the equilibrium crystalline state before their mobility is stopped. In this way, the random disordered state of the atoms is "locked in".

In 1992, the first commercial amorphous alloy, Vitreloy 1 (41.2% Zr, 13.8% Ti, 12.5% Cu, 10% Ni, and 22.5% Be), was developed at Caltech, as a part of Department of Energy and NASA research of new aerospace materials. More recently scientists have created about a dozen metallic glasses in bulk form bars, for example by mixing four or five elements that possess atoms of varying sizes. That makes it tougher for the mixture to form crystal lattices. One of these new metallic glass alloys is being used commercially to make powerful golf club heads.

In 2004, two groups succeeded in producing bulk amorphous steel, one at Oak Ridge National Laboratory, the other at University of Virginia.[10,11] As advanced structural materials, the bulk-metallic glasses (BMGs) have recently received extensive interest, as they have outstanding mechanical properties, such as a high strength of up to 5 GPa[12], a large elastic deformation limit of around 2%, as well as good fatigue properties.

For obvious reasons metalic glasses are alloys rather than a pure metal. The alloys contain atoms of significantly different sizes, leading to low free volume (and therefore up to orders of magnitude higher viscosity than other metals and alloys) in the molten state. The viscosity prevents the atoms from moving enough to form an ordered lattice. The material structure also results in low shrinkage during cooling and resistance to plastic deformation. The absence of grain boundaries, the weak spots of crystalline materials, leads to a better resistance to wear and corrosion. Amorphous metals, while technically glasses, are also much tougher and less brittle than oxide glasses and ceramics.

Amorphous alloys have a variety of potentially useful properties (Fig. 1.1). In particular, they tend to be stronger than crystalline alloys of similar chemical composition, and they can sustain larger reversible ("elastic") deformations than crystalline alloys. Amorphous metals derive their strength directly from their non-crystalline structure, which does not have any of the defects (such as dislocations) that limit the strength of crystalline alloys. One

modern amorphous metal, known as Vitreloy, has a tensile strength that is almost twice that of high-grade titanium. However, metallic glasses at room temperature are not ductile and tend to fail suddenly when loaded in tension, which limits the material applicability in reliability-critical applications, as the impending failure is not evident.

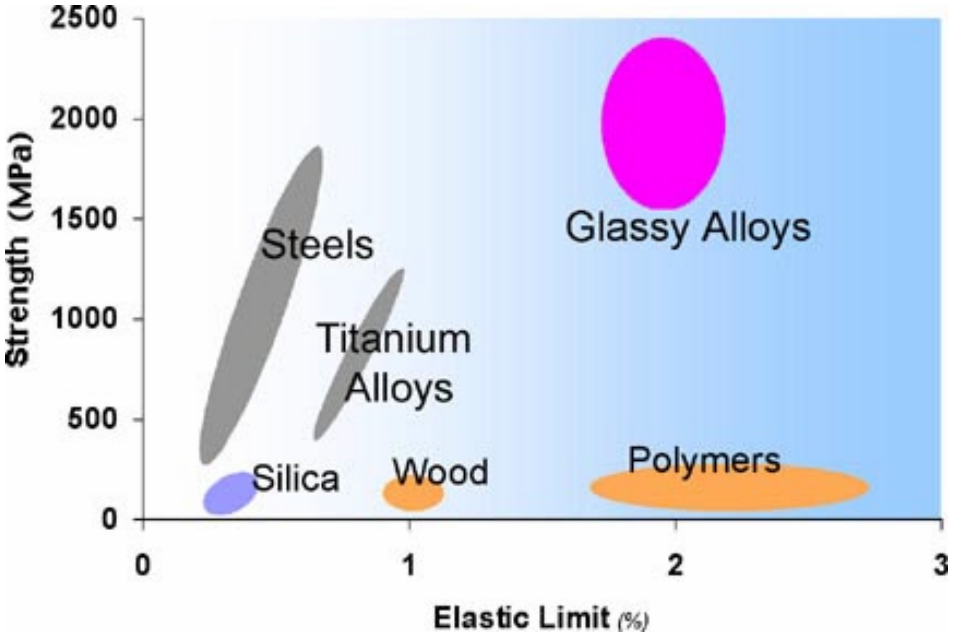

Fig.1.1. Strength vs. elasticity of materials[13]

Thermal conductivity of amorphous materials is lower than of theircrystalline counterpart. As the formation of an amorphous structure relies on fast cooling, this limits the maximum achievable thickness of amorphous structures. To achieve formation of amorphous structure even during slower cooling, the alloy has to be made of three or more components, leading to complex crystal units with higher potential energy and lower chance of formation. The atomic radius of the components has to be significantly different (over 12%), to achieve high packing density and low free volume. The combination of components should have a negative heat of mixing, inhibiting crystal nucleation and prolonging the time the molten metal stays in supercooled state.

Metallic glasses are indeed metallic in their electrical conduction, but they can have very high resistivity because of inelastic scattering. The temperature dependence of the resistivity can be positive or negative but is in any case close to zero. Their mechanical properties, because of the absence of

crystal plasticity, are quite unlike those of conventional metals. At high temperatures, there is viscous flow, which opens up the possibility of superplastic forming. At ambient temperature, although some metallic glasses are brittle, many are not. However, the plastic flow is concentrated into shear bands, which indicates that any flow leads to softening, not hardening, as normally expected for metals. This work-softening unfortunately means that, in tension, a metallic glass sample fails with little plastic elongation, in an apparently brittle manner. The absence of crystal-slip mechanisms leads to very high flow stresses.

The poor ductility and subsequent catastrophic fracture severely limit their processing and application. At low homologous temperatures, typically including room temperature, the plastic deformation of the BMGs is characterized by the inhomogeneity, and is restricted to highly localized shear bands. The excessive propagation of individual shear bands substantially decreases the plastic-deformation resistance of the BMGs, and may cause the premature fracture. Various strategies have been developed to improve their ductility. It has been realized that the dispersion of certain heterophases into the BMG's matrix can confine effectively the propagation of shear bands and promote their multiplication. Evidently, such a multiplication of the shear bands can limit the propagation of individual shear bands, and, thus, increase both the mechanical strength and ductility. This behavior has motivated the development of numerous reinforcement/ metallic glass-matrix composites. Recently, it was proposed the BMG foams may have a better ductility than solid BMGs. It was indeed confirmed that pores can also arrest shear bands and dramatically improve the ductility. Besides the interior structural modifications on the BMGs, exterior constraints are also expected to be a potential approach for multiplying the shear bands and preventing the BMGs from the premature fracture. However, to the authors' best knowledge, relatively little work has been done on this topic. Using a confining sleeve technique, Lu and Ravichandran observed a large plastic deformation of more than 10% of a Zr-base BMG in compression, which is a result of numerous shear-banding operations. This trend indicates that the mechanical constraint can effectively hinder the excessive propagation of individual shear bands. Also the specimen geometry may affect the demonstration of the ductility of the BMGs. Johnson noted that a high ductility can be observed on the specimens with the small length, i.e. in the range of 1-100 micrometer.

Metallic glasses exhibits a unique softening behavior above their glass transition and this softening has been increasingly explored for thermoplastic

forming of metallic glasses. Perhaps the most useful property of bulk amorphous alloys is that they are true glasses, which means that they soften and flow upon heating. This allows for easy processing, such as by injection molding, in much the same way as polymers. As a result, amorphous alloys have been commercialized for use in sports equipment, medical devices, and as cases for electronic equipment.

Despite the high strengths, there has been only limited interest (for example, as reinforcing fibers in auto tires) in metallic glass ribbons for mechanical applications; this is partly because their properties, although good for alloys, are not outstanding compared to other fibers, and partly because of the lack of fatigue resistance and the apparent brittleness caused by the work-softening. A mechanical property that is exploited is wear resistance. With combined wear and corrosion resistance, metallic glass coatings are suitable to withstand aggressive environments such as are found in valves. In combination with their soft magnetic properties (see below), the wear resistance is useful in tape recorder heads. The capability of amorphous alloys to be more ductile than their crystalline counterparts in bending has led to significant application as brazing foils. The corrosion resistance, although not necessarily good, can be outstanding and promoted by the chemical and structural homogeneity of metallic glasses and by the ability to have high levels of solute to produce protective oxides. Protective coatings can of course be deposited by a variety of methods, but they may also be made in situ by rapid solidification of a thin surface layer melted by a scanned laser or an electron beam. With such "laser glazing," it is difficult to get uniform completely amorphous coatings, but surface coatings of this kind have nevertheless attracted wide interest. A chemical property of interest is the use of amorphous alloys as catalysts. Of all of the properties of metallic glasses, it is their soft magnetism that has led to the most significant applications. The microstructural homogeneity of the glasses and the absence of magnetocrystalline anisotropy can give very low coercivity and low hysteretic losses. On the other hand, strong magnetostriction in many compositions and low saturation magnetizations (because of high solute levels) can be disadvantages. There is now large-scale production, by planar-flow casting, of iron-based soft magnetic material for the cores of distribution transformers, and there are many other applications in small magnetic devices, like transformers. Because of the requirement (for most compositions) for rapid liquid quenching, metallic glass samples are available only in thin cross sections. However, ribbons or sheet can be quite suitable for many

applications. For example, ribbons can be used for reinforcing elements, and thin sheet can be used for transformer core laminations or magnetic shielding.

It is well known that the bulk metallic glass is essentially a viscoelastic solid so that its deformation behavior consists of two different contributions, i.e., elasticity and viscosity. Because the Newtonian flow is very attractive for the near-net shaping and fine surface-imprinting of BMG, many studies on flow behaviors in the supercooled liquid region (T_g, is the glass transition temperature) have been done. On the contrary, there are not many reports on temperature dependence of deformation behavior in the glassy temperature region.[14]

The alloys of boron, silicon, phosphorus, and other glass formers with magnetic metals (iron, cobalt, nickel) are magnetic, with high electrical resistance. The high resistance leads to low losses by eddy currents when subjected to alternating magnetic fields, a property useful for e.g. transformer magnetic cores.

The small-scale mechanical behavior of crystalline metals can be different from that of the bulk. For example, size dependent strengths have been reported in nanoindentation, micro-torsion, micro-bending, and micro-compression, and attributed variously to hardening by geometrically necessary dislocations, dislocation interactions with surfaces, and dislocation starvation. The topic has been reviewed recently by Greer and De Hosson.[15] In amorphous metals, size effects have not received much attention, presumably because plasticity is not dislocation-mediated. At low homologous temperatures (relative to the glass-transition temperature) plastic deformation in BMGs occurs inhomogeneously with the applied strain remaining localized in a small number of discrete shear bands. Strain softening is believed to be the reason for this localization. Although the strain in the shear bands can be quite high, the overall ductility is low, and BMGs typically fracture by massive shear-off at ~ 42 – 46° to the loading axis. Strain softening is not unique for metallic glasses. It can occur in crystalline metals if the mobile dislocation density is low and is manifested as a rapid drop in stress after yielding. In the case of nearly-dislocation-free whiskers, the yield drop can be quite dramatic, because dislocations first have to be nucleated at stresses close to the theoretical strength, but once nucleated, they can multiply rapidly and move at much lower stresses. Recent micropillar compression tests on Mo-alloy single crystals also show yielding at the theoretical strength followed by catastrophic and unstable plastic deformation until the pillar is fully compressed. Since the tests were conducted in load control at a constant

loading rate, the plastic instability suggests significant strain softening after yielding, quantification of which would require a displacement controlled test. If the specimen and testing machine are treated as springs in series, the elastic displacement of the machine just prior to yielding is equal to $(\sigma_y A)/k$, where σ_y and A are the specimen yield strength and cross-sectional area, respectively, and k is the machine spring constant. Upon yielding, the specimen momentarily ceases to offer resistance, which allows the machine to spring-back and the cross-head to recover some of its displacement. In a uniaxial tensile test, the spring-back is in the same direction as the deformation of the specimen and its magnitude is proportional to the specimen cross-sectional area. In BMGs, too, plasticity initiates at approximately the theoretical shear strength. Therefore, if strain softening accompanies the generation of the initial shear bands, one would expect a substantial machine spring-back when BMGs are tested, similar to that observed in the whisker tests. However, there is a crucial difference between these two cases: in crystalline metals, after an initial period of strain softening, work hardening eventually takes over, whereas in BMGs, work hardening typically does not develop. Consequently, in crystalline metals, the initial strain softening does not normally produce massive shear instability, whereas in BMGs, we expect the machine spring-back to result in catastrophic shear failure. If this reasoning is correct, it raises the following interesting question: can the magnitude of the spring-back be sufficiently decreased, by reducing the specimen cross-sectional area, that catastrophic fracture is avoided? In other words, is there a natural transition from unstable to stable shear band propagation with decreasing specimen size? To our knowledge this issue has not been addressed before and the purpose here is to demonstrate that, indeed, there is such a size effect in BMGs.[16]

In single-phase metallic glasses there is no microstructure per se, and the intrinsic structural length scales of the system are generally believed to be of atomic dimensions; the 10–100 atom volumes associated with shear transformation zone (STZ) activity are a manifestation of this. For most experiments, the scale of the test (or specimen) is much larger than this intrinsic scale, and thus complications due to size-related constraints on the deformation mechanism are not expected to occur. However, the process of shear localization introduces additional length scales to the deformation of metallic glasses, including the width of a shear band, its shear displacement and the characteristic spacing between shear bands (Fig.1.2). As a consequence of these scales, tangible size effects can manifest themselves in

mechanical tests. For constrained geometries, shear bands are produced in a consecutive series that sequentially accommodates increments of applied strain. For such a mechanical test (e.g. a bending test), the time series of shear banding events maps to a spatial distribution of shear bands on the specimen surface, with a characteristic spacing. If one imagines the same experiment conducted again with similar geometry of a smaller size, then it is clear that the characteristic shear band spacing on the specimen surface must also decrease if the shear banding events are to individually accommodate the same amount of strain. As a consequence, shear band spacing is proportional to the characteristic specimen size. The shear displacement of a single shear band (and the magnitude of the associated slip step) also increases with specimen size. This effect has important consequences for the fracture of metallic glasses in bending because fracture is generally believed to occur along a shear band once a critical level of displacement has been attained. This results in a scale dependent fracture strain for metallic glasses, where thinner specimens may be bent to larger plastic strains without fracture and thicker plates are apparently brittle. The ‘‘size effect’’ described above is basically geometrical in nature, and has been discussed without consideration of kinetic effects. However, as detailed shear band spacing and shear offset are also impacted by strain rate and temperature. This fact speaks to the possibility of a physical (non-geometrical) size effect in metallic glasses. As noted above, the characteristic strain rate associated with shear banding is believed to be of order of s^{-1}.

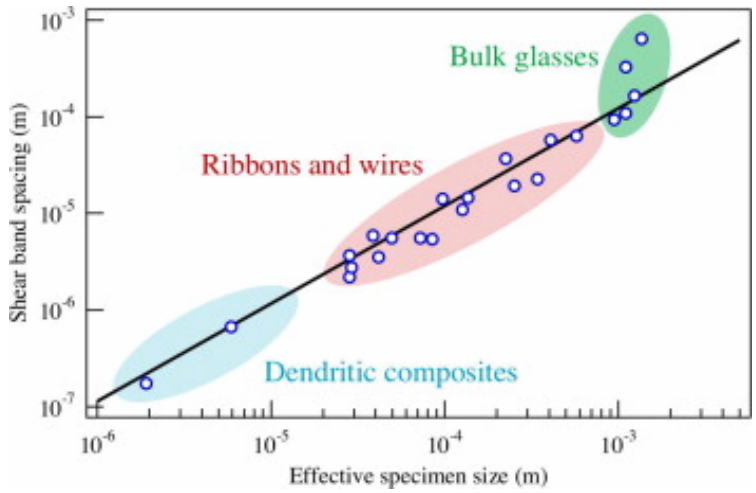

Fig.1.2. Average shear band spacing are plotted as a function o characteristic specimen dimensions for a variety of metallic glasses (and some derivative composites) deformed in constrained modes of loading.[17]

Both the geometric and intrinsic size effects described above may have practical implications for the toughness and ductility of structural bulk metallic glasses, and are certainly germane for applications involving thin films or micro-devices. What is more, there may be important interactions between the geometric and kinetic phenomena described above, although this has not yet been investigated in detail.

The fundamental mechanism of deformation in metallic glasses is thought to be the local distortion or reorganization of an atomic cluster called a shear transformation zone (STZ). While the details of the deformation process are not fully understood, in larger volumes deformation presumably occurs through the collective operation of many STZs (as in shear band formation and propagation[18], Fig. 1.3, courtesy Dave Matthews).

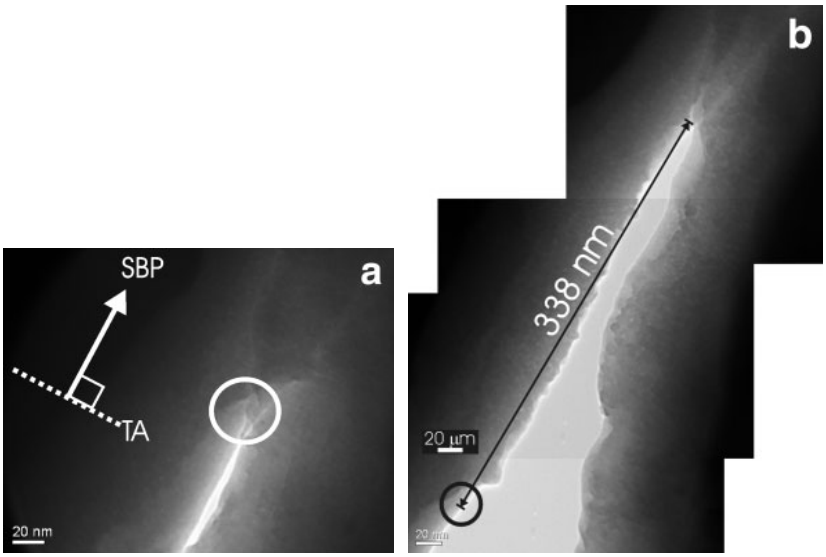

Fig. 1.3. (a) TEM micrograph of a shear band and its crack opening after 4.08% straining in $Cu_{47}Ti_{33}Zr_{11}Ni_6Sn_2Si_1$ alloy. The inset shows that the shear band propagation (SBP) direction relative to the tensile axis (TA). The white circle corresponds with the black circle in (b), a TEM micrograph of the crack opening progress at 4.12% strain.[19]

Given that STZs are the fundamental deformation mechanism, there are at least two possible perspectives on their size-dependent properties. Since the length scales in mechanical testing are typically far greater in size than the length scales associated with STZs, one could argue that metallic glasses

should possess relatively size-independent mechanical properties. On the other hand, the suggestion that the critical nucleus of a shear band has a diameter of 50–500 nm, certainly suggests some size dependence of the mechanical behavior of specimens approaching that size. There have been a number of investigations into the size-dependent strength and deformation modes of small test volumes of metallic glasses in compression and tension. Usually for compression test nowadays researcher uses small pillars with sizes up to around 100 nm, prepared by FIB technique (Fig 1.4).

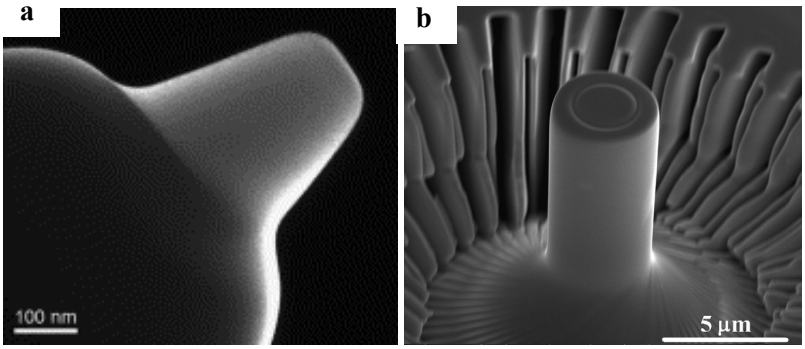

Fig. 1.4. A $Pd_{40}Ni_{40}P_{20}$ microcompression specimens prepared using focused ion beam milling.[20,21]

In $Pd_{40}Ni_{40}P_{20}$ plastic flow in compression is always localized in shear bands (in specimens with diameters ranging from 250 nm to several millimeters). A strong dependence of strength on specimen size has been suggested. To reach this conclusion, they implicitly assumed that the onset of plastic deformation is determined by the maximum shear stress or maximum effective stress in their tapered microcompression specimens. Recently, however, strong evidence is provided that the lowest shear stress on a shear plane would determine yield. While there is perhaps some dependence of strength on specimen size in metallic glasses, these measurements are clearly affected by the specimen taper. Also our investigations confirm that in BMGs there are no size effect as far as strength is concerned.[22]

On the other hand, it has been recently shown that the strength of Mg-based BMGs is sensitive to the specimen size. Specifically, the strength is higher in a smaller size sample, i.e. around 1 micrometer. The question then arises as to what would happen when the specimen size is reduced to a range where the specimen can no longer support even one single shear band.

To overcome the problem of brittleness in tension, many researchers made attempts to develop an extrinsic composite microstructure within the

glassy matrix , or an intrinsic structure, such as dual-phase BMGs or in situ precipitated nanocrystals. The basic idea is effectively to block or hinder the propagation of shear bands during deformation. For example, we have developed a phase-separated ductile Zr–Ni–Cu–Al BMG, exhibiting high compression ductility more than 30%. Recently, metallic glasses are seen as the potential material for imprinting, molding and microelectromechanical systems (MEMs) because of their high strength, hardness, and processing flexibility in the supercooled liquid region. Thus, intense efforts were made to study the properties of small-sized samples. For example, it has been found that the strength of the face-centered cubic (fcc) single crystals such as Ni and Au depend on the specimen size in the micrometer range. This dramatic effect was proposed to be a result of the reduced specimen size which is smaller than the characteristic length for dislocation multiplication, resulting in dislocation starvation. In contrast, the BMG pillars do not deform by dislocation-mitigated processes; instead, the plastic deformation in BMGs at room temperature is highly localized within shear bands or shear transformation zones (STZs). The study on the brittle Mg–Cu–Gd-based glasses (no plastic compression strain in the bulk specimens) in the form of micropillars measuring 3.8 and 1 micrometer showed a sudden strain burst, manifested a constant flow stress, and no work-hardening. Every strain burst event, regardless of the strain rate, proceeds within about one second, suggesting the strain rate during these bursts was at least 10^{-1} s^{-1}. There were very few shear bands, especially in the 1 μm pillar sample at a low strain rate: only one single shear band was present (Fig.1.5).

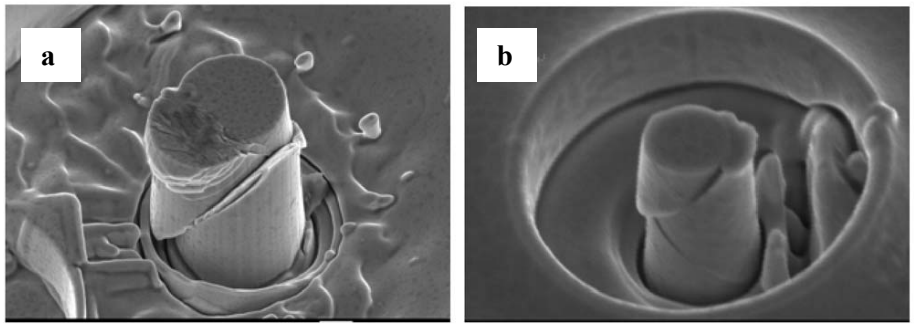

Fig.1.5. Displacement as a function of loading time during microcompression for the a) 3.8 μm and b) 1 μm pillars.[23]

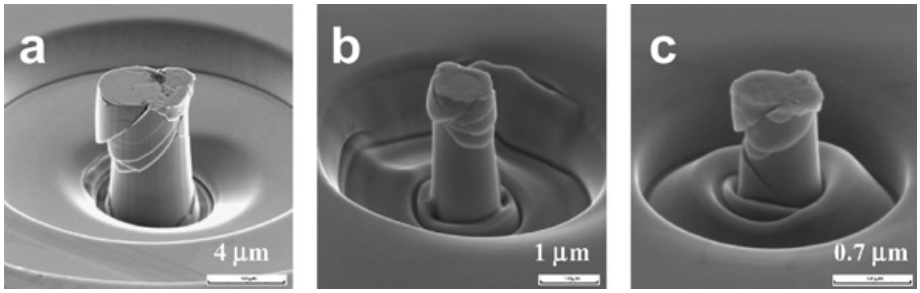

Fig. 1.6. SEM micrographs showing the appearance of deformed Zr-based MG pillars: (a) 3.8 µm, (b) 1 µm, and (c) 700 nm.[23]

In Zr-based material, which is much more ductile, shear banding behavior was definitely different (Fig. 1.6).

At temperatures well below the glass transition and at high stresses, deformation in amorphous metals occurs in highly localized shear bands. This leads to macroscopic brittle behavior and compromises the potential application of amorphous metals. The design of composites based amorphous metals may provide solutions that take advantage of their high strength but avoid brittle behavior. Many of these composites either have nanoscale features, so-called nanocomposites or are intended for applications as small components in micro- and nanosystems. Thus, size effects in the mechanical behavior of amorphous metals are important to identify and understand.

1.2 Scope of the thesis

In Chapter 2, the material compositions, preparation methods and mechanical testing techniques are introduced. Focused ion beam (FIB) technique was used as principal equipment for the preparation of metallic glass nanopillars. Conventional aspects of FIB milling process and its artifacts are presented. The mechanical testing experiments were performed on picoindentor using a Hysitron picoindenter TEM holder (Hysitron Inc., Minneapolis, MN, USA) equipped on JEOL 2010F TEM. The different aspects, relevant to the characterization of in situ TEM tests are also reviewed. The principal techniques for the observation are Scanning Electron Microscopy (SEM) attached with a TLD detector for high resolution and Transmission Electron Microscopy (TEM) with the High Resolution HRTEM measurements.

Chapter 3 presents new methods developed for the preparation of nanopillars in order to avoid conventional FIB milling artifacts. The optimized results for the sample milling by controlling FIB current and milling time are

discussed. In-situ quantitative compression tests which revealed intrinsic and strong size effects of taper-free metallic glass nanopillars inside a transmission electron microscope (TEM) on different MG compositions show predominant inhomogeneous and intermittent plastic flow characterized by shear banding events.

In Chapter 4 the extended investigation of different extrinsic and intrinsic size effect of MG at the nanoscale are reviewed. The variation of bulk modulus and Poisson's ratio affect the deformation mode and ductility of MGs at the nanoscale. Different compositions are investigated $Cu_{47}Ti_{33}Zr_{11}Ni_6Sn_2Si_1$, $Zr_{50}Ti_{16.5}Cu_{15}Ni_{18.5}$, $Zr_{61.8}Cu_{18}Ni_{10.2}Al_{10}$ and $Al_{86}Ni_9Y_5$, in-situ in a TEM.

Chapter 5 deals with the investigation of super- ductile MG. The composition was strictly designed in our lab and its aspects are discussed. A critical size was found, below which the deformation mode changes from intermittent shear banding to homogenous flow. In comparison with all other compositions Cu- and Zr-based MGs, the threshold size for the transition from brittle to ductile behavior shifts from diameter of 100 nm to 300 nm in $Al_{86}Ni_9Y_5$.

Chapter 6 completes the picture by revealing the results on unique tension experiments of $Al_{86}Ni_9Y_5$ MGs at nanoscale. The in situ TEM observations revealed a transition from brittleness on larger sizes to high plasticity performance while going to hundreds of nanometers. These tension experiments help to answer several questions about extrinsic and intrinsic size effects at submicrometer scale.

References

1. M. Miller, P. Liaw, Bulk Metallic Glasses, an Overview, 237 (2008).
2. D.T.A. Matthews, Surface Engineering: Amorphous Alloys and Nanocrystallinity, 189 (2007).
3. Science Daily "Metallic Glass: Material Of The Future?", Mar. 30 (1998).
4. A. Zhang et al., Intermetallics, 496-503 (2009).
5. I. Stloukal, L. Král, J. Cermák, Hradecnad Moravicí, 8 (2009).
6. A. Innoue, X.M. Wang, W. Zhang, Review on Advanced Materials Science 18, 1-9 (2008).
7. Johns Hopkins University, Science blog (1998).
8. W. Klement, R.H. Willens, Duwez, Pol, Nature 187, 869–870 (1960).

9. H. Libermann and C. Graham, IEEE Transactions on Magnetics, 12 (6) (1976).
10. ORNL Review 38 (1) (2005).
11. V. Ponnambalam, S. Joseph Poon and Gary J. Shiflet, Journal of Materials Research 19 (5), 1320-1323 (2004).
12. W.H. Jiang, G.J. Fana, H. Choo, and P.K. Liaw, Materials Letter 60 (29-30), 3537-3540 (2006).
13. http://www.its.caltech.edu/
14. H. Kato, H. Igarashi and A. Inoue, Materials Letters 62(10-11), 1592-1594 (2008).
15. J. R. Greer and J.Th.M. De Hosson, Progress in Materials Science 56, 654–724 (2011).
16. S. Xie and E. P. George, Intermetallics 16 (3), 485-489 (2008).
17. C. A. Schuh, T. C. Hufnagel, U. Ramamurty, Acta Materialia 55, 4067–4109 (2007)
18. J.Th.M. De Hosson, Microscopy research and technique 1097-1129 (2009).
19. D.T.A. Matthews, V. Ocelík, P.M. Bronsveld, and J.Th.M. De Hosson, Acta Materialia 56 (8) 1762-1773 (2008).
20. B.E. Schuster, Q. Wei, T.C. Hufnagel and K.T. Ramesh, Acta Materialia 56(18) 5091-5100 (2008).
21. X.L. Wu, Y.Z. Guo, Q. Wei, and W.H. Wang, Acta Materialia 57(12) 3562-3571 (2009).
22. C.Q. Chen, Y.T. Pei, J.Th.M. De Hosson, Acta Materialia, 58 (1), 189-200 (2010).
23. C. J. Lee, Y.H.Lai, C. W. Tang, J. C. Huang and J. S. C. Jang, Materials Transactions 50(12) 2795-2800 (2009).

Chapter 2

Preparation and mechanical testing techniques

This chapter presents a concise overview of the experimental techniques used in this thesis work, e.g. Focused Ion Beam (FIB) for the milling of metallic glass nanopillars, picoindenter installed in Transmission Electron Microscope for the in situ mechanical testing of metallic glass nanopillars. The preparation methods of metallic glasses will be also discussed. Scanning Electron Microscopy and X-ray techniques, which were used for the preparation control and post mortem observation of metallic glasses will be summarized.

2.1 Preparation and characterization techniques

2.1.1 Melt spinning for MG preparation

The method that we have used for the preparation of metallic glassy (MG) ribbons is called melt spinning.[1] A schematic representation and picture of melt spinning technique is shown on Fig.2.2. The molten material is driven from the nozzle in the form of a jet, which impinges with a rotating wheel. Puddles formed under the counteracting forces of the flow of the material and the surface tension. Because of the low viscosity of the molten metallic alloy, the shear layers extend only a few microns from the surface of the roller into the puddle and stays on the roller surface. Because of a large temperature gradient at the melt-substrate interface, the melt beneath the puddle solidifies into a ribbon. The ribbon remains in contact with the disc surface and then leaves it under the action of the centrifugal force.

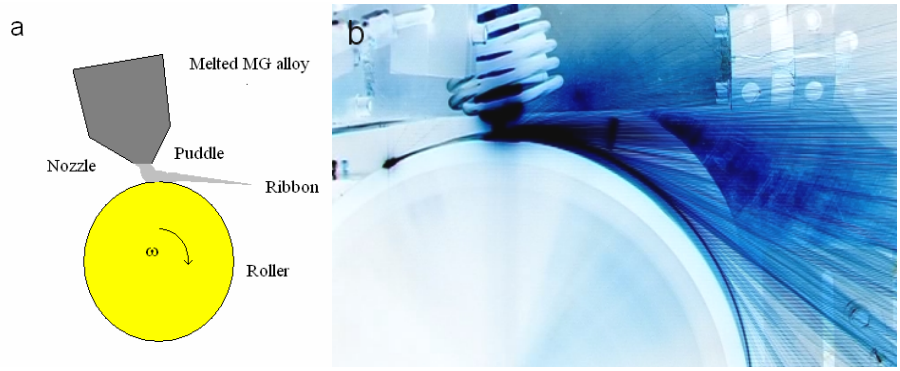

Fig.2.2. Schematic diagram (a) and picture (b) of melt spinning technique Fraunhofer- Bremen-Dresden, Germany.

For our experiments we have chosen the compositions $Zr_{61.8}Cu_{18}Ni_{10.2}Al_{10}$ and $Al_{86}NI_9Y_5$ with low shear modulus over bulk modulus, i.e. μ/B, that according to predictions have higher ductility. The idea was to check whether the ductility of bulk MG alloys may affect the deformation mode of micropillars and the transition of banding events from nucleation control to propagation control.[2] Strips of such MG alloy were prepared by vacuum arc melting and mold-casting with water cooling, SEM micrographs are shown at Fig. 2.3.

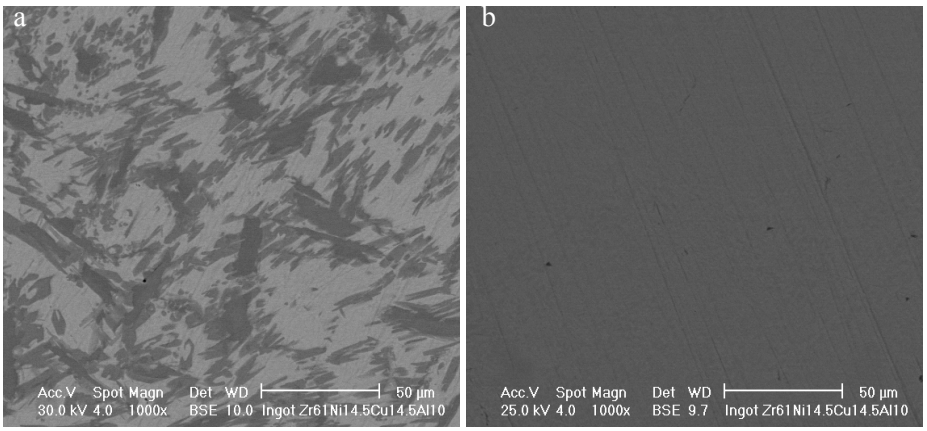

Fig. 2.3. SEM micrograph of $Zr_{61.8}Cu_{18}Ni_{10.2}Al_{10}$ strip as alloy (a) and melt-spin MG ribbon (b).

2.1.2 Mechanical polishing of MG ribbon

A typical mechanical polishing tool is represented in Fig. 2.4. It consists of a spinning flat plate which is covered by a pad. The ribbon that is being

polished is mounted with special holder. During the process of loading and unloading an oil introduction mechanism deposits the oil on the pad. Both the plate and the holder are then rotated and the holder is kept oscillating as well. A downward manual pressure force is applied to the holder. The manual force depends on the contact area and polishing requirements. The roughness of the ribbon edge that has been achieved by using this technique was equal to 2 to 5 μm, which was suitable for further sample preparation.

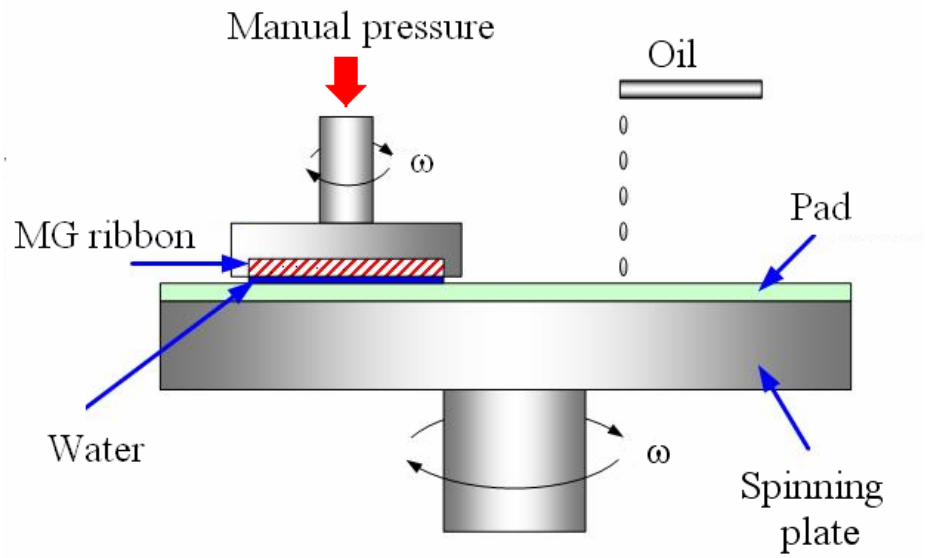

Fig.2.4. Schematic picture of mechanical polishing technique

2.1.3 Surface characterization techniques

Scanning electron microscopy (SEM)

In order to make a link between processing, microstructure and properties in materials science, almost every year new and exciting characterization techniques enter the field. A landmark in the analysis of both bulk materials and surfaces, since its introduction in the 1930s, is the electron microscope.[3] The two most popular electron microscopy techniques probably are the scanning electron microscope (SEM, Fig. 2.5) and the transmission electron microscope (TEM, Fig. 2.8.). The resolving power is defined as the closest

spacing between two points which can be clearly seen by the naked eye to be separate entities. The resolving power in microscopy is limited by diffraction of the source as it passes through a series of apertures. An empirical diffraction limit is given by the Rayleigh criterion

$$\sin\theta = 1.22\frac{\lambda}{D} \tag{2.1}$$

where θ is the opening angle of the ray from the source, λ is the wavelength of the incoming electrons or photons and D is the diameter of the lens. It follows therefore that for the best resolving power, λ should be as small as possible and/or D should be as large as possible. The electron beam is focused by a system of magnetic lenses to a small spot of around 1-10 nm in diameter. Primary electrons which enter the specimen are scattered elastically or inelastically by the atoms. This can cause electrons to exit the specimen, i.e. backscatter, after traveling through the specimen. Since the material volume in which the electrons are backscattered, can be much larger than for the secondary electrons, the lateral resolution is much smaller.

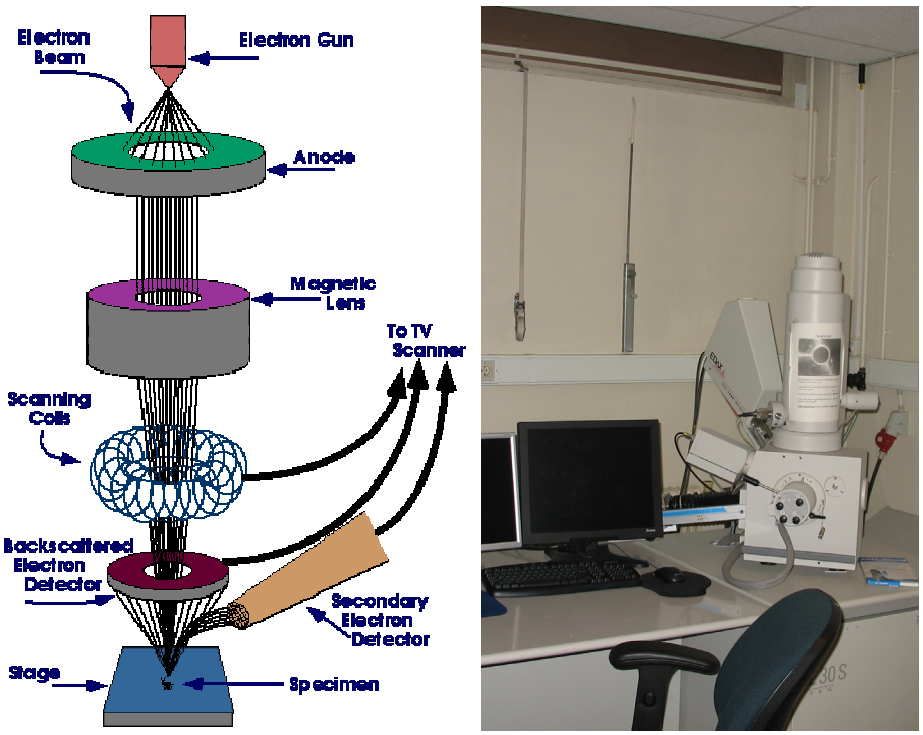

Fig. 2.5. left: Schematic representation of a SEM; right: picture of one of the SEMs (Phillips XL30 SEM FEG) of the Materials Science group.

If the microscope is operating in the backscattered mode, the result is a lateral resolution of the order of micrometers. The penetration depth of the high energy electrons will cause the electrons to be trapped in the material. When studying conducting materials, the electrons will be transported away from the point of incidence. If the specimen is a non-conducting material, the excess electrons will cause charging of the surface. The electrostatic charge on the surface deflects the incoming electrons, giving rise to distortion of the image. In order to reduce surface charging effects, a conducting layer of metal, with typical thickness of 5-10 nm, can be sputtered onto the surface.

Charging of the surface is not the only factor determining the resolution of a scanning electron microscope. The width of the electron beam is also an important factor for the lateral resolution. A narrow electron beam results in a high resolution. The broadening of the spot size is the sum of broadening effects due to several processes. The first contributor is the beam itself and the second part is the contribution due to diffraction of the electrons of wavelength λ by the size of the final aperture. The latter parts are the broadening caused by chromatic and spherical aberrations. To achieve the smallest spot size, all contributions should be as small as possible. Decreasing the accelerating voltage will not only cause the wavelength of the electrons to increase, but also the chromatic aberration increases as well, resulting in increasing of the spot size and, as a consequence, a decrease in resolving power of the microscope.

X-ray characterization technique

The principle of this technique is based on the detection of a diffracted beam when the Bragg diffraction condition $n\lambda = 2d\sin\theta$ is fulfilled, where d is the space between the planes, θ is the diffraction angle, n is the order of the diffraction peak and λ is the wavelength of the X-rays. [4]

During the collection of the diffraction spectrum, only the detector rotates through the angular range, thus keeping the incident angle, the beam path length, and the irradiated area constant. The long slit on the receiving side allows only those beams that are nearly parallel to arrive at the detector. This has an added advantage of reducing the sensitivity to sample displacement from the rotation axis.

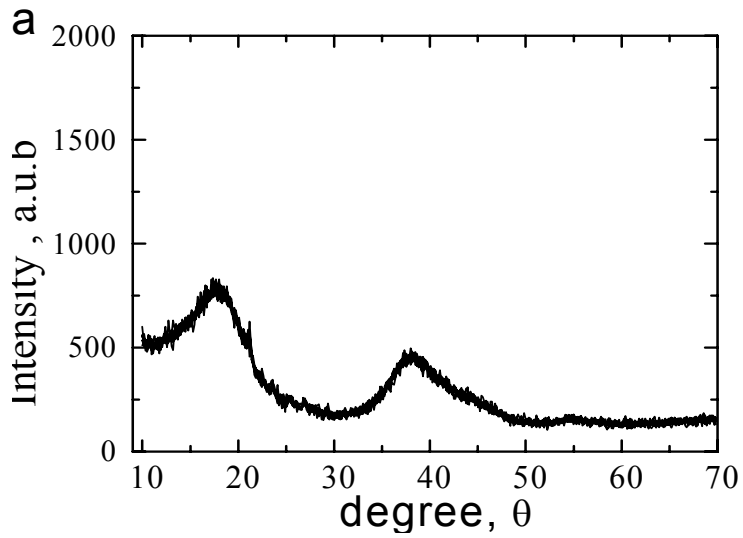

Fig. 2.6.X-ray diffraction (XRD) spectra of $Al_{86}NI_9Y_5$ MG

A single circle diffractometer was used with an grazing angle of 1.5°, with a CuKα radiation (λ=1.540 Å) generator operated at 40kV and 40mA. Fig. 2.6 shows a XRD spectra of the amorphous $Al_{86}NI_9Y_5$ ribbon. Two homogeneous rings are indicating on the amorphous nature of the investigated metallic ribbon.

2.1.4 FIB technique

The Focused Ion Beam technique was used for the fine stage in the preparation of the samples for mechanical testing in TEM. A FIB instrument represents an ion gun installed in a SEM. Both instruments operate with focused beam to image the specimen, i.e. an ion beam for the FIB and an electron beam for the SEM. In the FIB, secondary ions are used to image and to mill the sample.

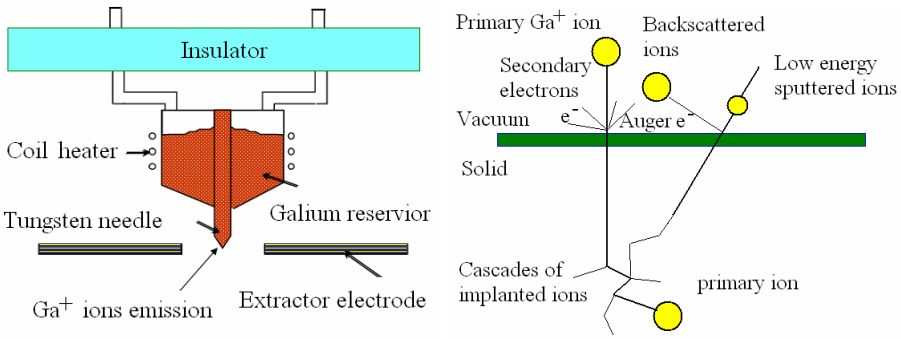

Fig. 2.7. left: schematic picture of the liquid ion beam source; right: interaction of Ga^+ ion with the solid surface.

The operation of a FIB begins with a liquid metal ion source. A reservoir of gallium (Ga) is positioned in contact with a sharp W needle. Ions are emitted as a result of field ionization and post-ionization and then accelerated down the FIB column towards the sample (Fig. 2.7.a). When Ga ions are accelerated toward the target sample, they enter the sample and create a cascade of events which results in the ejection of a sputtered particle (Fig.2.7.b)

2.2 Picoindentation tests in TEM

2.2.1 Introduction of TEM

The optical microscope has a limited spatial resolution because it uses as source visible light, which has a relatively long wavelength. The electron microscope has the best possible source to overcome this limitation because of the wave-like character with short wavelength of accelerated electrons.[5] The first Transmission Electron Microscope (TEM) was built by Max Knoll and Ernst Ruska in 1932. The famous DeBroglie equation relates the momentum of the particle, and the wavelength through Planck's constant

$$\lambda = \frac{h}{p}. \tag{2.2}$$

When electrons are accelerated to a high energy of 200 keV by the accelerating voltage, the corresponding wavelength of the electrons is 2.51 pm, which is a very small value compared to the diameter of the atoms. However, the resolution of a TEM is not equal to the wavelength, because is limited by the aberrations of the electro-magnetic lenses used in the

microscope. A reduction in the spherical aberration of the objective lens is a first step to increase the resolution limits in high resolution microscopy.

Generally the chemical composition of the material can also be obtained with a resolution of a few nanometers. Electron microcopy is not just a single technique, but a diversity of electron-matter interactions with unique properties are used to gain insight in structure, morphology and chemical composition, where the latter is obtained via spectroscopic techniques (Fig. 2.8).

During elastic interaction no energy is transferred from the electron to the sample, as a result the electron leaving the sample has its original energy and contributes to the direct and diffracted beams. In contrast, inelastically scattered electrons reduce the quality of the images and diffraction patterns. Most of the signals other than elastic scattering are used in analytical microscopy to obtain chemical and other spectroscopic information from the specimen. JEOL 2010F TEM (Fig. 2.8.) was used for the research work presented in this thesis.

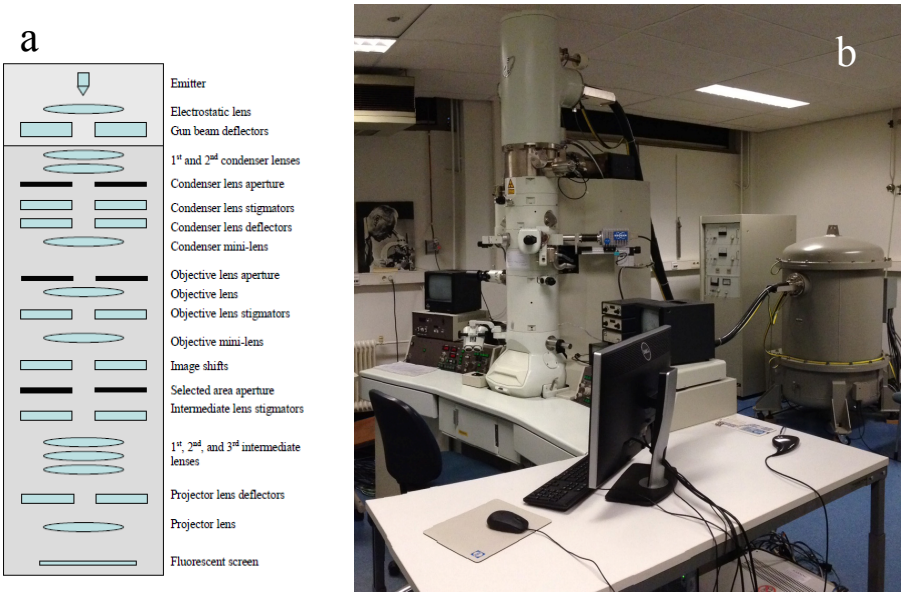

Fig.2.8. Left: schematic of lenses, apertures, stigmators, and deflectors of TEM column; right: picture of one of the TEMs (JEOL 2010F) of the Materials Science group.

The electron beam of a JEOL 2010F is operated at an acceleration voltage of 200 keV. A Gatan digital micrograph software and CCD cameras were used to record and analyze the TEM images. In-situ TEM compression

experiments were performed using a Hysitron picoindenter TEM holder (Hysitron Inc., Minneapolis, MN, USA) implemented on the JEOL 2010F TEM.

2.2.2 In situ compression, tension and cyclic tests in TEM

Testing the mechanical properties of nanoscale materials faces a number of inherent challenges. As the size of the "target" decreases, the inability to actually see what occurs during testing can be troublesome. Here we present a compression, tension and cyclic experiments of the *in situ* mechanical testing. With the picoindenter TEM holder (Hysitron Inc., Minneapolis, MN, USA) equipped on JEOL 2010F TEM it is possible to acquire quantitative mechanical data while simultaneously monitoring the microstructural evolution of the sample with the TEM (Fig. 2.9).

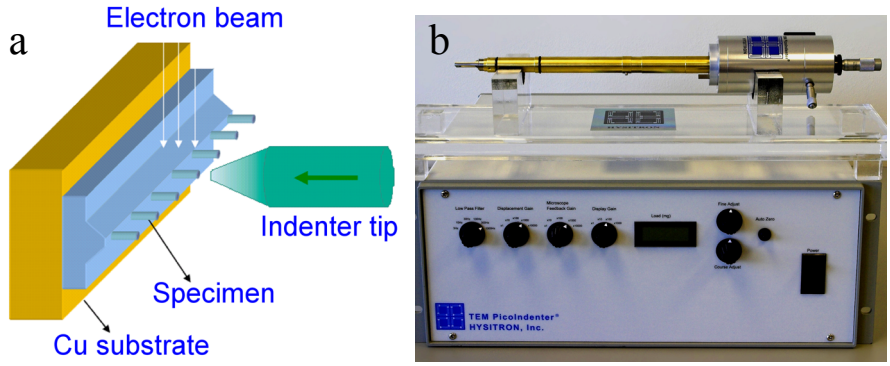

Fig. 2.9. Scheme of quantitative in-situ compression test in TEM (a) specimen diameters are at a submicrometer range, length of specimen base is mm range and total with sub-mm range, Hysitron picoindenter (b)

In-situ TEM compression experiments were performed using a picoindenter with a diamond flat punch of 2 mm in diameter. The indenter has several unique features, which are particularly critical to the present study. First, it is integrated with a miniature capacitive load–displacement transducer permitting high resolution load and displacement measurements (resolution of ~0.3 μN in load, ~1 nm in displacement). In addition, a rapid instrument response and data acquisition rate (the controller is operating in a continuous loop and samples data at 20 kHz) allows discrete flow events to be well-resolved. The experiments were run in two typical control modes:

displacement control, which shows a great sensitivity, and load control, which has an advantage when evaluating sudden displacement jumps. The displacement and/or load rate are programmed in such a way that a nominal strain rate of ~ 10^{-2} s^{-1} is applied. Together with the high data acquisition rate, this all makes it possible to evaluate the development of a single SB event.[6,7]

Tensile experiments allow circumventing some artifacts (tapering, shear band formation due to friction) and increased purity of MG testing at the nanoscale. In-situ TEM tension experiments were performed by using a Hysitron picoindenter TEM holder with an in house –made Al tip sample holder and W indenter tip.

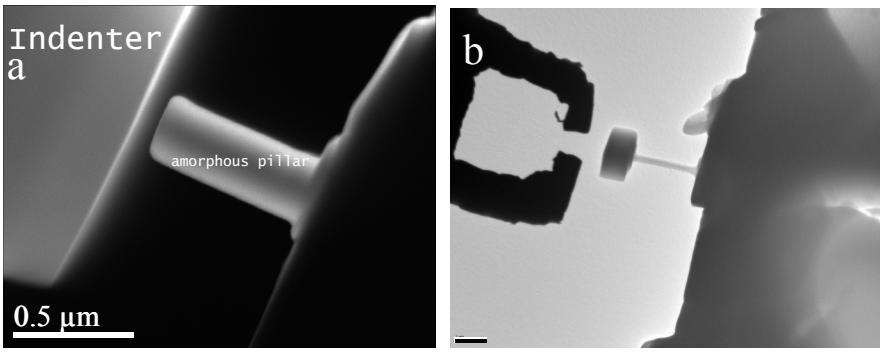

Fig. 2.10. (a) TEM picture of compression testing; (b) FIB milled W tensile tip and mushroom-like nanopillar.

Al holder was designed and developed in order to achieve good calibration and to avoid undesirable mechanical noise during tensile experiments. Tungsten tip was designed and made first by electrochemical polishing and later on milled by Focused ion beam (FIB) to a desired shape.

References

1. The Institute of Solid State Physics, Materials Science and Technology in Kharkiv Institute of Physics and Technology (KIPT)
2. O.V. Kuzmin, Y.T. Pei, C.Q. Chen, J.Th.M. De Hosson, Acta Materialia 60, 889–898 (2012)
3. V.A. Zworykin, J. Hillier, R.L. Snyder, ASTM Bulletin 117, 15–23 (1942).
4. C.S. Barrett, Physical Review 38, 832-833 (1931).
5. H. G. Rudenberg and P.G. Rudenberg, Advances in Imaging and Electron Physics 160, 207-286 (2010).

6. O.V. Kuzmin, Y.T. Pei, J.Th.M. De Hosson, Applied Physics Letters 98, 233104 (2011).
7. C.Q. Chen, Y.T. Pei, J.Th.M. De Hosson, Acta Materialia 58, 189–200 (2010).

Chapter 3

FIB milling and size effects of taper free metallic glass pillars

In this chapter we present a versatile method to fabricate taper-free sub-micrometer and nanometer sized pillars through focused ion beam (FIB). The key feature of the fabrication is: an ion-beam with an incident angle of 90° to the longitudinal axis of the pillar that enables to mill the pillar sideways avoiding tapering. A procedure to determine accurately the cross-section of each pillar was developed. Taper-free pillars with different chemical compositions, i.e. $Zr_{61.8}Cu_{18}Ni_{10.2}Al_{10}$ and $Al_{86}Ni_9Y_5$ and diameters ranging from 700 to 90 nm were investigated. In-situ quantitative compression tests which revealed intrinsic and strong size effects of taper-free metallic glass nanopillars inside a transmission electron microscope (TEM) are discussed in detail.

3.1 Introduction

Study on size effects in the mechanical response of MGs is interesting as it may provide hints on the fundamental issues of extrinsic versus intrinsic mechanical properties. Also it may guide us to the practical design of small size MG-incorporated materials and devices.[1-3] Consequently these basic questions provided an impetus to considerable theoretical[4-6] and experimental[7-16] attention. From experimental observations it has become clear that at a micrometer scale shear banding is still the predominant behavior.[7-11] Testing of submicron- and nanometer sized samples is highly desirable but these experiments are extremely challenging because of the difficulties in performing well-designed experiments, i.e. fabricating nanosized specimens, which are desired to be free-of geometrical imperfections and surface contaminations.[7-15] Recent literature hints to homogeneous plastic flow,[8-14] but also remarkable artifacts arising from geometrical tapering and surface modification due to the use of focused ion beam (FIB) are not always clarified. In addition, the driving force and microscopic basic concepts of such transitions in deformation modes remain rather obscure and elusive.

The focused ion beam (FIB) technique has been known over several decades, with diverse applications including various design, mechanical testing and failure analysis of different types of materials.[17,18,19,20] In the materials science domain, its applications are just as widespread, encompassing of microstructural analysis,[21] transmission electron microscopy (TEM) specimen preparation,[22] thickness determination of coatings[23] and micro-, nanomachining.[24,25] A FIB is designed similar to a scanning electron microscope (SEM); however, instead of an electron source, it utilizes a liquid metal ion source (e.g. Ga) . The filament to produce a high-focused (5 nm) beam of energetic metal ions can be operated either at low beam currents (<1 pA) for high resolution imaging or precise milling, or higher beam currents (10-30 nA) for coarser and faster milling.[26] The dual beam system FIB-SEM is commonly used all around the world. This equipment interfaces an ion column and an electron column at a 55° angle to each other. Interaction of either the electron beam or the ion beam with the specimen produces secondary electrons which are detected and used to form an image. Images generated with the ion beam display different contrast mechanisms, depth of focus and sensitivity to surface topography[27] compared to images generated by the electron beam. Therefore both ion and electron images are useful in providing complementary information. However, the ion beam, even when used at low beam currents, will always remove material from the specimen surface. Despite of many advantages of this technique these are several crucial complexities which may have various consequences depending on the type of the applications used. Some of them, such as re-deposition, surface damage induced by ions, tapering angle, etc.

For the mechanical testing of materials at nanoscale, a crucial problem is tapering of objects made through FIB. For instance, highly localized shear bands in metallic glasses (MG) may preferentially nucleate at the corner of a tapered sample-plunger contact during compression.[28] So-called mushrooming effects.[29,30] These effects become more serious in smaller pillars. These effects become more serious in thinner pillars at the nanoscale. Our study demonstrates a new method for the preparation of submicron pillar samples in investigating size-dependent deformation effects. The FIB milling approach is uniquely suited for the fabrication of 3D structures with nanometer precision in a variety of metallic and non-metallic materials.

Due to the FIB milling process, sub-micron sized pillars require corrections of the measurements of noncircular cross-section area for an accurate calculation of the applied stresses during compression. The model

proposed in this paper is related to the time of the FIB milling process. There are two factors that in most of the cases are relevant to consider. One of them is the smoothness of the final shape of the pillar and the second is the manufacturing time for the FIB milling process.

A particular challenge is the preparation of pillars with smaller size. Upon decreasing size the angle that supposed to be 90^0 becomes rounded off. That does not have much influence on the deformation behavior of the pillar under compression, but it makes precise determination of the applied stress rather difficult. The calculation of the cross-section area becomes a problem at smaller diameter and may cause a wrong conclusion whether size effects exist or not. The process that we may have an influence on milling artifact includes the interaction between ions of FIB source and amorphous surface of the materials.

In bulk metallic glasses plastic deformation is concentrated in extremely thin, sheet-like volumes known as shear bands (SBs) and a relevant question is whether and how nucleation and propagation of these SBs are affected by the external size of the system. Do we face extrinsic or intrinsic size effects and would it be possible to suppress brittleness and enhance ductility just by changing the size of the samples?[31,32] Despite the number of recent publications dealing with compression of focused ion beam (FIB) fabricated micropillars, consensus does not seem to exist on size effects in either strength or modes of deformation of MGs. These controversies are largely related to the ex-situ tests methods when deformation events cannot be correlated to the particular individual SBs.[33,34-42 43,44]

Besides size effects addition of alloying elements that lower the ratio between shear modulus (μ) and bulk modulus (B) may help in alleviating brittleness. Metallic glasses with $\mu/B > 0.41–0.43$ (or, equivalently, with Poisson's ratio $\nu < 0.31–0.32$) are more brittle.[45] This correlation applies equally for as-cast metallic glasses of different compositions. In this chapter Al addition was chosen to improve the ductility of MG in bulk state instead of Ti addition in previously investigated $Zr_{50}Ti_{16.5}Cu_{15}Ni_{18.5}$. In-situ TEM compression observations of taper-free micro-/nano- pillars of Zr-based MG of $Zr_{61.8}Cu_{18}Ni_{10.2}Al_{10}$ composition and diameters ranging from 600 nm to 90 nm are presented.

The basic carriers of plasticity in MGs are widely accepted to be shear transformation zones (STZs), each of which is a local atomic region containing tens to hundreds atoms and confined within an elastic medium.[46,47,48-50] However, the dynamics and correlation of the local flow

units, and their spatiotemporal evolution into macroscopic shear bands (SBs) remain mysterious.

3.2 Experimental

This Chapter includes two different experimental parts. In the first part MGs with Al and Zr base with the compositions $Al_{86}Ni_9Y_5$ and $Zr_{61.8}Cu_{18}Ni_{10.2}Al_{10}$ were selected for the experiments. Microwedges were prepared by mechanical polishing out MG ribbons with the length about 100 μm and thickness 3-5 μm. The experiments were performed on a dual beam FIB-SEM microscope (Lyra, Tescan, CZ) by varying the parameters while preparing the nanopillars out of MG microwedges. The FIB gun operates with Ga ions. We have investigated pillars with different diameters (ranged from 1200 nm down to 100 nm). The presets of the FIB current require different apertures, which basically decrease the number of the ions impinging the sample, and therefore improving the accuracy of the cut. TEM was used to measure the FIB milling artifacts, especially for measuring of the sharpness of the curve at the edges of pillars.

By setting approximately equal milling time with different current we can conclude on the quality of the milling process. The presets of the FIB current are presented in Table 3.1.

Table 3.1. The FIB current presets for milling of nanopillars

Diameter, nm	FIB current presets, pA	Milling time, s	Sharpness, nm (error: about 5-10%)
500	200	10-20	60
400	150	15-20	40
300	40	20-30	30
200	10	30-40	20
100	<1	50 - 80	20

Non-tapered nano-pillars were fabricated by FIB in a FIB/SEM microscope (Lyra, Tescan, CZ) from Zr-based MG ribbons of $Zr_{61.8}Cu_{18}Ni_{10.2}Al_{10}$ and Cu-based MG $Cu_{47}Ti_{33}Zr_{11}Ni_6Sn_2Si_1$ composition prepared by melt spinning. Micro-wedges out of these ribbons with length about 100 μm and thickness 2-5 μm were prepared by mechanical polishing. A set of taper-free nanopillars with diameters ranging from 600 to 90 nm was

fabricated by using a combination of top and side FIB milling. In this study the side surfaces of the pillars are finally polished with ion beam oriented perpendicular to the pillars in a quasi-parallel milling mode to remove tapering and to avoid surface re-deposition. First a series of rectangular microsized beams were milled on the microwedge. Then out of these beams, nanopillars (Fig. 3.1 a) with aspect ratio ranging between 3 and 4 were fabricated step-bystep by decreasing of FIB current on different milling stages. The final shape of the taper-free pillars has been achieved by FIB side polishing (Fig. 3.1 b). The uniform amorphousness of the FIB-milled nanopillars was verified by X-ray analysis and TEM observations.

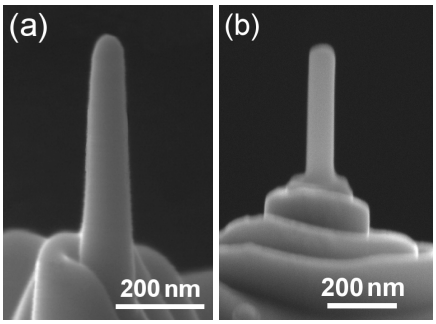

Fig.3.1.(a) SEM image of $Zr_{61.8}Cu_{18}Ni_{10.2}Al_{10}$ nanopillar made by FIB top milling;(b) further side polishing.

In-situ TEM compression experiments were performed using a Hysitron picoindenter TEM holder (Hysitron Inc., Minneapolis, MN, USA) equipped in a JEOL 2010F TEM, with a diamond flat punch of 2 μm in diameter. The indenter has several unique features, which are particularly critical to the present study. First, it is integrated with a miniature capacitive load–displacement transducer permitting high resolution load and displacement measurements (resolution of ~0.3 μN in load, ~1 nm in displacement). In addition, a rapid instrument response and data acquisition rate (the controller is operating in a continuous loop and samples data at 20 kHz) allows discrete flow events to be well-resolved. The experiments were run in two typical control modes: displacement-rate control that shows a great sensitivity, and load control that has an advantage in evaluating sudden displacement jumps (shear band offset). The displacement and/or load rate were programmed in such a way that a nominal strain rate of ~ 10^{-2} s^{-1} is applied.

3.3 Results and discussion

3.3.1 FIB milling artifacts

There are two different artifacts known as redeposition and tapering effects that occur during FIB milling procedure and have an influence first on the quality and the geometry of the MG pillars and make the analysis of the experiments rather difficult. The influence of the redeposition effect on the FIB microfabrication process by conventional top FIB milling method is significant. There are several parameters such as beam current, ion beam spot size, milling speed could also key factors that determines this process. Not fully controllable portions of material can be redeposited on the walls of the sample and will form an undesirable pattern on the surface of the sample. Relationships between milling depth, sputtering yield and ion dose redeposition are complex in FIB milling. As material is sputtered away, some of it becomes redeposited in the volume that is being sputtered (Fig. 3.2 a). For low speed scans, the redeposited material is not removed. As a consequence the higher the aspect ratio, the more redeposited material is accumulated on the surface. In addition, different tilting angles of the sample cause a different ion sputtering angle that leads to different geometrical dimensions of the pattern bottom owing to the re-deposition. Re-deposition is critically depending upon how the milling is carried out. Since in our experiments the preparation required certain fixed ion beam parameters, a new method of side FIB milling was developed.

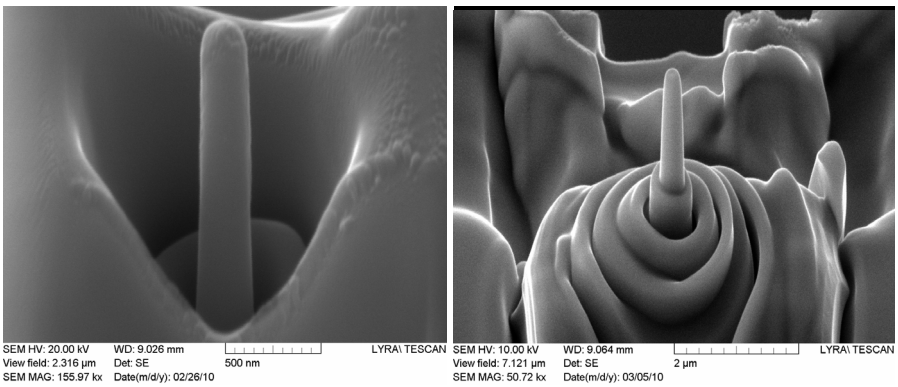

Fig.3.2. (a) SEM image of $Zr_{61.8}Cu_{18}Ni_{10.2}Al_{10}$ nanopillar made by conventional FIB top milling method;(b) tapering effect..

A FIB milling artifact which significantly influences the analyzing of compression tests is tapering effect (Fig. 3.2 b). Tapering artifact owing to the tapered geometry of the FIB milled micro-/nanopillars. Since the sample is tapered, yielding will start from the top of the sample because this is the location with the minimum cross section. Tapering angle will have a significant influence on the deformation behavior of nanopillars. In the next paragraph the home made method that allows circumventing significant artifacts of FIB milling of MG pillars is described.

3.3.2 A novel FIB milling method for MG preparation

The objectives of the current experiments appear from the necessity to avoid the major FIB artifact such as tapering angle. The sample must be glued to the sample stage and mounted to flat surface of the FIB holder (Fig. 3.3a). At the first milling step the sample stage must be tilted to an initiate angle that allows separating the pillars of chosen polygonal shape in one row from each other in view of FIB image, the tilting angle can be 45° and 77.5° from the side surface normal for square and octagonal pillars, respectively (see Fig. 3.3d). Such an angle allows cutting the pillars from the side (Fig. 3.3b). The next milling step is done step by step to form the adjacent sides. The pillar can be milled further by changing the milling characteristics such as current and time in order to mill until the desired size (Fig. 3.3c).

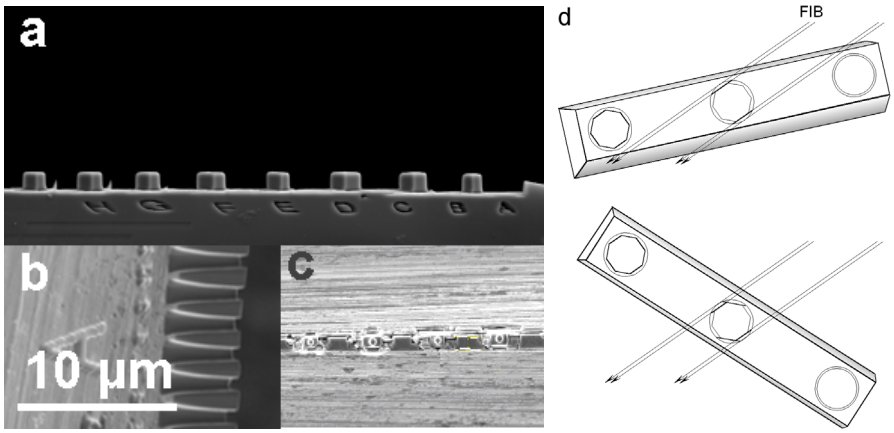

Fig. 3.3. Preparation stages of the pillars: (a) side view of prepared pillar, (b) side view of pre-milled beams at 90 degrees rotation angle, (c) top view of the ribbon with milled beams

The second important characteristic that has to be chosen properly is the FIB milling current. The smaller the size of the desired pillar, the smaller Fib current must be used to decrease the FIB damage of the surface and the rounding of the shape of the edge. (Fig.3.3). For the preparation of each pillar the final FIB cutting step is important.

The one of the most important characteristics while performing mechanical testing is the stress calculation:

$$\sigma = \frac{P}{S} \tag{3.1}$$

where P is the load, S is the cross-section area. Therefore, the major controllable factor affecting the final shape of the pillars and therefore the stress measurements is FIB current. Since the flow of the ions is proportional to the ion beam current and considering the amorphousness of the pillar surface the current which is needed to prepare 100 nm pillars with same quality should be as low as possible. The current is it already limited by the size of the ions and therefore becomes a challenge for instrumental industry. The correlation between the real cross-section of the pillar and experimental curve of the FIB currents versus diameters was obtained. While measuring pillar diameter in TEM (rotation angle is 45° around z axis), the following results are observed (Fig.3.4). From the experimental procedure occurs

As said before, another important factor is the FIB milling current. The smaller the size of the desired pillar, the smaller FIB current must be used for each milling step in order to minimize possible FIB damage of the surface (Fig. 3.4), in particular, the final FIB cutting step.

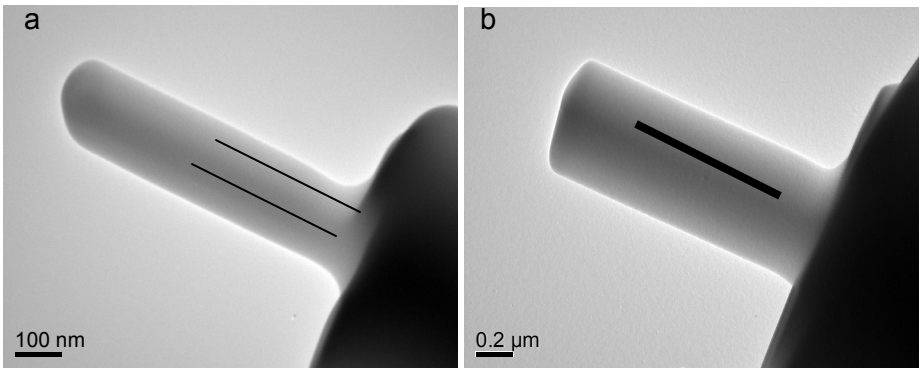

Fig.3.4 TEM images of the pillars prepared by FIB: (a) ø 150 nm; (b) ø 600 nm. Black lines indicate the sharpness caused by rough FIB milling

Our method is designed having a reproducible procedure not only to make small pillars but also to find a way to calculate the cross-section of the pillars accurately. The latter is relevant for an accurate determination of the applied stress fields.[51] Therefore, the major controllable factor that affects the final shape of the pillars and therefore the stress measurements is the FIB current. Measurements of the pillar diameter in TEM (tilting angle is 45° around z axis) can be summarized as follows.

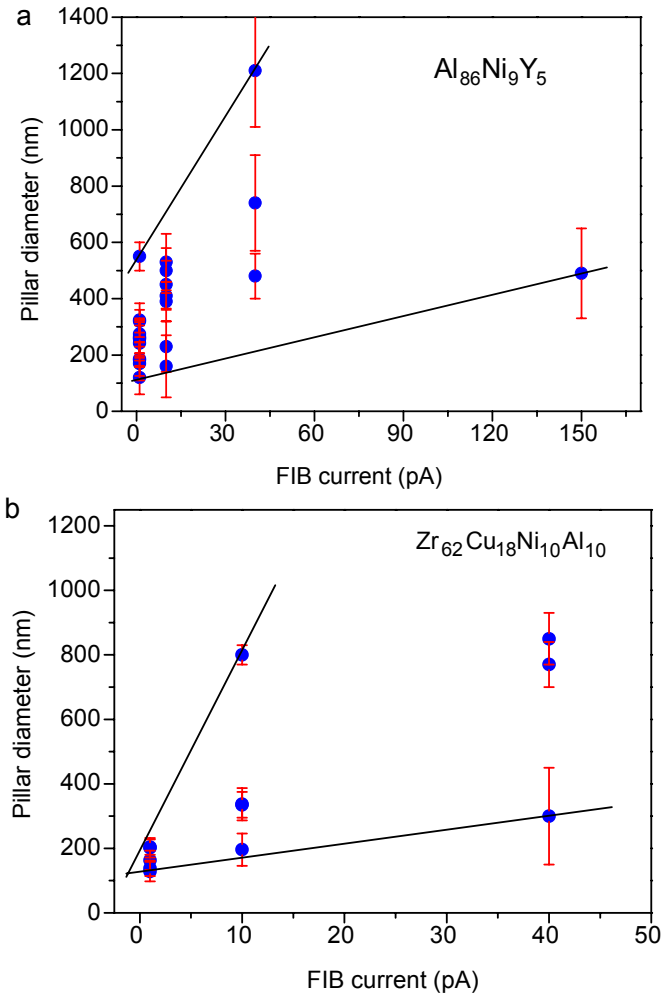

Fig. 3.5. Dependence of the pillar diameter vs. FIB current for MG pillars of different composition: (a) $Al_{86}Ni_9Y_5$ and (b) $Zr_{61.8}Cu_{18}Ni_{10.2}Al_{10}$. The red bars indicate the milling error measured in TEM

When a pillar is milled to a smaller diameter the cross section changes from polygonal to a more rounded shape. The cross-section area of regular polygons can be calculated according to their circum-circle of radius *r, touching* all the vertices of the polygon or apothem *a*, i.e. the line from the centre of the polygon at right angles to any of its sides

$$S_{polygon} = \frac{r^2 N \sin(2\pi / N)}{2} \tag{3.2}$$

$$S_{polygon} = a^2 N \tan(\pi / N) \tag{3.3}$$

where N is the number of sides of a polygon. The diagonal (*d*) of cross sections of a polygonal pillar is measured in the range of $2a \leq d \leq 2r$.
These simple geometric considerations show that the error between the measurements and the real values of the equivalent diameter of polygonal pillars is equal to $\pm r(1-\cos\pi / N)$.

Therefore, the error decreases with decreasing diameter and increasing the number of the polygonal section. For instance, changing the cross section from a square to an octagon, the error decreases from ±0.293*r* to ±0.076*r*.

Fig. 3.5 shows the dependence of the pillar diameter on the FIB current for the metallic glass (MG) pillars of different compositions. The error bars indicate the milling error. With decreasing pillar diameter the FIB current should be decreased so as to mill better shaped pillars. On the other hand the milling time also plays an important role in the preparation. By lowering the FIB current the milling time increases. Therefore, for the best performance, it is necessary to keep the suitable time range and to use the proper FIB currents for the different pillar diameters.

Indeed the difference in composition may also affect the details of the preparation process. In general harder (MG) materials will take longer but to reach smaller diameters a harder material is preferable, e.g. for Zr- based materials the smallest diameter was equal to 70 nm but for the Al-base MG only 120 nm was attained. This phenomenon is related to the limitations of the milling process itself. When the sizes of milled features approach tens of nanometers, the damage by Ga ions becomes more relevant. The softer the material the less accurate becomes the milling. The shape of the desired mill becomes rather out o control and not very much reproducible.

3.3.3 In-situ compression study of taper-free Cu-based metallic glass nanopillars

Taper-free pillars with relatively large diameters always show catastrophic shear banding following elastic deformation similar to that observed through testing slightly tapered pillars.[8-11] One example is shown in Fig. 3.6(a-b), where the pillar with 640 nm diameter shows an initial small local banding to accommodate the imperfect tip-punch contact and subsequently two major SBs are triggered simultaneously at a larger event.

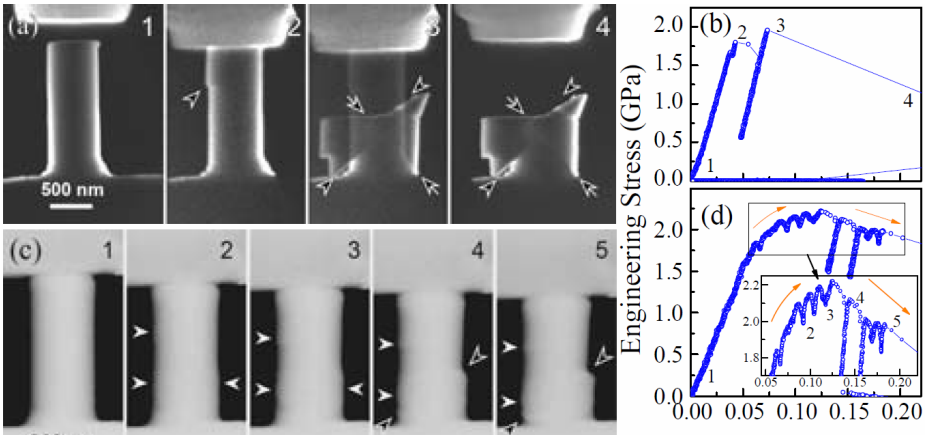

Fig. 3.6. Grabbed dark-filed TEM video frames showing the deformation of taper-free pillars of (a) 640 nm and (c) 365 nm diameter respectively under displacement controlled compression: the numbering of the video frames in (a) and (c) corresponds to the numbers marked in the stress-response curves in (b) and (d) respectively. Open and solid white arrows annotate shear bands and local bumps respectively.

Test of pillars with the diameter down to ~ 300 nm regime shows interesting new phenomena. For example, the deformation of a 365 nm taper-free pillar in Fig. 3.6(c) shows several features. First, it experienced large engineering strain up to 18%; second, the stress evolution is intermittent; third, the stress evolution is initially "hardening" up to 12.5% strain followed by softening as indicated in Fig. 3.6(d) and zoomed-in in the inset. The initial "hardening" is a result of a general "global fattening" effect that increases the effective load-bearing-area. The "hardenable" deformation however is not uniform, with jerky-type stress drops observable. But no transient shear processes corresponding to the jerky events are observed in the structure evolution; instead irregular local bumps are gradually developed at the

surface. The subsequent softening is due to the development of a nascent shear band [indicated by open-arrows in (c4) and (c5)] at the edge of a local bump that is developed prior to the "hardening" stage. It should be noted that the initial "hardening" is an intrinsic behavior. It is fundamentally different from the "hardening" observed in tapered pillars, where the stress gradient induced by the tapering promotes the formation of local SBs, i.e. the load increase is due to diameter increase associated to the tapered geometry. Also, the transient stress drops at the softening stage observed in Fig. 3.6(d) are associated to the arrest and re-initiation of the single SB, fundamentally different from that observed in bulk specimen due to interaction of many SBs. It can be interpreted in terms of elastically stored energy averaged to the shear plane which is proportional to the volume to area ratio (or D for constant L/D ratio) and thus not enough to drive the SB to propagate automatically at this size regime.

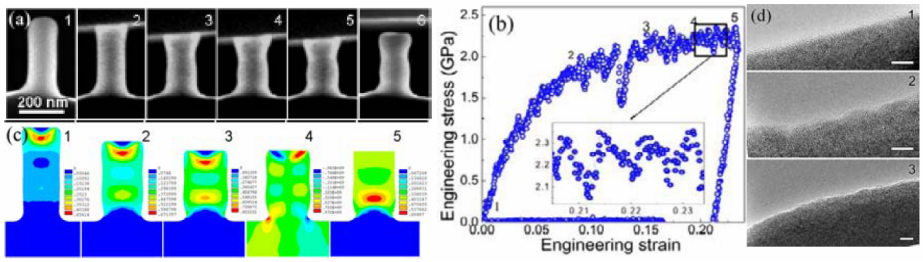

Fig. 3.7. Banding-less deformation of a 125 nm diameter pillar: (a) video frames grabbed at points 1 to 6 marked in the stress-strain plot in (b); (c) 3-D Finite Element Analysis Method FEA of the compression by treating the MG as an isotopic, elastic ideal–plastic solid, taking into account the rounded tip and the tip-punch friction, with (c1-3) being Mises-strain at different displacements and (c4) shear strain at the same displacement as in (3), (5) compression of a pillar with flat top and neglecting friction. (d) HRTEM showing atomically flat and clean surface of the as milled pillar (d1) and nanoscale inhomogeneity at the "necking" (d2) and "swelling" (d3) regions. Scale bar in (d) represents 5 nm.

Upon further decreasing the size to 120 nm level, the deformation becomes apparently fully homogenous. With the term "homogeneous" we mean that the deformation is smooth and banding-free (without band-like features), but not that the deformation is uniform throughout the pillar. In fact, the deformation is not completely uniform because of the tip-punch friction and the constraint at the base. Initially, a homogeneous bulging/swelling occurs at the top, with increasing displacement. The bulge does not extend downwards instead plastic flow starts in a virgin area far away from the tip where the side

surfaces continuously bow upon compression, producing a barrel-like shape leaving two seemingly "necking" regions at both ends. Importantly, a monotonic "hardening" is shown as a result of a continuous upsetting effect and lack of SBs.

Despite the apparent "hardening", the stress evolution is obviously still intermittent with transient load-drops present in Fig. 3.7(c). The intermittency is presumably a result of very tiny local transitions distributed throughout the pillar, which would not have been detected without ingenious quantitative test and fast enough machine response.

They do not organize into a shear band or cause observable band-like local deformation. By this mechanism, very large engineering strain can be obtained without any indication of damage.

The phenomenon of barreling is often a signal of good plasticity. 3-D finite element analysis was performed and the result shows that, by treating the material as an isotropic elastic-plastic body characteristic of homogeneous plastic flow, the deformation of the MG nanopillars can be satisfactorily predicted (Fig. 3.7 b). The local deformation at the tip of a pillar can be interpreted either by friction or by the rounded tip, or a combination as a result of developed local large shear stress shown in Fig. 3.7(b4). The continuous barreling and fattening is more likely due to the constraint at the base and shear stress concentration especially. This is further confirmed by simulating a specimen with a flat top by neglecting the friction in Fig. 3.7(b5). Barreling was previously observed only in compression of some bulk MG-based composites containing nanocrystallites, where the barreling was accommodated however by well-developed profuse shear bands whose nucleation, distribution and propagation is influenced by the embeded nanocrystallites.[52]

High resolution TEM (HREM) confirmed the atomically flat surface of the as-milled pillars free of surface redeposition (Fig. 3.7d) and the band-free deformation characteristics. It also revealed nanoscale surface modulations associated to local deformation domains of a few nanometer size at either the "bowing out" region or the "necking" region as shown in Fig. 3.7(d2) and (d3), respectively.

The intermittency becomes clearly less observable in compression of a thinner pillar with 100 nm diameter in Fig. 3.8(a), and eventually disappeared in Fig. 3.8(b) for the 70 nm pillar leading to a fully smooth stress response, despite the fact that an initial slight misalignment results in reduced barreling effect in the 100 nm pillar while a geometric imperfection leads to

bending/buckling of the 70 nm pillar at a later stage, indicating extreme sensitivity of the test to external perturbation at this size scale.

The detailed microscopic processes of individual STZs towards the formation of macroscopic SBs have not been visualized directly yet. However, the present results provide strong support that, microscopically, a larger volume upon plastic yielding has a higher probability to develop larger flow defects (or percolation of flow defects), which are associated to larger jerky events and shear banding in micrometer size pillars.

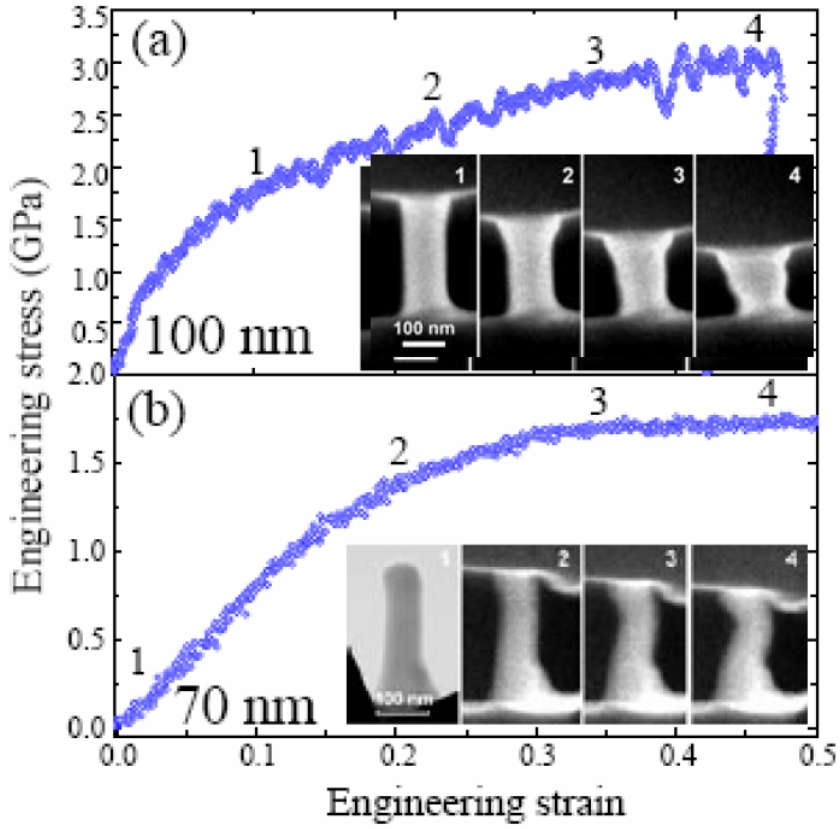

Fig. 3.8. Stress and structure evolutions of nanopillars with diameters of (a) 100 nm and (b) 70 nm respectively: The 100 nm pillar still shows noticeable transient stress-drops, and the slightly developed misalignment in loading reduced the barreling effect; the stress evolution in the 70 nm pillar is completely smooth without intermittency, however, a slight geometric imperfection (curved shape) induces bending in the later stage of deformation and thus much lower engineering stress.

Upon decreasing the size of the pillars, smaller local shear processes (flow defects) become critical and they lead to less inhomogeneous

deformation. The deformation is still intermittent and may develop to shear bands at ~ 300 nm, but becomes banding-free though still intermittent when the system approaches 100 nm scale. It ultimately changes to fully smooth and continuous plastic flow at sub-100 nm scale. Such a picture of flow defect distribution is reminiscent of flaws/cracks (preexisting and stress-induced) commonly observed in many alloys and ceramic systems, whose behaviors can be described, e.g., by Weibull statistics (WS), depending on the size distribution of the defects.[53] Active simulation studies of microscopic processes and dynamics of local transitions in MGs indeed suggested an inhomogeneity of local mechanical response in MGs and an influence of the system size (2-D or 3-D) on the size of the local processes although no general scaling laws have been proposed. We may tentatively assume that the size of the critical flow defects *a* in MGs statistically follows the same scaling law with the volume *V,* as normally assumed in Weibull materials, where *a* described as

$$a \propto V^m, \tag{3.4}$$

with *m* being a constant.[54]

To statistically get such a scaling law, intrinsically it requires that smaller flow defects have a much higher relative density (number per unit volume) in the material. Such a dependence can be represented by a size distribution function describing the relative density in terms of size of the flow defects. A function of a simple form

$$g(a) = g_0 \left(\frac{a}{a_0} \right)^{-r} \tag{3.5}$$

has been shown to be intrinsically consistent with Eq. (1), where a is the size of a flow defect, g_0, a_0 are materials related constants, r is related to m through $m = 2(r\text{-}1)$. Eq. (3.5). Assuming a_c being the size of smallest critical flow defects that directly contribute to the global plasticity, for evenly distributed flow defects, the total density (number) of critical flow defects is expressed as

$$\rho(a_c) = \int_{a_c}^{\infty} g(a)da = \frac{a_c}{(r-1)} g(a_c). \tag{3.6}$$

Here, a_c is determined by Eq. (3.4) and scales with the volume of the specimen. Noticing that, with the size approaching zero, g(a) goes

unreasonably to infinity, one expects that the actual density distribution of flow defects smaller than individual STZs (e.g. <1 nm) may deviate from Eq. (3.5) . However, such a deviation may not influence the analysis based on Eq. (3.5), since defects smaller than the critical value a_c do not remarkably influence the phenomena.

3.3.4 In-situ compression study of taper-free Zr-based metallic glass nanopillars

Fig. 3.9 shows a sequence of frames grabbed from in-situ recorded video of the compression of a $Zr_{61.8}Cu_{18}Ni_{10.2}Al_{10}$ pillar with a relatively large tip diameter of 460 nm which was compressed under displacement rate control.

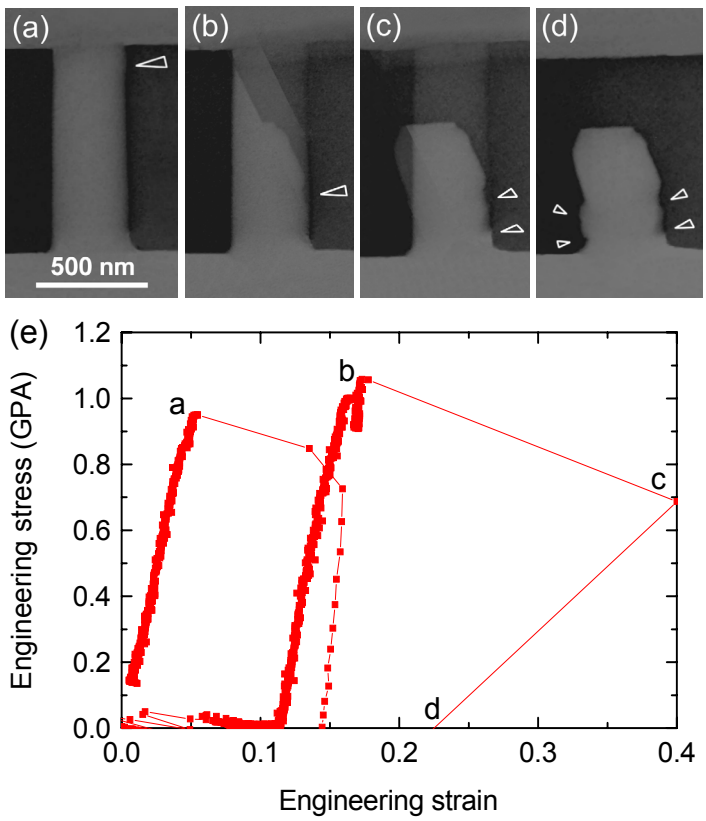

Fig.3.9 (a–d) Grabbed TEM video frames recording the deformation of a ø460 nm $Zr_{61.8}Cu_{18}Ni_{10.2}Al_{10}$ MG taper-free pillar compressed under displacement-rate controlled mode, corresponding respectively to the deformation structure marked on the load–displacement curve (e). Open white arrows annotate shear bands in pillars during and after compression.

Due to the friction between the top part of the pillar and the indenter when deformation starts, small shear (Fig. 3.9a) appears in the top part of pillar, subsequently two major and one top SBs are triggered simultaneously at a larger event (Fig. 3.9b and 3.9c). They occur rapidly with a speed beyond the recording speed of the camera. With decreasing pillar diameters, the deformation behavior continues by showing shear banding. However, the amplitude of load drops, which represent a shear band displacement, decreases significantly. In pillars with diameter of about 150 nm we observe no major or large shear displacements. It is considered that this diameter is the transition point between inhomogeneous and homogeneous behavior of pillar response to compression.

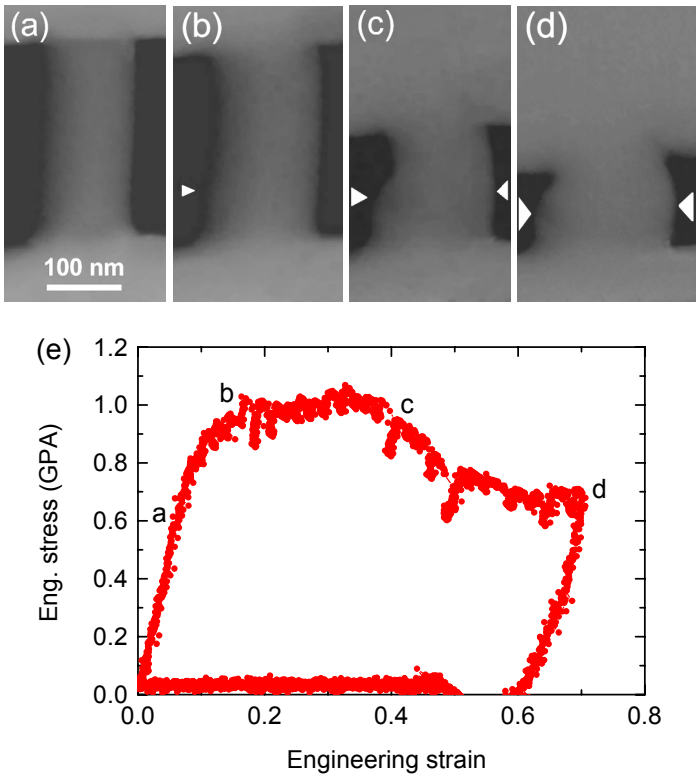

Fig. 3.10 (a–d) Grabbed TEM video frames recording the deformation of a ø140 nm $Zr_{61.8}Cu_{18}Ni_{10.2}Al_{10}$ MG taper-free pillar compressed under displacement-rate controlled mode, corresponding to different strain values marked in the load–displacement curve (e). Filled white arrows annotate bulging areas in pillars during compression. Sizes of arrows correspond to different bulging volumes.

Fig. 3.10 shows the video frames recording the compressive deformation of a ø140 nm pillar. Bulging was observed at about one third of its height close to

the base and continued with increasing displacement. The deformation reached an engineering strain up to 70 % without any visible shear banding or offset (Fig. 3.10 c and 3.10 d), but rather homogeneous flow at this scale. This phenomenon is in contradiction to the deformation behavior of pillars with large sizes (> ø 300 nm), which showed an engineering strain not larger than 5% before a major shear displacement occurs.

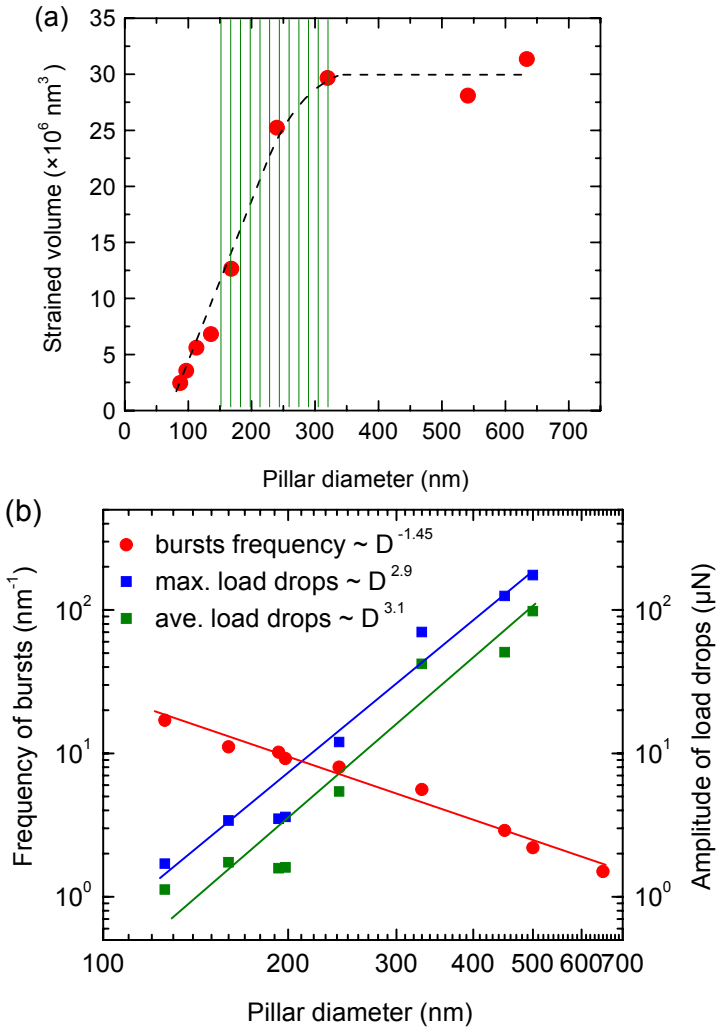

Fig. 3.11 (a) Elastic strained volume versus pillar diameter of $Zr_{61.8}Cu_{18}Ni_{10.2}Al_{10}$ MG. (b) Mechanical characteristics and quantitative analysis as a function of pillar diameter: frequency of bursts and the amplitude of lord drops.

Fig. 3.11a displays the elastically strained volume before shear banding versus the diameter of pillars. Assuming the same yielding strength of STZs, the stored energy in the elastically strained volume needed to initiate the first major shear banding is the same. It indicates that as soon as STZs concentration per volume unit is enough, major shear displacement occurs.

However, we do not observe homogeneous deformation in large samples. Large pillars from 600 nm down to around 300 nm in diameter show an elastic deformation followed by a jerky-type deformation with transient shear banding events registered with large load drops in the load–displacement curve (see Fig. 3.9e), which are analogues to the intermittent bursts or slip avalanches observed in crystalline materials with a power-law size distribution.[55,56] With decreasing pillar diameter the apparent deformation mode shows a gradual transition from highly inhomogeneous to homogeneous behavior, as indicated by the hatched zone in Fig. 3.11a. The yield stress of all the pillars tested is size-independent, which is consistent with our previous work on tapered pillars.[44] The frequency of bursts increases rapidly with decreasing pillar diameter (power-law, Fig. 3.11b). It indicates more frequently activated shear banding events, whereas the shear displacement carried by individual shear banding events decreases quickly, indicating suppression of shear band propagation.

The observed load drops at constant displacement rate are triggered by the formation and propagation of multiple shear bands. Amplitudes of load drops (LDs) reveal that the shear displacement in thinner pillars proceeds more smoothly, while the stress decreases more steadily. At the smallest diameter of 110 nm, the amplitude of LDs is very small (~2 μN), whereas maximum load is still considerably high (~ 10 μN). The ratio between average LD and maximum load for ~100 nm pillars equals 8-10. This ratio decreases down to 1 for larger pillar diameters, which shows the propagation of a major shear band to the edge of the pillar. This is caused by changes in the mechanism of plastic behavior with decreasing pillar diameter. During compression of micrometer sized pillars ductility appears due to distinctive structure of the BMGs. The shear transformation zones occur preferentially in soft regions in BMGs and evolve into shear bands upon loading. Consequently, numerous shear-band nuclei are formed concurrently in the soft regions. Because the soft regions cannot carry much plastic strain due to shear band multiplication processes, any further deformation has to proceed in hard regions so that higher plasticity is still attainable on a large scale. With pillar

size on the scale of hundred of nanometers, this mechanism is no longer applicable, due to the decrease of the quantity and interaction of soft regions.

3.4 Conclusions

A new method to prepare sub-micrometer sized and nanometer sized pillars with a high aspect ratio that is suitable for mechanical testing was developed. This method allows avoiding of all FIB milling artifacts including tapering, while preparing amorphous nanopillars. A comparison of two different MG compositions, $Zr_{61.8}Cu_{18}Ni_{10.2}Al_{10}$ and $Al_{86}Ni_9Y_5$, reveals the milling time procedure and shed lights on the FIM limitations when milling down to tens of nanometers. The proper procedure of the pillars preparation with respect to the time of milling, accuracy of the shape and proper FIB current selection was revealed. The unique method determines accurately the cross-section of each pillar which is essential for the accurate mechanical testing, especially stress strain measurements.

We have applied the novel preparation method to various BMG with different chemical composition and at various sizes. In-situ compression tests of taper-free micro-/nano-pillars of $Zr_{61.8}Cu_{18}Ni_{10.2}Al_{10}$ MG with tip diameters ranging from 600 to 90 nm show predominant inhomogeneous and intermittent plastic flow characterized by shear banding events. The deformation is defect-nucleation-controlled in larger pillars but becomes propagation-controlled in smaller pillars. Pillars with a diameter smaller than 150 nm show a homogeneous flow behavior without shear banding during compression. It is concluded that larger overlap of stress fields of flow defects in smaller pillars (samples) plays a crucial role for the ductile behaviour. Quantitative analysis of load-displacement curves have revealed a strong size effect of nanopillars under compression and confirmed the existing of transition threshold.

References

1. A. Donohue et al., Applied Physics Letter 91 (2007).
2. D. C. Hofmann et al., Nature 451, 1085 (2008).
3. C. C. Hays, C. P. Kim, and W. L. Johnson, Physical Review Letters, 84, 2901 (2000).

4. F. Delogu, Physical Review B 79(18), 184109 (2009).
5. N. P. Bailey et al., Physical Review Letters 98, 095501 (2007).
6. H. G. E. Hentschel et al., Physical Review Letters 104, 025501 (2010).
7. C. J. Lee, J. C. Huang, and T. G. Nieh, Applied Physics Letters 91, 161913 (2007)
8. C. A. Volkert, A. Donohue, and F. Spaepen, Journal of Applied Physics 103, 083539 (2008)
9. C. Q. Chen, Y. T. Pei, and J. T. M. De Hosson, Acta Materialia 58, 189 (2010).
10. B. E. Schuster et al., Acta Materialia 56, 5091 (2008).
11. A. Dubach et al., Scripta Mater 60, 567 (2009).
12. Z. W. Shan et al., Physical Review B 77, 155419 (2008).
13. H. Guo et al., Nature Materials 6, 735 (2007).
14. D. C. Jang, and J. R. Greer, Nature Materials 9, 215 (2010).
15. J. H. Luo et al., Physical Review Letters, 104, 215503 (2010).
16. J. C. Ye et al., Nature Materials 9, 619 (2010).
17. R. Seliger, J.W. Ward, Wang, V. and Kubena, R.L. (1979. Applied Physics Letters 34 (5): 310.
18 Principe, E L; Gnauck, P; Hoffrogge, P (2005). Microscopy and Microanalysis (2005), 11 : pp 830-831
19. S. Khizroev, R. Chomko and D. Litvinov, Nanotechnology 15, *S575-S584* (2004).
20. Orloff, J. and Swanson, L., (1975) J. Vac. Sci. Tech. 12 (6): 1209
21. L. Holzer, F. Indutnyi, P.H. Gasser, B. Münch and M. Wegmann, Journal of Microscopy 216, 84–95 (2004).
22. J. Mayer, Lucille A. Giannuzzi, T. Kamino, and J. Michael, Materials Research Society bulletin 32, 400-407 (2007).
23. S. Shukla , S. Seal, J. Akesson, R. Oder, R. Carter, Z. Rahman Applied Surface Science 181 (2001) 35 – 50
24. C.A.Volkert and A.M. Minor, Materials Research Society bulletin 32(5), 389–399 (2007).
25. O.V. Kuzmin, Y.T. Pei, J.Th.M. De Hosson, Applied Physics Letters 98, 233104 (2011).
26. J. Orloff, Journal of Vacuum Science & Technology B: Microelectronics and Nanometer Structures 14 (6), 3759 (1996).
27. J. Gupta, J. M. E. Harper, J. L. Mauer IV, P. G. Blauner, and D. A. Smith, Applied Physics Letters 61, 663 (1992).
28. C.Q. Chen, Y.T. Pei, J.Th.M. De Hosson, Acta Materialia 58, 189–200 (2010).
29. O.V. Kuzmin, Y.T. Pei and J.Th.M. De Hosson, Scripta Materialia 67, 344-347 (2012).
30. C.Q. Chen, Y.T. Pei, O. Kuzmin, Z.F. Zhang, E. Ma, J.Th.M. De Hosson, Physical Review B 83, 180201(R) (2011).
31. J. Th. M. De Hosson, Microscopy Research Techniques 72, 250 (2009).
32. J. Th. M. De Hosson, C. Q. Chen, Y. T. Pei, V. Ocelik, D. Matthews, TMS Annual Meeting Exhibition (2010).
33. C. G. Tang, Y. Li, K.Y. Zeng, Materials Letters 59, 3329 (2005).
34. Z. W. Shan, J. Li, Y. Cheng, A. Minor, S. A. Syed Asif , O. L. Warren, et al. Physical Review B 77, 155419 (2008).
35. Q. Zheng, S. Cheng , J. Strader , E. Ma, J. Xu, Scripta Materialia 56, 161 (2007).

36. C. Lee, J. Huang, T. Nieh, Applied Physics Letters 91, 161913 (2007).
37. S. Cheng, X. Wang, H. Choo, P. Liaw, Applied Physics Letters 91, 201917 (2007).
38. B. Schuster, Q. Wei, M. Ervin, S. Hruszkewycz, M. Miller, T. Hufnagel and K. T. Ramesh, Scripta Materialia 57, 517 (2007).
39. Y. Lai, C. Lee, Y. Cheng, H. Chou, H. Chen, X. Du, C. I. Chang, J. C. Huang, S. R. Jain, J. S. C. Jang, and T. G. Nieh, Scripta Materialia 58, 890 (2008).
40. C. Volkert, A. Donohue, F. Spaepen. Journal of Applied Physics 103, 083539 (2008).
41. B. Schuster, Q. Wei, T. Hufnagel, K. Ramesh, Acta Materialia. 56, 5091 (2008).
42. A. Dubach, R. Raghavan, J. Loffler, J. Michler, U. Ramamurty. Scripta Materialia 60, 567 (2009).
43. C. Q. Chen, Y. T. Pei, J. Th. M. De Hosson, Acta Materialia. 58, 189 (2010).
44. C. Q. Chen, Y. T. Pei and J. Th. M. De Hosson, Philosophy Magazine Letters 89, 634 (2009).
45. J. J. Lewandowski, W. H. Wang and A. L. Greer, Philosophy Magazine Letters 85, 78 (2005).
46. A. L. Greer, and E. Ma, Materials Research Society bulletin 32, 611 (2007).
47. C. A. Schuh, T. C. Hufnagel, and U. Ramamurty, Acta Materialia 55, 4067 (2007).
48. A. S. Argon, Acta Metallurgica 27, 47 (1979).
49. M. L. Falk, and J. S. Langer, Physical Review E 57, 7192 (1998).
50. W. L. Johnson, and K. Samwer, Physical Review Letters 95, 195501 (2005).
51. O.V. Kuzmin, Y.T. Pei, C.Q. Chen and J.Th.M. De Hosson, Acta Materialia. 60 (2012) 889.
52. J. Das et al., Physical Review Letters 94, 205501 (2005).
53. W. Weibull, Journal of Applied Mechanics 18, 293 (1951).
54. R. Danzer, J Eur Ceramic Society 26, 3043 (2006).
55. J. E. Carsley, A. Fisher, W. W. Milligan and E. C. Aifantis, Metallurgical and Materials Transactions 29A, 2261 (1998).
56. M. Zaiser and E. C. Aifantis. International Journal of Plasticity 22, 1432 (2006).

Chapter 4

Intrinsic and extrinsic size effects of taper free metallic glass nanopillars

This chapter demonstrates that the chemical composition as well as the variation of bulk modulus and Poisson's ratio may affect the deformation mode and ductility of metallic glasses at the nanoscale. The lower the shear modulus over bulk modulus ratio, the larger pillar diameter above of which more brittle behavior occurs was found.

Nano-sized pillars with diameters ranging from 90 to 600 nm of four amorphous alloys $Cu_{47}Ti_{33}Zr_{11}Ni_6Sn_2Si_1$, $Zr_{50}Ti_{16.5}Cu_{15}Ni_{18.5}$, $Zr_{61.8}Cu_{18}Ni_{10.2}Al_{10}$ *and* $Al_{86}Ni_9Y_5$, *were fabricated and tested in-situ in a transmission electron microscope (TEM). Differences among the deformation behavior of tapered (1.5 - 3°) and taper-free systems are also discussed. Upon increasing size all the MGs examined show a transition from ductile–to-brittle behavior under compression, where the transition point, however, depends on the chemical composition of the specific metallic glass. A micromechanical model is presented in detail to explain the various dependencies.*

4.1 Introduction

Metallic glasses are currently the focus of extensive studies in view of their potential applications.[1,2] Tremendous efforts have been dedicated to characterize, understand, and possibly control the atomic and micro- scale mechanisms underlying the unique properties of MGs, e.g. the very high yield strength but near zero plasticity at room temperature. One of the explanations of the deformation behavior in MGs under applied stresses is related to the movements of the shear transformation zones (STZs). According to this hypothesis, the basic carriers of plasticity in MGs are STZs, each of which is a local atomic region containing tens to hundreds atoms and embedded within an elastic medium.[3-5] However, the dynamics and correlation of the local flow units, and their spatiotemporal evolution into macroscopic shear bands (SBs) are still under drastic debate. Whether STZs exist or how they manifest in

deformation still remains unsettled. In our view the dynamical (stochastic) and collective interactions among defects, essentially characterized by density fluctuations that produce local stress fluctuations in a MG, are responsible for intrinsic versus extrinsic size effects.

So far, size effects on mechanical properties have been widely investigated in different kinds of materials, including polycrystalline and single-crystalline metals, polymers and concretes. Size effects in plasticity of crystalline metals have been investigated to a large extent, at least for pure metallic systems and size-dependent strengths have been reported in nanoindentation, micro-torsion, micro-bending, and micro-compression experiments, and were attributed to different phenomena, e.g. hardening by geometrically necessary dislocations, dislocation interactions with surfaces, and dislocation starvation. For a recent review reference is made to.[6] Size effects in the mechanical behavior of metallic glasses have received less attention. At low homologous temperatures relative to the glass-transition temperature plastic deformation in MGs occurs inhomogeneously with the strain being localized within a small number of discrete shear bands.[7] Strain softening is believed to be the reason for this localization. Although the strain in the shear bands can be quite high, the overall ductility of bulk MGs is low, and MGs typically fracture by massive shear-off along the shear bands. Strain softening is not unique and not limited to metallic glasses. In general, if strain softening accompanies the generation of the initial shear bands, one would expect a substantial machine spring-back when MGs are tested, similar to that observed in whisker tests. But there is a substantial difference between crystalline and amorphous materials: work hardening in crystalline metals eventually takes over after a possible initial period of strain softening, whereas in MGs work hardening typically does not develop. Consequently, it raises the following question: is there a transition from unstable shear band propagation to homogeneous yet ductile deformation with decreasing specimen size of MGs?[8,9,10,11,12]

So far a major drawback of experimental research on pillars is that almost all ex situ deformation followed by post-mortem microscopy does not allow a direct observation of the microstructure during mechanical loading and thus lacks the possibility to monitor deformation events and the evolution of microstructures as the deformation proceeds.[13] In addition, the microstructure observed after deformation is generally different from that of the material under loading, due to recovery during and after unloading.[14]

Furthermore, the appearance of a tapering angle due to the focused ion beam (FIB) milling procedure may have a large influence on the deformation behavior and stress/strength measurements of nanopillars under compression test (see paragraph 3.3.2). It is notable that tapering is inevitable for FIB milled pillars with diameters down to less than 300 nm. The tapering might be critical for MG pillars as shear band initiation mostly occur close to the corner of the top surface where the pillar has the least cross-sectional area due to tapering effects. This stress concentration is further intensified by possible frictional forces between the top surface of the pillar and the flat punch indenter. This affects not only SB nucleation but also makes stress analysis rather difficult.[15] This is especially so for the ex-situ experiments when the events in the stress-strain curve cannot be correlated to particular individual SBs through in-situ microscopy observations.

In this study, we investigate the size dependence of the deformation behaviors of four amorphous metallic glasses: $Cu_{47}Ti_{33}Zr_{11}Ni_6Sn_2Si_1$, $Zr_{50}Ti_{16.5}Cu_{15}Ni_{18.5}$, $Zr_{61.8}Cu_{18}Ni_{10.2}Al_{10}$, and $Al_{86}Ni_9Y_5$. Tapered and taper-free MG nanopillars with diameters down to sub-100 nm are made and tested quantitatively in-situ inside a transmission electron microscope. The major consideration of compositional variation was the change of bulk modulus and Poisson's ratio that may affect the deformation mode and ductility of MGs at the nanoscale. Lewandowski et al [16] suggested that the ratio between the shear modulus and bulk modulus is a relevant parameter to categorize intrinsic brittle behavior of bulk metallic glasses, i.e. the higher the ratio or the smaller the Poisson's ratio the more brittle the material may behave. This was taken as a starting point in our choice concerning materials addressing the questions whether also at smaller dimensions the ductile-to-brittle transition will depend on that ratio and whether a size effect will exist. In particular, we present some striking results on the ductile-brittle transition as a function of the MG composition that have not been observed before.

4.2 Experimental

MG of different alloy systems and compositions were selected: one Cu-based alloy, two Zr-based alloys and one Al-based alloy, i.e. $Cu_{47}Ti_{33}Zr_{11}Ni_6Sn_2Si_1$, $Zr_{50}Ti_{16.5}Cu_{15}Ni_{18.5}$, $Zr_{61.8}Cu_{18}Ni_{10.2}Al_{10}$ and $Al_{86}Ni_9Y_5$. A first set of experiments had been carried out on nanopillars tapered due to FIB milling.[15, 17] They were cut by focused ion beam (FIB) from two MG ribbons: $Cu_{47}Ti_{33}Zr_{11}Ni_6Sn_2Si_1$ and $Zr_{50}Ti_{16.5}Cu_{15}Ni_{18.5}$, as shown in Fig. 4.1a.

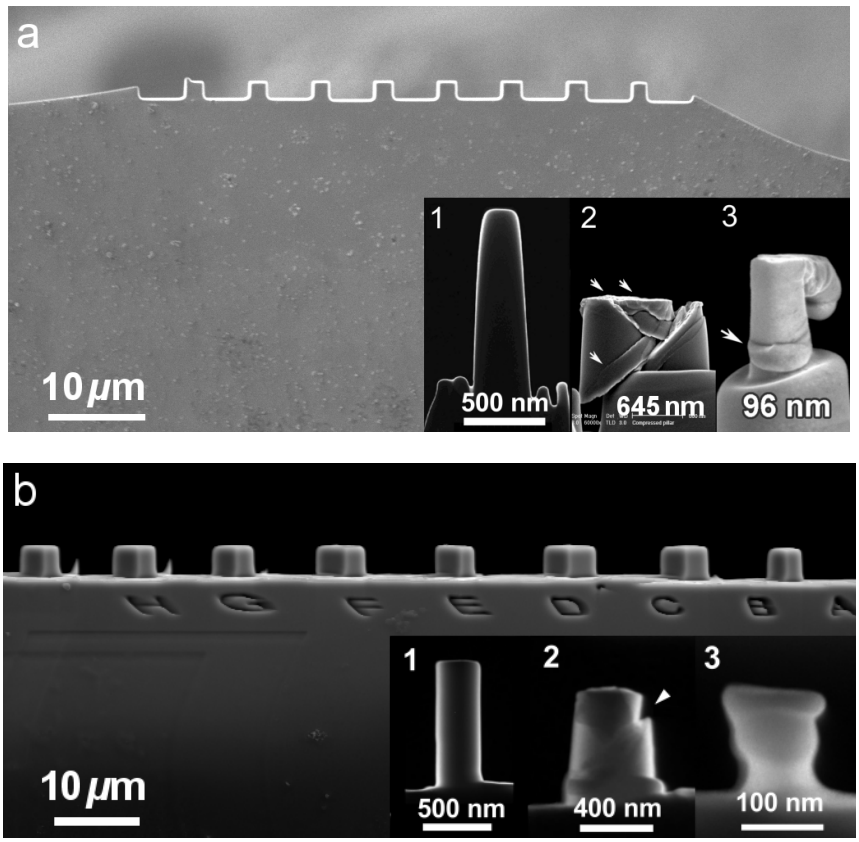

Fig. 4.1. FIB milling procedure of tapered (a) and taper-free pillars (b) with the insets showing nanopillars before compression (a1, b1) and after compression of large diameter pillars (a2, b2) and small diameter pillars (a3, b3).

More than 40 pillars of tip diameters ranging from 93 to 645 nm were studied. Despite having relatively small taper angles between 2.0° and 3.5°, these compression tests showed several drawbacks of tapered pillars, such as difficulties in stress measurements due to stress gradient, nucleation of highly localized shear bands (SBs) always at the corner of sample-plunger contact during compression.

Taper-free nanopillars were produced thereafter by using an in-house developed FIB milling procedure with a dual beam FIB-SEM microscope (Lyra, Tescan, CZ). Microwedges were prepared by mechanical polishing out of selected MG ribbons with the length about 100 μm and thickness 2-5 μm. First a series of rectangular microsized beams were milled on the microwedge. Then out of these beams nanopillars were fabricated step-by-step with decreasing FIB current at different milling stages (see chapter 3). A

set of taper-free nanopillars with diameters ranging from 90 to 600 nm and aspect ratios of around 4 was fabricated by a combination of top and side FIB milling (Fig. 4.1b). The uniform amorphousness of the nanopillars was confirmed by X-ray analysis and TEM observations (Fig. 4.2).

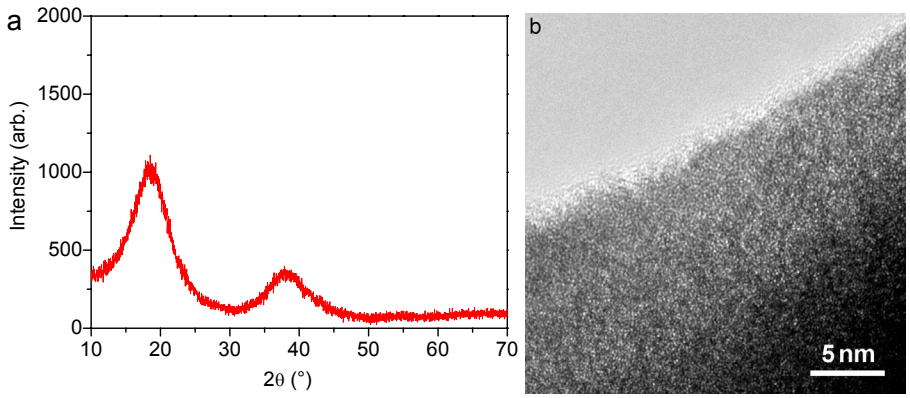

Fig. 4.2. X-ray diagram of $Zr_{61.8}Cu_{18}Ni_{10.2}Al_{10}$ MG ribbon (a), HRTEM picture of the pillar before compression.

In-situ TEM compression experiments were performed using a Hysitron picoindenter TEM holder (Hysitron Inc., Minneapolis, MN, USA) equipped on JEOL 2010F TEM, with a diamond flat punch of 2 μm in diameter. A similar approach has been recently used in the investigation of the incipient plasticity of thin metallic films[18],[19] and crystalline pillars.[20] The indenter has several unique features, which are particularly critical to the present study. First, it is integrated with a miniature capacitive load–displacement transducer permitting high resolution load and displacement measurements (resolution of ~0.3 μN in load, ~1 nm in displacement). In addition, a rapid instrument response and data acquisition rate (the controller is operating in a continuous loop and sampling data at 20 kHz) allows discrete flow events to be well-resolved. The experiments ran in two typical control modes: displacement control, which shows a great sensitivity, and load control, which has an advantage in evaluating sudden displacement jumps (SB offset). The displacement and/or load rate are programmed in such a way that a nominal strain rate of ~ 10^{-2} s^{-1} is applied.[21] Together with the high data acquisition rate, this all makes it possible to evaluate the development of a single SB event, which was found to be strongly size dependent.[15, 22]

4.3 Results and discussion

4.3.1 Transition from inhomogeneous shear banding to homogenous flow with deceasing pillar size

Fig. 4.3a shows a sequence of frames grabbed from a video that records the compression of a taper-free $Zr_{50}Ti_{16.5}Cu_{15}Ni_{18.5}$ MG pillar.

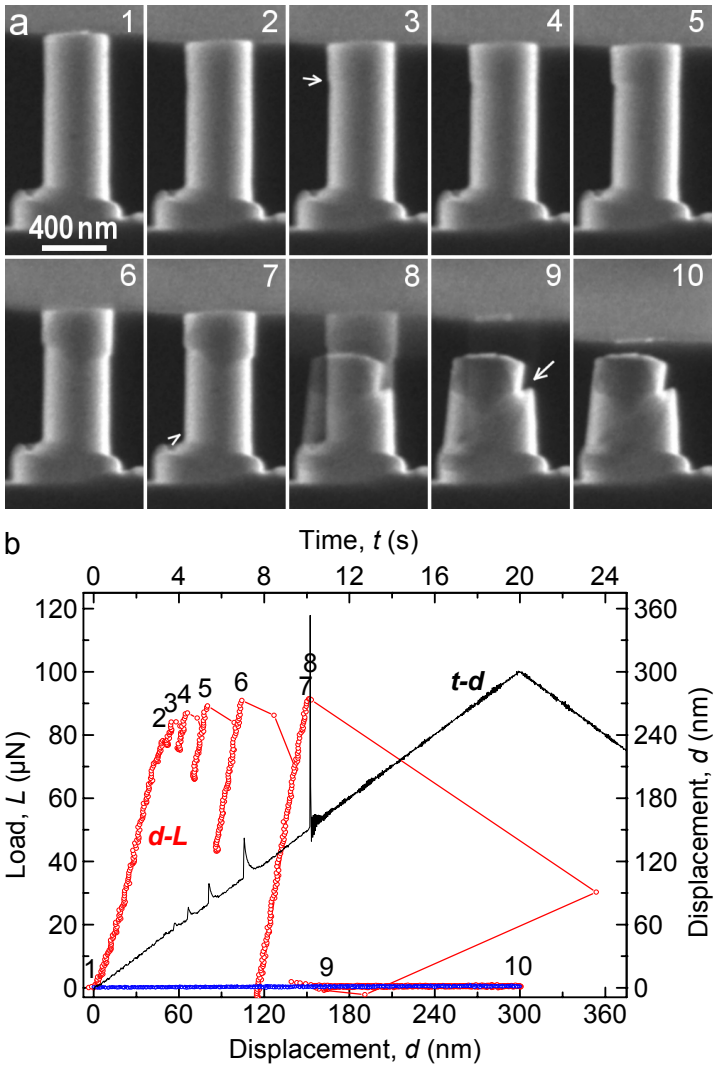

Fig. 4.3. (a) Dark-field TEM images (video frames) showing the deformation evolution of a $Zr_{50}Ti_{16.5}Cu_{15}Ni_{18.5}$ MG pillar of 410 nm diameter, with the arrows indicating major shear banding and its offset; (b) the time-displacement and displacement-load curves with the numbered instance corresponding to the frames in (a). The unloading curve is colored in blue for distinguishing from the loading curve in red.

The pillar has a relatively large diameter of 410 nm and was compressed under displacement-rate control. The pillar shows initial elastic deformation followed by jerky type deformation with transient shear banding events registered with large load drops in the displacement-load curve (Fig. 4.3b).

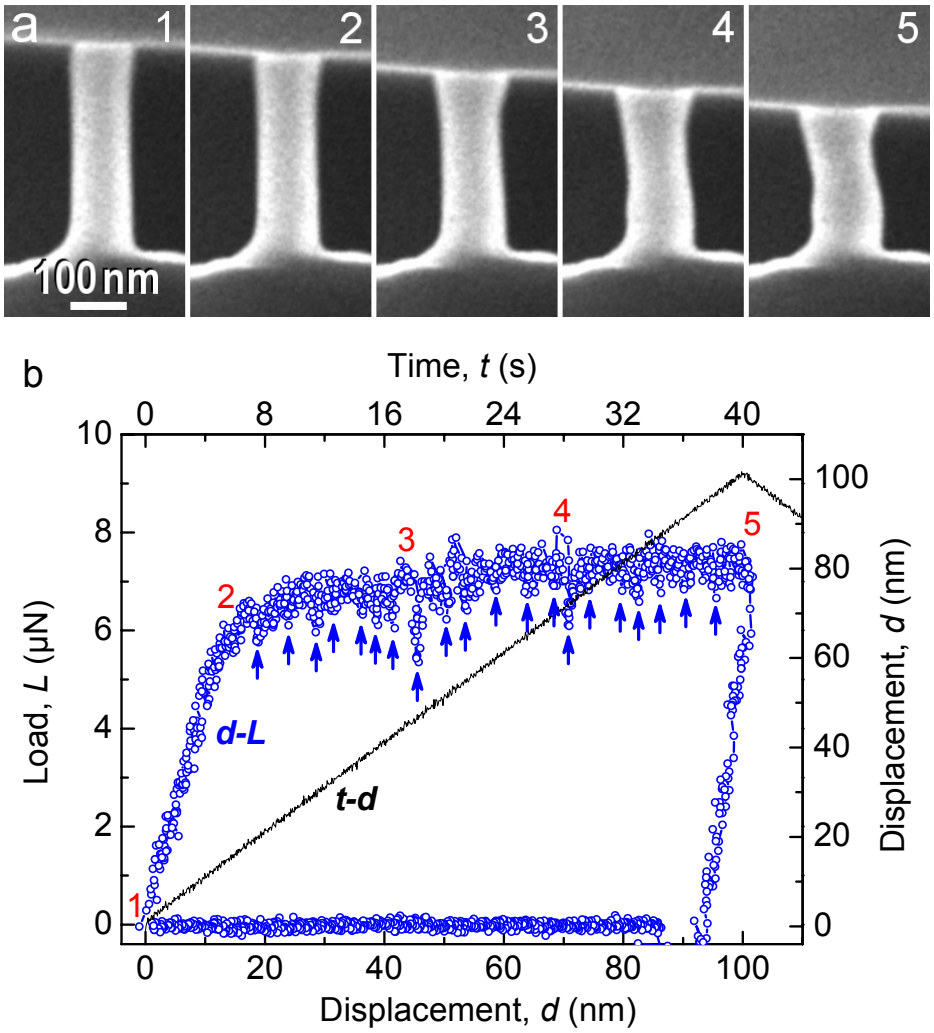

Fig. 4.4 (a) Dark-field TEM images (video frames) showing the deformation evolution of a $Zr_{50}Ti_{16.5}Cu_{15}Ni_{18.5}$ MG pillar of 112 nm diameter; (b) the time-displacement and displacement-load curves with the numbered instance corresponding to the frames in (a).

These shear bands propagate very fast and leave the punch moving behind at the programmed displacement rate, appearing in the form of displacement burst or sharp peaks in the time-displacement curve and

resulting in transient unloading (load drop). Taper-free pillars with relatively large diameters always show catastrophic shear banding, similar to that observed in slightly tapered pillars.[23] The clear difference is that the shear bands may nucleate at any height of taper-free pillars where large flow defects are triggered at loading. In contrast, the shear bands in tapered pillars always occur at the top corner due to the stress gradient along the pillar axis.

Upon decreasing the pillar diameter, the amplitude of the load drops reduces but their frequency increases rapidly. Fig. 4.4b presents the displacement-load and time-displacement curves of a ø110 nm diameter pillar of the same MG material. The amplitude of the load drops is so small that the drops are hardly visible but they can still be recognized in a closer view as indicated by the arrows in Fig.4.4b. Accordingly, there was neither any single offset observed in relation to shear banding with in-situ TEM observation nor any peak seen in the time-displacement curve. Instead, only continuous plastic flow was observed in the entire pillar, as shown in Figs. 4.4a. The deformation is still intermittent but becomes morphologically banding-free, i.e., without observable shear banding and shear offset, when the system approaches a threshold size. These in-situ compression tests on taper-free pillars confirm our previous finding with tapered pillars that the apparent deformation mode of MG pillars exhibits a transition from highly inhomogeneous to relatively homogeneous upon decreasing the sample size.

4.3.2 The influence of pillar tapering geometry on deformation behavior

As argued already tapering (see chapter 3.3.1) is a serious problem in investigating the deformation behavior of micro-pillars under compression. Investigations of the deformation behavior of nanopillars under compression testing become difficult due to the nucleation of highly localized SBs preferentially at the corner of sample-plunger contact, although also macroscopic samples without taper exhibit shear initiation at the corner of the sample-to-anvil interface. Tapering affects not only SB nucleation but also makes stress analysis rather difficult. The number of bursts of taper-free and tapered pillars shows a large difference, see Fig. 4.5a.

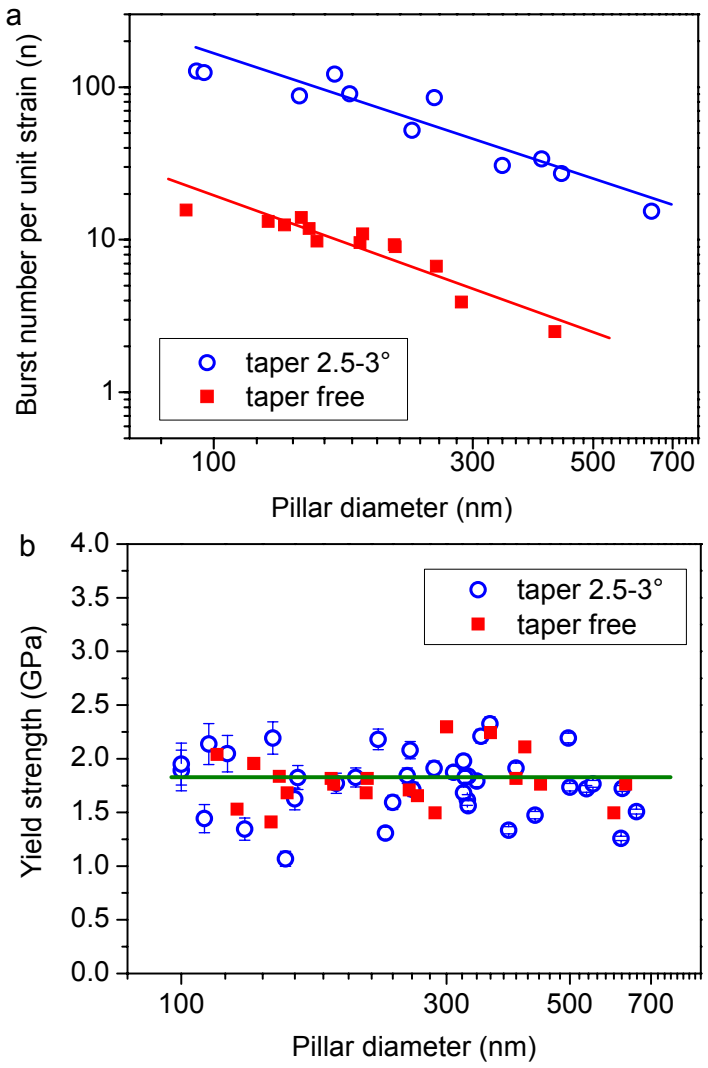

Fig. 4.5. Comparison of mechanical response of tapered and taper-free $Cu_{47}Ti_{33}Zr_{11}Ni_6Sn_2Si_1$ pillars: (a) number of bursts per unit engineering strain and (b) yield stress versus pillar diameter.

During compression of tapered pillars, shear bands initiate always at the punch-pillar contact corner and are more frequently generated due to the stress gradient. However, yield strength measurements of tapered and taper-free pillars do not show any noticeable difference in the entire size range as shown in Fig. 4.5b, if an accurate determination of the yield stress has been done with the effective load-bearing diameter of tapered pillars at different stages of deformation. Although the measurement errors are smaller with taper-free pillars, no size effect on yield strength was observed in either of the two pillar

shapes for any composition. The amplitude of the load drops of tapered and taper-free pillars becomes similar as pillars diameter increases (Fig. 4.6).

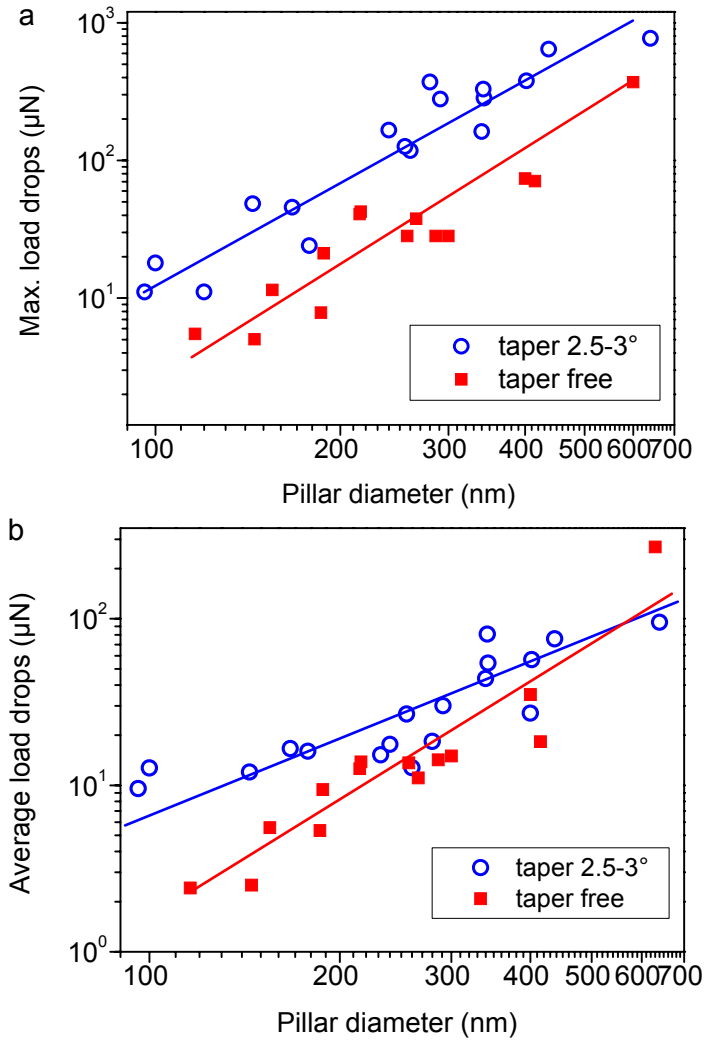

Fig. 4.6. Comparison of mechanical response of tapered and taper-free $Cu_{47}Ti_{33}Zr_{11}Ni_6Sn_2Si_1$ pillars: (a) maximum and (b) average amplitude of load drops versus pillar diameter.

This is attributed to the fact that the deformation of larger pillars is dominated by few discrete shear bands, i.e. independent of pillar shape but rather depending on the pillar size and on the yield strength. The gap between the curves for tapered and taper-free pillars in Fig. 4.6 reflects the tapering effect itself. For tapered pillars the generation of shear bands starts after the indenter touches the pillars. SBs appear from the top and they lead to

nucleation of new SBs during compression. This effect does not appear in taper-free pillars because of homogeneous thickness of pillars that leads to a homogeneous stress distribution. Therefore we do not observe so many shear events for taper-free pillars as for tapered ones (Fig. 4.5a).

4.3.3 Influence of bulk modulus and Poisson's ratio on the size effect

The major reason to study four different compositions $Cu_{47}Ti_{33}Zr_{11}Ni_6Sn_2Si_1$, $Zr_{50}Ti_{16.5}Cu_{15}Ni_{18.5}$, $Zr_{61.8}Cu_{18}Ni_{10.2}Al_{10}$ and $Al_{86}Ni_9Y_5$, was to verify whether the change of bulk modulus and Poisson's ratio may affect the deformation mode and ductility of MGs at the nanoscale.

Table 4.1. The bulk mechanical characteristics of the several MGs with different compositions and their transition thresholds

№	MG Composition	Transition (nm)	(E), GPa	(B), GPa	(μ), GPa	μ/B	(ν)	Ref.
1.	$Zr_{61.8}Cu_{18}Ni_{10.2}Al_{10}$	150	80	108	29	0.269	0.377	current results
2.	$Zr_{50}Ti_{16.5}Cu_{15}Ni_{18.5}$	120	92	118	33.5	0.284	0.37	[1]
3.	$Cu_{47}Ti_{33}Zr_{11}Ni_6Sn_2Si_1$	100	106	126	39	0.310	0.36	[1]
4.	$Al_{86}Ni_9Y_5$	300	57	82	20.5	0.25	0.384	current results
5.	$Au_{49}Ag_{5.5}Pd_{2.3}Cu_{26.9}Si_{16.3}$	1000 (1-343K)	51	89	18	0.2	0.406	[24]
6.	$Zr_{35}Ti_{30}Co_6Be_{29}$	30 - 100 (3-tension)	93.5	106	34.5	0.326	0.353	[25]
7.	$Zr_{57}Cu_{14.4}Ni_{12.6}Al_{10}Nb_5$	200 (2- strip)	87	108	32	0.296	0.365	[26]

Table 4.1 lists the bulk mechanical characteristics for several metallic glasses of different composition, either studied in this work or collected from literature[10, 27] and the transition threshold size from ductile-to-brittle behavior in compression. It is clear that with increasing Poisson's ratio and accordingly decreasing shear modulus over bulk modulus, μ/B ratio, the transition threshold size of MGs becomes is shifted and the ductility is enhanced for larger sizes. To emphasize this dependence, in Fig.4.7 the threshold size is plotted as a function of Poisson's ratio (a) and of μ/B ratio.

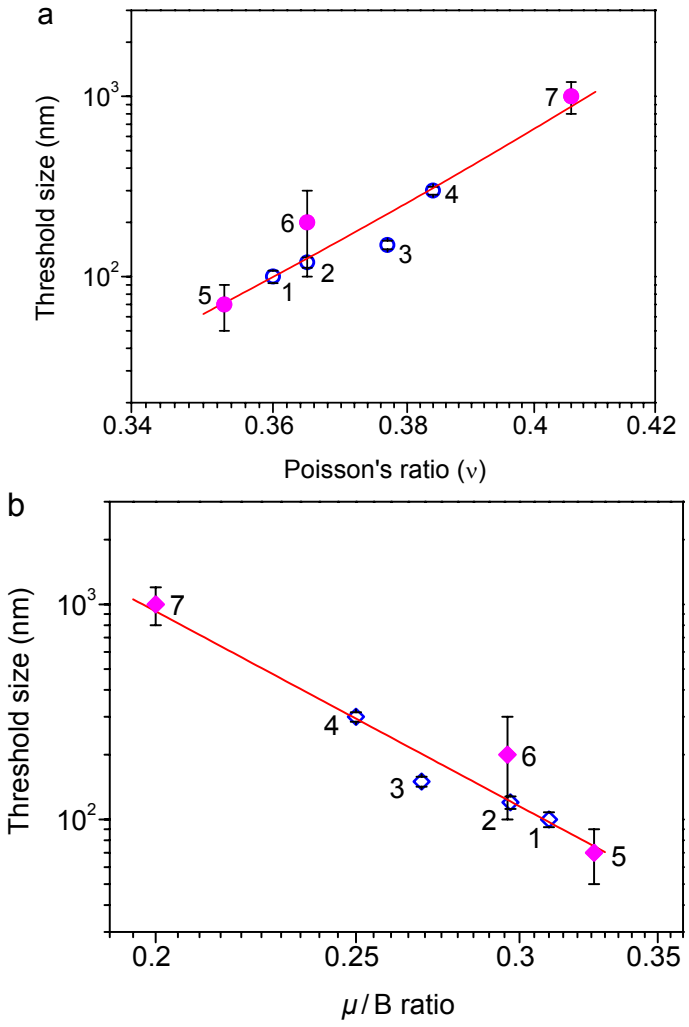

Fig. 4.7. Transition threshold size versus Poisson's ratio (a) and μ/B (b) of different MGs (the data of open symbols are from this work; the data of close symbols 5, 6 and 7 are from Ref. 25, 24 and 10, respectively).

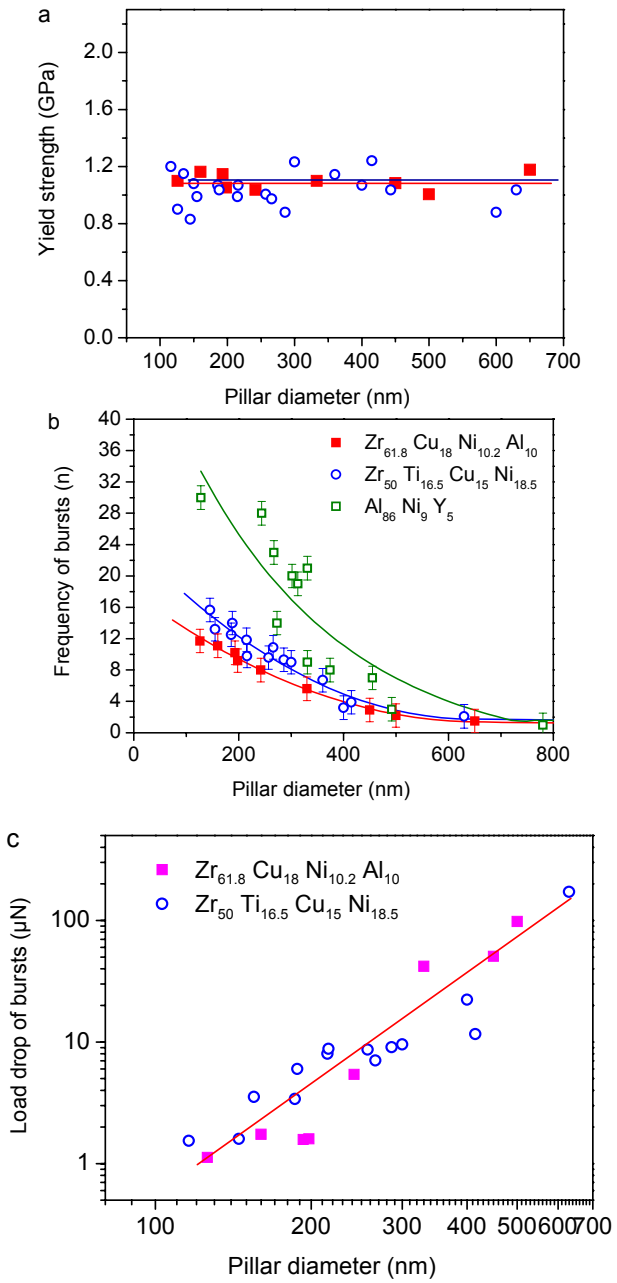

Fig. 4.8. Mechanical characteristics and quantitative analysis of $Zr_{50}Ti_{16.5}Cu_{15}Ni_{18.5}$ and $Zr_{61.8}Cu_{18}Ni_{10.2}Al_{10}$ MGs as a function of pillar diameter: (a) yield stress, (b) frequency and (c) average load drop of bursts vs. pillar diameter of $Zr_{61.8}Cu_{18}Ni_{10.2}Al_{10}$ (close symbols) and $Zr_{50}Ti_{16.5}$ Cu_{15} $Ni_{18.5}$ (open symbols), respectively. Frequency of bursts of $Al_{86}Ni_9Y_5$ indicated with the green color (b).

To investigate the influence of the chemical composition on the nanoscale deformation behavior two MGs of the same Zr-based material but with different added elements were chosen: $Zr_{50}Ti_{16.5}Cu_{15}Ni_{18.5}$ and $Zr_{61.8}Cu_{18}Ni_{10.2}Al_{10}$. Size effects in Al-based systems were investigated ($Al_{86}Ni_9Y_5$) whereas $Zr_{61.8}Cu_{18}Ni_{10.2}Al_{10}$ shows a rather different deformation behavior at the millimeter scale. Different brittleness is observed between these materials[28] and the question is whether this phenomenon is also seen at the nanoscale. The Young's modulus (E) and Vickers hardness (H_v) of $Zr_{50}Ti_{16.5}Cu_{15}Ni_{18.5}$ and $Zr_{61.8}Cu_{18}Ni_{10.2}Al_{10}$ do not differ more than 1% from each other and are approximately 90 GPa and 520 MPa, respectively. However, the major cause of different deformation behavior at the microscale is attributed to their difference in Poisson's ratios, which amounts to 6%.[29] As shown in Fig. 4.8a, the comparison of these two MGs with different composition shows a small difference in size-independent yield stress. However, pillars around 100 nm in diameter of either composition showed ductile behavior during compression, i.e. almost no shear banding.

The frequency of load drops of all three MGs increases rapidly with decreasing pillar diameter (Fig. 4.8b) and points to more frequently-activated shear banding events, whereas the shear displacement carried by individual shear banding events decreases quickly, indicating a suppression of shear band propagation. The number of bursts in more ductile $Al_{86}Ni_9Y_5$ pillars increases rapidly in comparison to the more brittle MGs, testifying to propagation controlled deformation in $Al_{86}Ni_9Y_5$, not nucleation controlled deformation as in the more brittle materials. This behavior is also consistent with the higher Poisson's ratio (see Table 4.1) of $Al_{86}Ni_9Y_5$ compared to Zr-based materials, leading to a more ductile behavior at smaller sizes. The observed load drops at constant displacement rate are triggered by the formation and propagation of multiple shear bands. The amplitude of the load drops for both Zr-based compositions reveals that the shear displacement in thinner pillars proceeds more smoothly, while the stress decreases more steadily. At the smallest diameter of 110 nm, the amplitude of the load drops is very small (<2 μN), whereas the load is still considerably high (~ 10 μN). The ratio between average load drop and maximum load for ~100 nm pillars for both compositions equals 8-10. This ratio decreases down to 1 for larger pillar diameters, which show the propagation of a major shear band to the edge of the pillar (Fig. 4.8a).

The amplitude of load drops of ductile MG is somewhat smaller at larger pillar diameters in comparison with that of brittle MGs. However, with

decreasing pillar diameter this difference becomes less significant. This is caused by changes in the mechanism of the plastic behavior with decreasing pillar diameter. During compression of micrometer sized pillars ductility is due to the distinctive structure of the MGs. The shear transformation zones occur preferentially in softer regions in MGs and evolve into shear bands upon loading. Consequently, numerous shear-band nuclei are formed concurrently in the soft regions. Because the soft regions cannot carry much plastic strain due to shear band multiplication processes, any further deformation has to proceed in hard regions so that a higher plasticity is still attainable on a large scale. With pillar size on the scale of hundred of nanometers, this mechanism is no longer applicable, due to the decrease of the quantity and interaction of more compliant regions.

4.3.4 Discussion

The threshold size for the transition of deformation modes from intermittent shear banding to homogenous flow may be affected by several factors. The physical picture that emerges is the following: In MG pillars of randomly disordered structure, the yield strength is determined by cooperative shear motion of flow defects consisting of atomic clusters, related to the STZs and flow defects.[30, 31, 32] The common activation energy of local inherent states of the flow defects has a broad distribution that may also scale with sample size. The total density of critical flow defects (See paragraph 3.3.1) is determined by the following equation with the distribution function *g(a)*:

$$\rho(a_c) = \int_{a_c}^{\infty} g(a)da = \frac{a_c}{(r-1)} g(a_c) \tag{4.1}$$

It is represented by the shaded area in Fig. 4.9(a). Here, a_c is determined by the Weibull scaling law and scales with the volume of the specimen. When the size approaching zero, *g(a)* goes to infinity and one expects that the actual density distribution of flow defects smaller than individual STZs may deviate from the simple function form of power-law decay. This goes with a trend represented by the dashed curve in Fig. 4.9(a). However, such a deviation may not influence the analysis, since defects smaller than the critical value a_c do not remarkably influence the failure phenomenon.

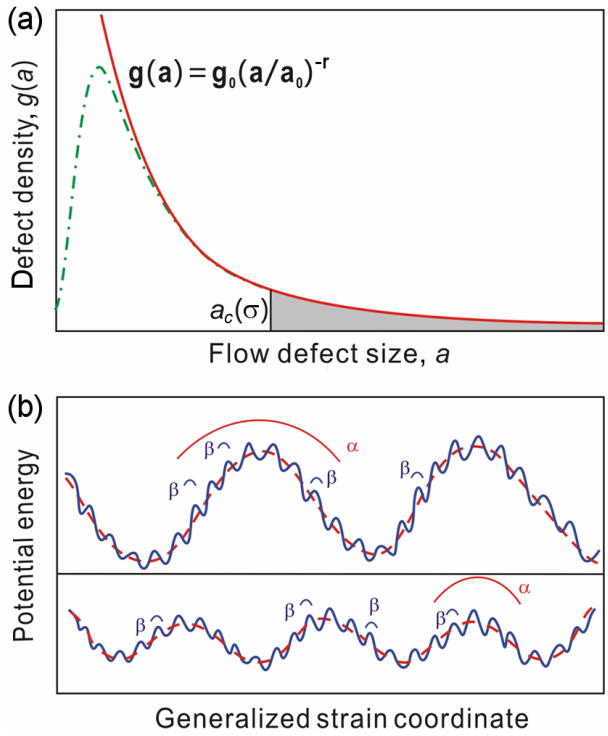

Fig.4. 9. Conjectured size distribution of microscopic flow defects associated with elementary transitions in potential energy landscape (PEL) influenced by system size: (a) plot of function g(a) defining flow defect density versus size of the defects, (b) PELs of a relatively large (top) and small (bottom) system.

Then, the total volume fraction of critical flow defects is expressed as

$$f(a_c) = \int_{a_c}^{\infty} ca^k g(a)da = \frac{ca^{k+1}}{r-(k+1)} g(a_c), \tag{4.2}$$

c and k being shape related factors, assuming ellipsoidal shape of the flow defects that is normally assumed for STZs [47,49], k has a value between 3 and 2 that are values for spheres and discs, respectively. Again, assuming that $r = m/2+1$ is large compared to (k + 1) (in Weibull materials, m is ranging from 10-100 for metals and ceramics, and 20-70 for MGs), utilizing Eq. 4.2 and keeping in mind the constant aspect ratio for all the pillars, one obtains approximately:

$$f(a_c) \propto a_c^{-r} \propto V^{-m^2/2} = D^{-3m^2/2}, \tag{4.3}$$

where D is diameter. This scaling behavior implies that despite the larger critical flow defect size a_c that can be developed in a bigger specimen, the

total volume fraction of the flow defects is rather low. This is consistent with the experimental observation that in larger pillars deformation is localized in local SBs, which account for a small fraction of the total volume. In a smaller volume large flow defects have less chance to be developed and smaller local flow defects are dominating the deformation. This is confirmed by the smoother stress evolution with vanishing stress-drops and less-observable local shear in the structure evolution at smaller size regimes. The smaller flow defects will have a higher density. These smaller local transitions however account for a larger volume fraction of the specimen and are well distributed, hence less localized (Eq.(4.3)). In Eqs. 4.1-4.3 flow defects are proportional to the material related constant (m) and to the diameter of the sample (D). The dependence on applied load is also involved but to a lesser extent because the current experiments were done in displacement-controlled mode.

It should be pointed out that in bulk specimens the scaling of flaw sizes with specimen volume may statistically lead to a size-dependent fracture stress based on Griffith theory within the framework of continuum mechanics and the weakest link assumption,[7,10,53] where the flaws are generally treated as cracks. However, the flow defects in the small size MGs are approaching the nanoscale where Griffith theory may not hold. In addition, these flow defects are local (shear) transformations without opening and dissimilar to cracks. The strength of the flow defect is directly controlled by the nucleation stress of STZs equal to the yield stress, rather than controlled by its size. Therefore, a significant size-dependent strength based on Weibull statistics is not expected (see also.[33]).

It is helpful to understand the microscopic processes underlying the size effects also from a perspective of the potential energy landscape, suggesting that the transient local events can be related to discontinuous transitions and relaxations to different energy minima in the potential energy landscape.[34] Recently, Johnson and Samwer et al[49, 35, 36] have extended Ali Argon's concept of STZ and merged it into the potential energy landscape perspective. These authors proposed a cooperative shear model to understand the deformation mechanisms and rheological properties of MGs. According to the cooperative shear model, activation of isolated STZs locally confined within elastic matrix could be associated with the faster β relaxation which is reversible, while the percolation of these transitions leads an irreversible collapse of the confining matrix and breakdown of elasticity, which are associated with the slower α process. The β transitions are identified in potential energy landscape as stochastically activated hopping events across ''subbasins'' within an inherent

‘‘megabasin’’ shown in Fig. 4.9(b), and the α transitions as (interbasin) hopping events extending across different landscape megabasins. Consequently, the effect of MG sample size on its mechanical response could be correlated to inherent relaxation processes and properties of the potential energy landscape. From the potential energy landscape perspective, in a smaller volume a large number of hopping events occur with a high frequency each releasing a small amount of energy, and this results in a relatively smooth transition in the potential energy landscape, as shown in Fig. 4.9b. In a more bulky specimen, excessive energy accumulation may lead to unbalanced relaxation events. When the whole system is unable to find any basin point to rest in the potential energy landscape a shear catastrophe occurs.

The experimental observations in this work clearly reveal that the irreversible alpha events associated with the load drops in Figs. 3b and 4b are size-dependent. With decreasing the size of the pillars, the amplitude of alpha events decreases but their frequency increases, since both are related to the size and density of isolated STZs. In contrast, the amplitude of beta transitions is independent of sample size and determined only by their local relaxation character. When MG samples are reduced to sizes of tens of nanometers, the alpha hopping events merge with the beta transitions, leading to a smooth plastic flow in deformation. Recent experimental measurement utilizing mechanical loss spectroscopy[37] has shown that by reducing the thickness of an amorphous thin PdCuSi film below 30 nm the loss of the secondary relaxation is vanishing, which was considered as merging of the primary relaxation and the secondary relaxation due to size effects and associated to less elastic confinement at the surface of the film. Merging of alpha and beta transitions, as well as a larger volume fraction involved in deformation, have similarity in homogeneous flow of MGs close to glass-transition temperature Tg.[38]

As we have seen in the previous section, upon decreasing the size of pillars, the amplitude of the strain burst decreases and their frequency increases, since both are related to the size and density of isolated STZs. This is consistent with the finding that the size above of which catastrophic and brittle failure occurs is materials-dependent. A material like $Al_{86}Ni_9Y_5$ having a lower μ/B ratio (or larger Poisson’s ratio) can homogeneously deform to larger diameters before brittle failure occurs than e.g. $Zr_{35}Ti_{30}Co_6Be_{29}$ (see Table 4.1). Although the exact nature of the local atomic motion when deforming metallic glasses is not fully resolved it is reasonable to envision that sites of low μ/B will accommodate more readily local shear. Based on Table 1 we therefore expect a larger and more readily accommodated STZ in

Al-based $Al_{86}Ni_9Y_5$ than in $Zr_{35}Ti_{30}Co_6Be_{29}$ and Cu-based systems. While the initiation of shear bands is controlled by shear stress, shear band propagation may be controlled by stored elastic energy resolving into a shear band. When a strain burst occurs the energy released is approximately (see our previous paper about details of a micromechanical description):

$$\Gamma = \frac{1}{4}\sqrt{2}(\sigma_i^2 - \sigma_{i+1}^2)\frac{D}{E} \tag{4.4}$$

where σ_i and σ_{i+1} are the stresses before and after the ith burst, D the diameter and E the Young's modulus. For a shear band that propagates through the entire pillar on a plane 45^o with respect to the loading axis follows:

$$D = 2\sqrt{2}\xi\frac{E\Gamma}{\sigma^2}. \tag{4.5}$$

Here ξ reflects the ratio of the shear transformation zone with respect to the diameter. If $\xi = 1$ catastrophic failure occurs and the shear band crosses the entire pillar. For the systems investigated the ratio between yield stress and *E* modulus is approximately constant (Table 1). The larger $\xi\Gamma/\sigma$, the larger diameter will be found above of which catastrophic failure occurs in a brittle manner. This is consistent with our findings that e.g. $\sigma_{Al} = 0.6\sigma_{Cu}$ and $\Gamma_{Al-base} = 1.8\Gamma_{Cu-base}$. From these arguments it is predicted that the maximum size for ductility of $Al_{86}Ni_9Y_5$ is about 3 times the critical size of Cu based systems as in agreement with mechanical testing.

Indeed, we can also recast our findings in size effect on SB propagation speed,[39] i.e. the lower the speed, the less "brittle" the specimen becomes. In our previous work we have investigated the propagation velocity more explicitly. It was presented as an average velocity (because of the jerky character) and calculated from the amplitude and frequency of displacement bursts and/or lord drops. Also in this work, basically, we are measuring the amplitudes and frequencies, and not directly the velocities. As far as the topic of velocity in MG is concerned an interesting contribution was recently reported.[40,41] Using a piezoelectric load cell data were acquired at rates of 10 kHz recording for individual load drops a time resolution of 300 μs. Interestingly, the shear band velocities in these studies but on much bigger samples (3mm in diameter) than those studied here , were found to exhibit a

pronounced temperature dependence covering nearly two orders of magnitude.

Finally, we would like to discuss the possibility that extrinsic factors influence the size-dependent deformation behavior discussed so far. The first item to be considered is ratio between the stiffness of instrument frame and the specimen. Han *et al.* recently demonstrated that higher instrument stiffness and smaller specimen size restrain catastrophic failure of MGs along a single dominant shear band.[42] The observation that the amplitude of the force drops decreases with decreasing pillar size, and at the same time the frequency increases could be related to the reduced stored elastic energy in the sample-machine assembly as similar observations were made on the macro-scale.[42,43] While a specimen fails due to the propagation of a dominant shear band when tested on a compliant frame, more stable plastic flow from multiple defects can be observed with a stiffer test frame under the same loading conditions. The physical argument of this extrinsic factor may be described as the total elastic energy stored that is released to drive the propagation of a dominant shear band: the larger the stored elastic energy, the faster the propagation and the more localized failure is. The extrinsic factor has an effect on the transition ductile-to-brittle threshold in different MG systems, because the same picoindenter was used and selection of MGs covered a wide range of stiffness

Another extrinsic factor is the geometry of pillars, namely tapering. For small scale pillars this has been discussed in detail by Schuster et al.[9], by Flores and collaborators[44] and in our review paper. Macroscopic samples without taper also exhibit shear initiation at the corner of the sample-to-anvil interface. Hence, tapering seems not to be the worst factor if size-dependent arguments are excluded. In principle if the taper angle remains roughly the same, tapering is a geometry effect that is self similar across sizes. Our measurements demonstrate that although the frequency and amplitude of bursts (or load drops) may differ due to tapering, this does not change the physical picture of the transition between deformation modes from intermittent shear banding to homogenous flow upon decreasing pillar size, nor the size-independent yield strength. Finally, the preparation treatments of BMG samples should be more or less identical in a comparative study. Molecular dynamics simulations suggest that extrinsic factors such as surface notches and cracks may introduce significantly changes with respect to the intrinsic mechanical properties of amorphous metals.[45]

4.4 Conclusions

The mechanical performance of nano-sized systems (pillars) of metallic glasses with diameters ranging from 90 to 600 nm were tested in-situ in a TEM. For this study MG pillars of different alloy systems and compositions were selected: one Cu-based alloy, two Zr-based alloys and one Al-based alloy, i.e. $Cu_{47}Ti_{33}Zr_{11}Ni_6Sn_2Si_1$, $Zr_{50}Ti_{16.5}Cu_{15}Ni_{18.5}$, $Zr_{61.8}Cu_{18}Ni_{10.2}Al_{10}$ and $Al_{86}Ni_9Y_5$. The major consideration for this composition variation was to investigate how the change of bulk modulus and Poisson's ratio may affect the deformation mode and ductility of MGs at the nanoscale.

From the in-situ experiments it can be concluded that all materials exhibit size effects upon deformation. In situ TEM shows that upon decreasing the size of the pillars, smaller local shear processes (flow defects) become critical, leading to homogeneous deformation. The deformation is still intermittent and may develop to shear bands at larger size but becomes banding-free when the system approaches smaller scales. At larger scale each pillar showed predominantly inhomogeneous and intermittent plastic flow, characterized by shear banding events. However, taper-free pillars with smaller diameters exhibited ductile behavior during compression almost without shear banding.

Different compositions, such as Cu-based, Zr-based and Al-based, results in different values for the transition threshold from ductile-to-brittle behavior upon increasing size. Higher values of the Poisson's ratio, and consequently lower values of the μ/B ratio lead to more ductile behavior. The lower μ/B, the larger the critical pillar diameter above which more brittle behavior occurs. The $Al_{86}Ni_9Y_5$ taper-free metallic glass showed the highest transition threshold for brittle behavior, namely for pillar diameters above 300 nm.

References

1. A.L. Greer, E. Ma, Materials Researsh Society bulletin 32, 611 (2007).
2. C.A. Schuh, T.C, Hufnagel, U. Ramamurty, Acta Materialia 55, 4067 (2007).
3. A.S. Argon, Acta Metalllugrica 27, 47 (1979).
4. M.L.Falk, J.S. Langer, Physical Review E 57 1998;57:7192.
5. W.E. Johnson, K Samwer, Physical Review Letters 95, 195501 (2005).
6. J.R. Greer, J.Th.M De Hosson, Progress Materials Science 56, 654 (2011).
7. S. Xie, E.P. George, Intermetallics 16, 485 (2008).
8. C.A. Volkert, A. Donohue, F. Spaepen, Journal of Applied Physics 103, 083539 (2008).

9. B.E. Schuster, Q. Wei, T.C. Hufnagel, K.T. Ramesh, Acta Materialia 56,5091 (2008).
10. D.C. Jang, J.R. Greer JR, Nature Materials 9, 215 (2010).
11. O.V. Kuzmin, Y.T. Pei, J.Th.M. De Hosson, Applied Physics Letters 98, 233104 (2011).
12. D.C. Jang, C.T. Gross, J.R. Greer, International Journal of Plasticity 27, 858 (2011).
13. J.Th.M. De Hosson, W.A. Soer, A.M. Minor, Z. Shan, E. Stach, S.A.S. Asif, O.L. Warren, Journal of Materials Science 41, 7704 (2006)
14. J. Rajagopalan, J.H. Han, M.T.A. Saif, Science 315, 1831(2007).
15. C.Q. Chen, Y.T. Pei, J.Th.M. De Hosson. Acta Materialia 58, 189 (2010).
16. J.J. Lewandowski, W.H. Wang , A.L. Greer, Philosophical Magazine Letters 85, 77 (2005).
17. C.Q. Chen, Y.T. Pei, J.Th.M. De Hosson. Philosophical Magazine Letters 89, 633 (2009).
18. W.A. Soer, J.Th.M. De Hosson, A.M. Minor, Z.W. Shan, S.A.S. Asif, O.L. Warren. Applied Physics Letters 90,181924 (2007).
19. A.M. Minor, S.A.S. Asif, Z.W. Shan, E.A. Stach, E. Cyrankowski, T.J. Wyrobek, O.L. Warren, Nature Materials 5, 697 (2006).
20. Z.W. Shan, R.K. Mishra, S.A.S. Asif, O.L. Warren, A.M. Minor, Nature Materials 7, 115 (2007).
21. T. Mukai, T.G. Nieh, Y. Kawamura, A. Inoue, K. Higashi, Intermetallics 83, 180201(R)10 1071(2002).
22. C.Q. Chen, Y.T. Pei, O. Kuzmin, Z.F. Zhang, E. Ma, J.Th.M. De Hosson. Physical Review B 83, 180201 (2011).
23. A Dubach, R Raghavan, J.F. Loeffler, J. Michler, U. Ramamurty, Scripta Materialia 60, 567 (2009).
24. S. X. Song, Y. H. Lai, J. C. Huang, and T. G. Nieh Applied Physics. Letters 94, 061911 (2009).
25. J. Dongchan and J. R. Greer, Nature Materials 9, 215-219 (2010).
26. A. R. Yavari, K. Georgarakis, W. J. Botta, A. Inoue, and G. Vaughan, Physical Review B 82, 172202 (2010).
27. S.X. Song, J.S.C. Jang, J.C. Huang, T.G. Nieh, Intermetallics 18, 702 (2010).
28. Y.H. Liu, G. Wang, R.J. Wang, D.Q. Zhao, M.X. Pan, W.H. Wang. Science 315, 1385 (2007).
29. T. Zhang, A. Inoue, Materials Transactions JIM 39,1230 (1998)
30. D. Srolovitz, V. Vitek, T. Egami, Acta Metallurgica 31, 335 (1983)
31. D. Rodney, C. Schuh, Physical Review Letters 102, 235503 (2009).
32. Y Wu, GL Chen, XD Hui, CT Liu, Y Lin, XC Shang, ZP Lu, Journal of Applied Physics 106, 083512 (2009).
33. D.C. Jang, C.T. Gross, J.R. Greer, International Journal of Plasticity 27, 858 (2011).
34. F.H. Stillinger, Science 267, 1935 (1995).
35. J.S. Harmon, M.D. Demetriou, W.L. Johnson, K. Samwer, Physical Review Letters 99, 135502 (2007).
36. M.D. Demetriou, J.S. Harmon, M. Tao, G. Duan, K. Samwer, W.L. Johnson, Physical Review Letters 97, 065502 (2006).
37. D Bedorf, K Samwer, Journal of Non-Crystalline Solids 356,340 (2010).

38. J. Rault, Journal of Non-Crystalline Solids 271, 177 (2000).
39. M. Zhao, M. Li, Y. Zheng, Philosophical Magazine Letters 91, 705 (2011).
40. D. Klaumünzer, R. Maass, F.H. Dalla Torre, J.F. Löffler. Applied Physics Letters 96, 061901 (2010).
41. R. Maaß, D. Klaumünzer, J.F. Lö□er, Acta Materialia 59, 3205 (2011).
42. Z Han, W.F. Wu, Y. Li, Y.J. Wei, H.J. Gao, Acta Materialia 57, 1367 (2009).
43. Y.Q, Cheng, E. Ma, Acta Materialia 59, 1800 (2008).
44. A. Bharathula, S.W. Lee, W.J.Wright, K.M. Flores, Acta Materialia 58, 5789 (2010).
45. Q.K. Li, M. Li, Intermetallics 14,1005 (2006).

Chapter 5

Ductile Al-based metallic glass

This chapter concentrates on in situ compression tests in transmission electron microscopy (TEM) of taper-free nano-sized pillars of $Al_{86}Ni_9Y_5$ metallic glass (MG) with diameters ranging between 110 and 900 nm. A critical size was found, below of which the deformation mode changes from intermittent shear banding to homogenous flow. In comparison with Cu- and Zr-based MGs, the threshold size for the transition from brittle to ductile behavior shifts from a diameter of 100 nm to 300 nm in $Al_{86}Ni_9Y_5$. Up to now plasticity was not found before in metallic glasses with these dimensions. Another parameter such as the aspect ratio is also discussed. In particular the aspect ratio plays a significant role regarding the stability, and determines bending versus compression in the experiments and, as a consequence, has a large influence on the final ductility. The ductility of $Al_{86}Ni_9Y_5$ MG at compression-bending mode opens interesting possibilities for future applications. Interestingly, the work reveals softening and toughening effects during cyclic deformation of metallic glasses and a physical model will be presented.

5.1 Introduction

The main drawback of metallic glasses that hamper applications is their brittleness at room temperature caused by strain localization in narrow areas called shear bands (SBs). Various attempts to enhance the deformability of MGs were focused on the development of alloy systems and compositions so as to enhance a uniform distribution of SBs.[1] A unique strains as high as 70% in compression was reported as well as an enhancement of the plasticity limit in tension, either in thin metallic glass foils even at room temperature.[2,3] Several toughening mechanisms were considered in the explanation of the experimental observations, including a high Poisson's ratio or μ/B ratio, spinodal phase separation[4], nanometer-scale heterogeneities[5],

nanocrystallization within shear bands [6], extreme amounts of the free volume content[7] and sluggish atomic movement kinetics.[8]

The influence of sample size on compressive deformation response has been recently studied for several amorphous alloy systems.[9,10,11,12,13,14,15] For a recent review reference is made to.[16] It was found that the yield strength is independent of sample size ranging from tens of nanometers to one micrometer but the plasticity increases as sample sizes decreases. It was observed that there exists a critical energy density above which catastrophic fracture would occur. This critical energy density depends on the composition of MG but it is independent of sample size.

Here we focus on Al-based MGs since in comparison with conventional crystalline Al alloys, Al-based MGs exhibit much higher yield strength without loss of ductility and corrosion resistance.[17] Despite studies on mm and sub-mm scale, size effects on nanometer scale of these MGs have not been investigated before. The mechanical response of $Al_{86}Y_9Ni_6$ MG is scrutinized in the present work with in-situ compression test in transmission electron microscopy (TEM) on taper-free pillars of sizes down to 100 nm. We show strong size effects with the achievement of excellent mechanical properties.

It is also well known that the ductility of MGs at the large scale depends strongly on the sample geometry and, as a consequence, on the aspect ratio[18] ρ (height to diameter ratio), e.g. at mm-scale buckling occurs when $\rho > 5$, shear banding $2.5<\rho<5$, and barreling when $\rho < 2.5$.

In particular, here we present new results on the aspect ratio dependences on two accounts that have not been observed. First, research on the effect of the aspect ratio at smaller length-scales, the focus point of this thesis, is rather scarce in literature. Second, this chapter governs effects of aspect ratio on the mechanical behavior of an Al-based MG over a very wider range, i.e. 3 to 12, in order to investigate the yield strength dependence, plasticity, as well as the corresponding shear deformation and brittle fracture mechanisms. As far as the diameter is concerned, our choice is based on our findings, i.e. pillars around 300 nm diameter show the transition from brittle to ductile behaviour (see section 5.3.1.) and therefore this diameter is assumed to exhibit a higher sensitivity on the aspect ratio.

Despite the absence of a crystallographic lattice structure these materials exhibit failure under fatigue at room temperature, with an endurance limit as low as 4% of the yield strength.[19] A question to be addressed is: what happens during cyclic deformation when down-sizing the specimen to a couple of hundred nanometers? Recently, several studies have reported on the cyclic

compression of crystalline nanopillars. Milne et al. have demonstrated that compressive and cyclic loads can be applied to individual nanostructures, enabling the observation of nanoscale deformation and fatigue of Al crystalline pillars of 350 nm diameter.[20] In crystalline Al nanopillars 15% of the stress reduction was explained by the formation and re-arrangement of grains. However this effect is not expected for Al-base MG pillars, since there are no grain boundaries or dislocations present.

In the final section we show an exciting phenomenon of nano-sized MG pillars under cyclic loading revealing that deformation contributes to advanced MGs ductility. The mechanical response of in-situ TEM compression tests on taper-free MG pillars of diameter down to 150 nm at cyclic deformation mode will be also presented and suggestions for a physical description are made.

5.2 Experimental background

MG Al-based alloy with a composition of $Al_{86}Ni_9Y_5$ was selected. MG alloy was prepared by melt spinning. Ribbons of 0.3 mm in thickness were mechanically polished down to a wedge shape of around 3 μm thickness suitable for further focused ion beam (FIB) milling. Taper-free nanopillars were cut by using an in-house developed FIB milling technique. A different set of rectangular taper-free nanopillars with diameters ranging from 110 to 900 nm was successfully fabricated for different experiments including compression tests, aspect ratio investigations and cyclic experiments by means of a dual beam FIB/SEM microscope (Lyra, Tescan, CZ). First, a series of rectangular microsized beams were milled on the microwedge. Then, out of these beams, nanopillars were fabricated step by step with decreasing FIB current at different milling stages. First, a series of microsized beams were milled on the microwedge at 10 degrees tilt angle of the stage with respect to the ion beam at high FIB current (~10 nA). Then, nanopillars were fabricated from these beams step-by-step with decreasing FIB current at different milling stages down to 1 pA.

The aspect ratios were varying from 2.5 to 12. The accuracy of measuring pillar diameter was equal to 3%. The final shape of the pillars has been achieved to be fully taper-free. The aspect ratio of the pillars for typical compression and cyclic experiments was maintained in the range of 2.5 to 3.5. For the investigation of the influence of aspect ratio the diameter of the pillars was kept constant to 300±20 nm. The amorphousness of the Al ribbons was

examined by X-ray diffraction and confirmed by high-resolution TEM observations on the nanopillars.

The cyclic experiments were performed in such a way that unloading was followed after each loading cycle when reaching the corresponding yield stress and subsequently one stress drop (due to shear band propagation) was registered. To ensure reproducibility of the cyclic experiments, several samples, order of 3, were investigated.

In-situ TEM compression experiments were performed using a Hysitron picoindenter TEM holder (Hysitron Inc., Minneapolis, MN, USA) equipped on JEOL 2010F TEM, with a diamond flat punch of 1.5 μm in diameter. It is integrated with a miniature capacitive load–displacement transducer permitting high resolution load and displacement measurements (resolution of ~0.3 μN in load, ~1 nm in displacement). In addition, a rapid instrument response and data acquisition rate (the controller operates in a continuous loop and samples data at 20 kHz) allows discrete flow events to be well-resolved.

The experiments are run in displacement rate control mode, which shows a great sensitivity. The displacement and/or load rate are programmed in such a way that a nominal strain rate of ~ 10^{-2} s^{-1} is applied. Together with the high data acquisition rate, this all makes it possible to evaluate the development of a single SB event, which is found to be strongly size dependent.

5.3 Results and discussion

5.3.1 Size effects and ductility of $Al_{86}NI_9Y_5$

In section 4.3.3 we showed that, in accordance with the work of Lindsay Greer and collaborators,[21] the ratio between shear modulus and bulk modulus (μ/B) is a major factor that determines the mechanical performance of MGs under compression.[22] According to these considerations, the selection of MG composition elements is targeted for lower μ/B and higher Poisson's ratios to attain a higher ductility of small-sized samples. Therefore, the $Al_{86}Ni_9Y_5$ MG with a relatively low shear modulus-bulk modulus ratio μ/B ratio was chosen for further examination of size effects. To represent the transition threshold from brittle to ductile behavior in this particular MG, three pillars of diameters 490 nm, 450 nm and 315 nm were compressed in situ, respectively, as shown in Figs. 5.1-5.3.

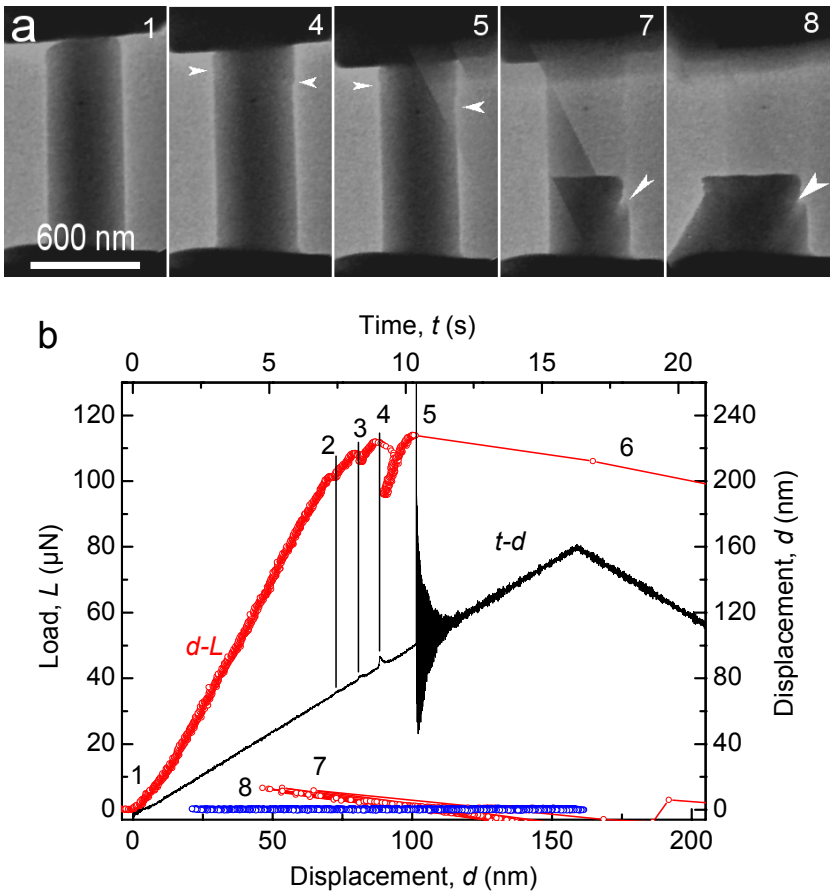

Fig. 5.1. (a) Video frames recording the deformation of a ø 490 nm $Al_{86}Ni_9Y_5$ MG taper-free pillar compressed under displacement-control mode. Grabbed video frames (1-8) show the deformation structures before, during and after compression (white filled arrows indicate the shears). (b) Load-displacement and time-displacement curves with the vertical black lines (2-5) indicating shear events. Line 5 corresponds to the time and displacement when pillar has broken. The numbers on the d-L curve correspond to the numbers of video frames.

The relatively large pillar (ø490 nm, Fig. 5.1) exhibited two large shear bands at the early stage (around 5% strain) after yielding and the final banding led to catastrophic break that exceeded the recording speed of the camera. The amplitude of load drop in the successive shear events increased from 3 to 15 μN.

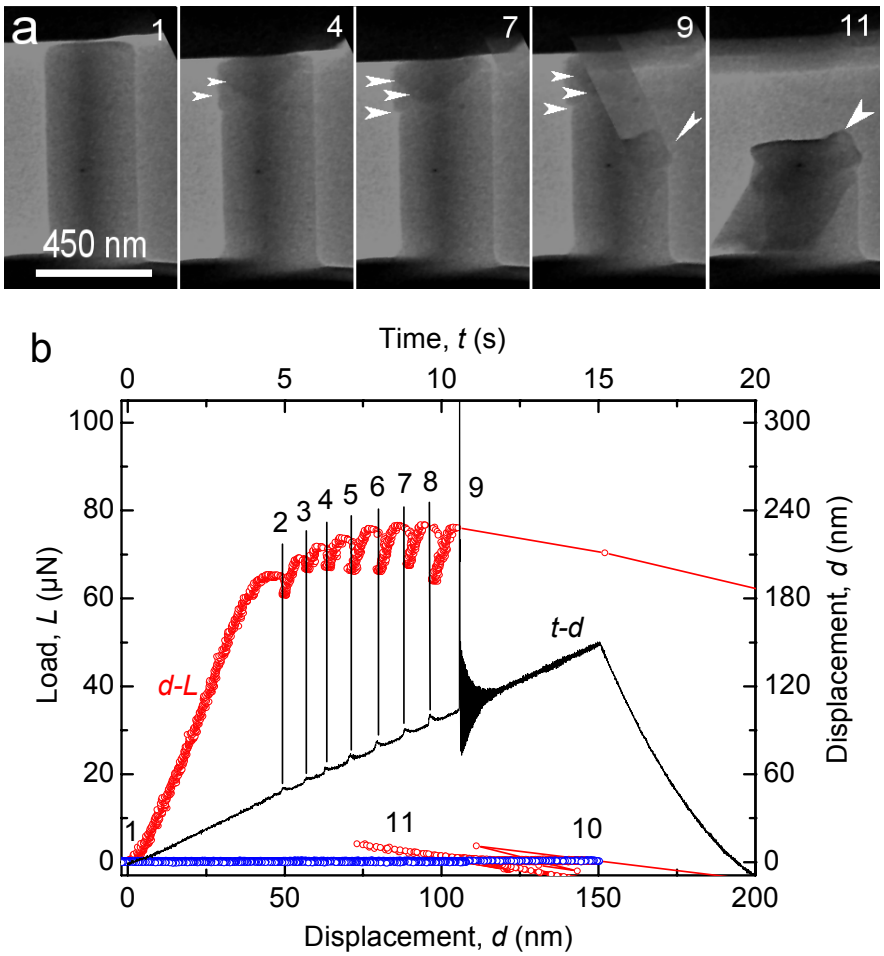

Fig. 5.2. (a) Video frames recording the deformation of a ø450 nm and length 1420 nm $Al_{86}Ni_9Y_5$ MG taper-free pillar compressed under displacement-control mode. Grabbed video frames (1-11) show the deformation structures before, during and after compression (arrows indicate the shears). (b) Load-displacement and time-displacement curves with the vertical black lines (2-8) indicating shear events. Line 9 corresponds to the time and displacement when pillar has broken. The numbers on d-L curve correspond to the numbers of video frames.

As the pillar diameter became smaller (ø450 nm, Fig. 5.2) more shear events occurred after yielding and the associated load drops increased gradually from 2 to 13 μN yet with smaller intermediate bursts of displacement in between, attaining a higher engineering strain (10%) in comparison with 7% of the thicker pillar (ø490 nm). With further reducing the pillar size to around 300 nm (Fig. 5.3), the number of shear events significantly increased. The deformation of the pillar began in the same way

of shear banding as that of the larger pillars, but after several small shear events the pillar started to flow homogeneously and did not break at an engineering strain of 26%. This was considered as the transition point from brittle to ductile deformation behavior of $Al_{86}Ni_9Y_5$ MG pillars, which is around 300 nm in diameter.

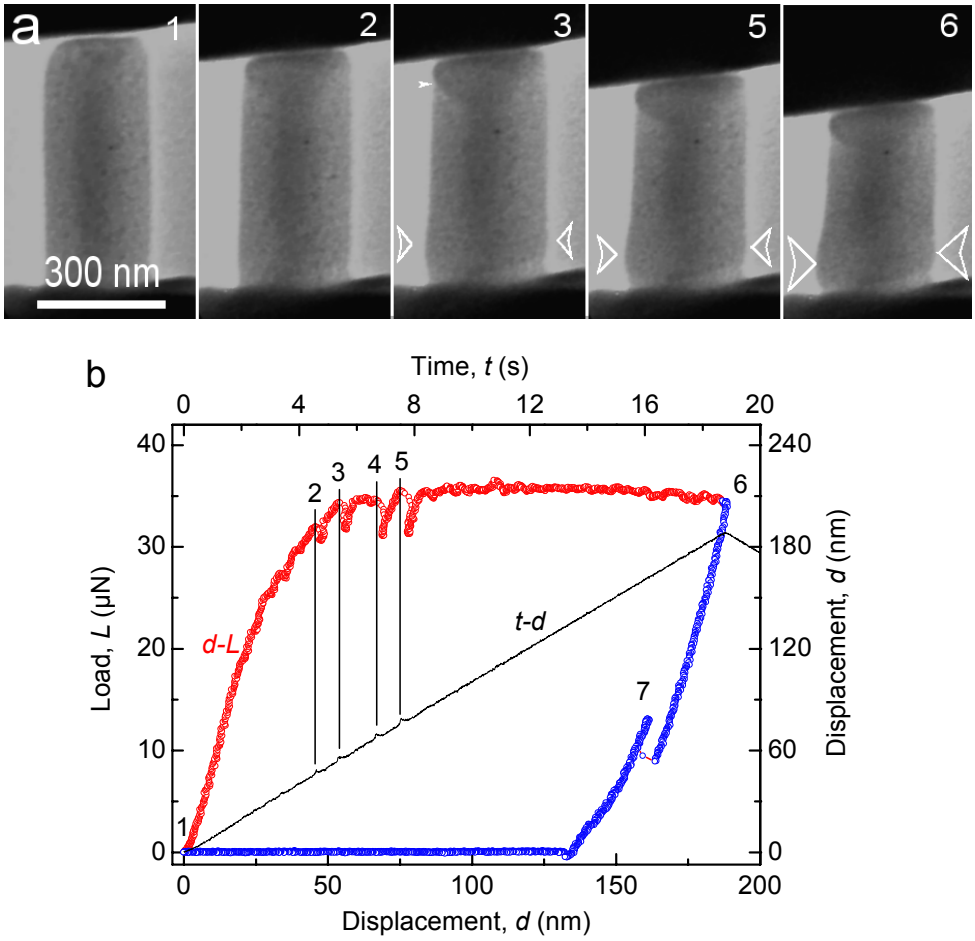

Fig. 5.3. (a) Video frames recording the deformation of a ø 315 nm Al_{86} Ni_9 Y_5 MG of taper-free pillar compressed under displacement-control mode. Grabbed video frames (1-6) show the deformation structures before, during and after compression (white empty arrows indicate the bulging areas). (b) Load-displacement and time-displacement curves with the vertical black lines (2-5) indicating small shear events. Shear activities occur during the whole deformation process after yielding. The numbers on the d-L curve correspond to the numbers of video frames.

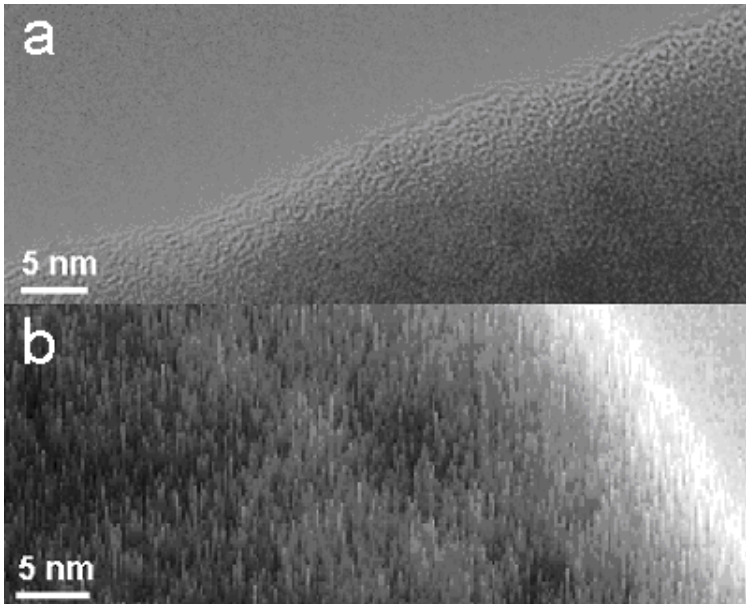
a
5 nm
b
5 nm

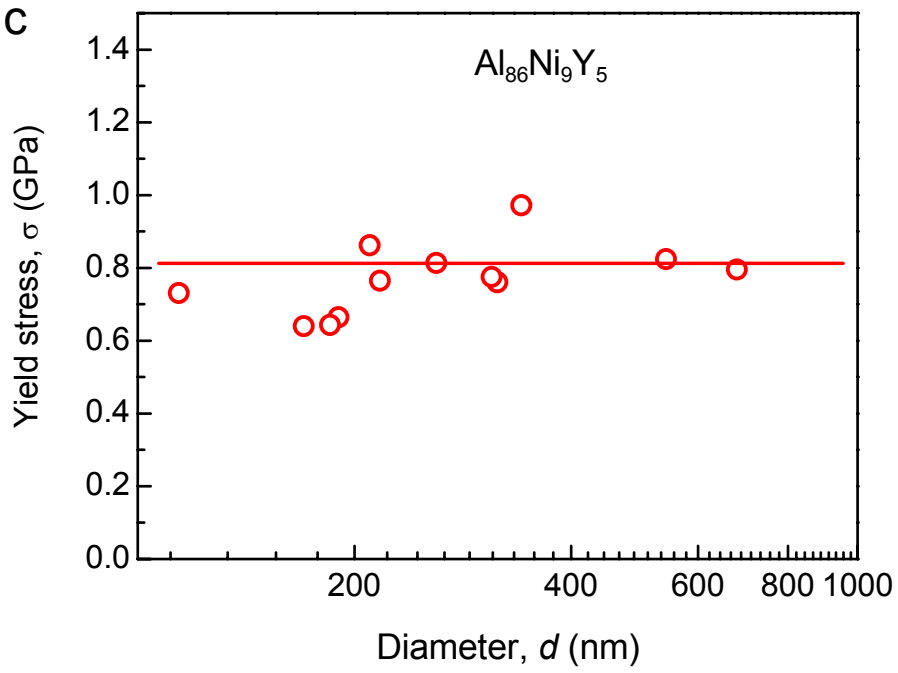
c
$Al_{86}Ni_9Y_5$
Yield stress, σ (GPa)
1.4
1.2
1.0
0.8
0.6
0.4
0.2
0.0
200
400
600
800
1000
Diameter, *d* (nm)

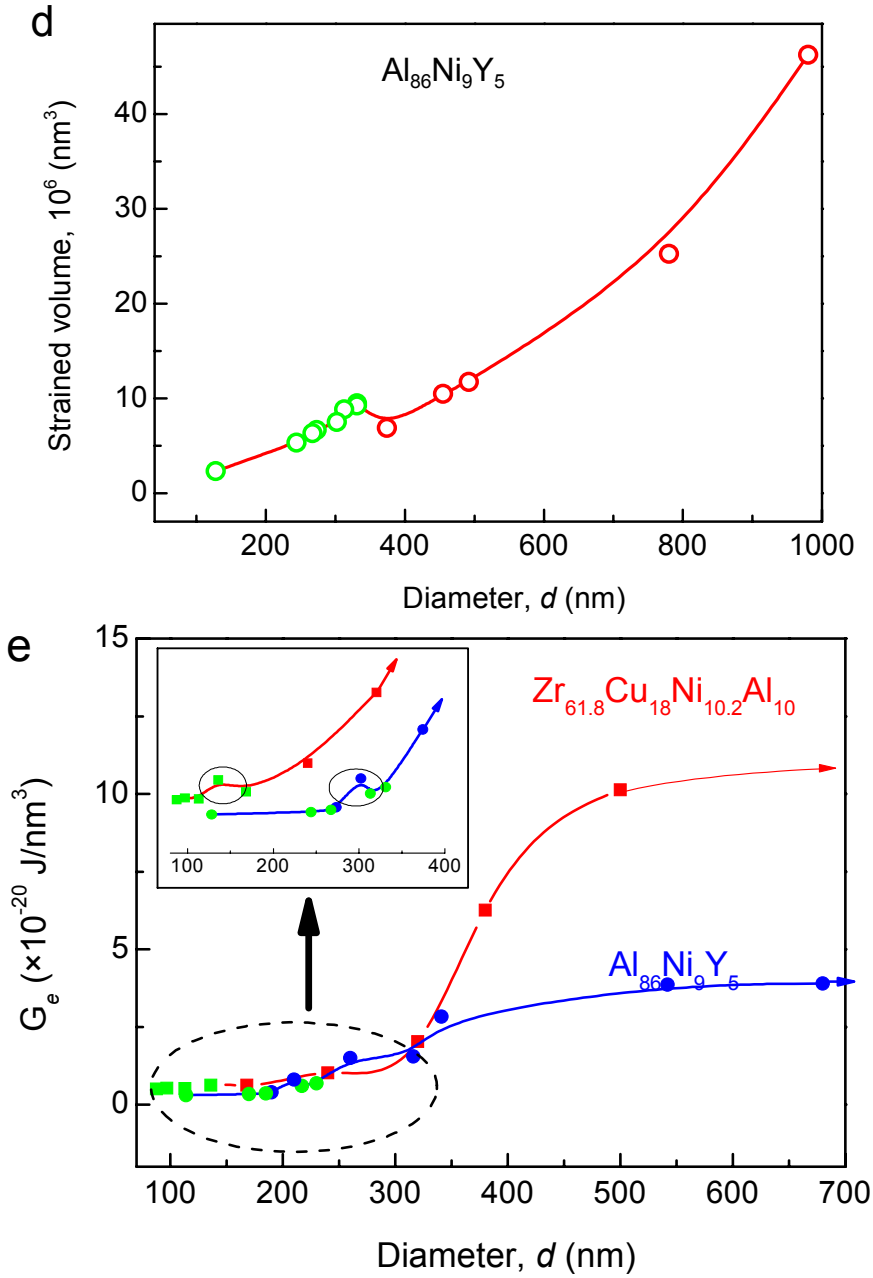

Fig. 5.4. (a) HRTEM picture of ø300 nm $Al_{86}Ni_9Y_5$ MG pillar after compression (bulging area, wavy-like structure); (b) surface topography of HRTEM picture (side view of z-component); (c) yield strength of $Al_{86}Ni_9Y_5$ MG independent of pillar diameter; (d) Strained volume versus pillar diameter of $Al_{86}Ni_9Y_5$ MG; (e) Critical elastic energy per elastic strained volume versus pillar diameter of $Al_{86}Ni_9Y_5$ and $Zr_{61.8}Cu_{18}Ni_{10.2}Al_{10}$ MG. Green dots indicate the samples without fracture.

The transition point from brittle to ductile behavior is related to the alloying system and composition of MGs. An Al-based MG with lower μ/B ratio (or larger Poisson's ratio) can homogeneously deform to larger sample sizes than e.g. Zr-based MGs before brittle failure occurs, although the exact nature of the local atomic motion in deforming metallic glasses is not yet fully resolved.

The yield stress of the $Al_{86}Ni_9Y_5$ MG was defined as the load *L* applied onto the top surface area of the pillars. The strength of the full range of pillars with diameters from 110 nm to 900 nm was calculated and plotted versus pillar diameters as shown in Fig. 5.4c. The strength of pillars with different diameters varies between 650 MPa and 950 MPa with an average value of 770 MPa. No size effect was observed in the tested range of pillar diameters from 110 nm to 900 nm. Thus, in metallic glass the "smaller is stronger" effect was not observed. This observation (Fig. 5.4c) is not surprising as many MGs do not show size effects in strength. Higher values of the yield stress of MGs in comparison with their crystalline counterparts are due to the absence of existing dislocations.

Fig. 5.4d plots the strained volume versus pillar diameter. Data points for the pillars that did not have brittle fracture under compression are marked with green color. These ductile pillars could reach strain values 3 times higher than those of the fractured pillars with diameter larger than 300 nm (marked with red color) (Fig. 5.4d). Therefore, 300 nm diameter is considered to be the threshold size of transition from brittle to ductile deformation behavior of $Al_{86}Ni_9Y_5$ MG pillars under compression.

Also TEM observations of $Al_{86}Ni_9Y_5$ MG pillars after compression were performed. The enlarged TEM picture of the edge of the bulging region in a ø190 nm pillar is represented on Fig. 5.4a. The deformation showed a typical ductile behavior with bulging in 1/3 pillar's length close to the bottom. The picture of the surface topology of small-sized bulging pillars shows a mix of different areas (flow defects) registered by the contrast of TEM image, that has a wavy profile structure with a thickness around 1 nm. Flow defects were detected by the picoindenter on load displacement curves as wave-like drops and hills due to the response from the sample. The surface undulations associated with local deformation domains of a nanometer size are either hills or valleys as shown in Fig. 5.4b.

To reveal the presence of flow defects inside the bulging region of pillar volume, the 3-D contrast modulation of TEM image was performed. By including a z-component, the presence of flow defects is easily noticeable

both on the whole bulging surface and inside the pillar volume close to the wave-like surface areas. The presence of inhomogeneities in samples seems to have the same nature as α, β described in [see section 4.3.3].

The stiffness of both the sample and the stiffness of the picoindenter frame are characteristics that may have an influence on the deformation behavior of MGs. It has been demonstrated that the lower the instrument stiffness and the larger the sample size, the more brittle failure along major shear bands tends to occur. The physical meaning of these extrinsic factors is described in terms of the total energy stored in the system, which is the driving force for the propagation of a major shear band: for larger energies the propagation goes faster. Assuming the same yield strength of STZs, the strained volume needed to initiate the first major shear band is the same. It indicates that as soon as the concentration of STZs per unit of volume is large enough, fatal fracture occurs. Therefore, the critical energy per strained volume has been chosen to describe the transition threshold observed in compression of metallic glasses at nanoscale. For a total energy U_T that the system stores before fatal failure, the elastic energy per volume is (see also[23]):

$$G_e = \frac{U_T}{V} \tag{5.1},$$

where V is the total volume involved. The total energy is calculated as

$$U_T = U_S + U_M \tag{5.2},$$

where U_S and U_M are energies stored in the sample and in the machine, respectively. The energy stored in the machine is

$$U_M = U_S \frac{k_s}{k_m} \tag{5.3}$$

with k_s and k_m are the stiffness of the sample and of the machine, respectively. The stiffness of and the stored energy in a pillar can be written as:

$$k_s = \frac{\pi E_Y d}{4\rho} \tag{5.4}$$

and

$$U_S = \frac{\pi d^3 \rho \sigma_y^2}{8E_Y} \tag{5.5},$$

where E_Y is the Young's modulus, σ_y is the yield stress in compression, d is the diameter, ρ is the aspect ratio of a pillar. Assuming that the total volume involved into compression is equal to V_f, knowing k_s, U_S and the machine

compliance c_m, which is equal to the reciprocal of k_m namely $c_m = (k_m)^{-1}$, the critical elastic energy per volume is then calculated:

$$G_e = \frac{\pi d^3 \rho \sigma_y^2}{8 E_Y V_f}\left(1 + \frac{\pi E_Y d c_m}{4\rho}\right) \quad (5.6).$$

V_f represents the strained volume of the pillar just before fracture occurs and has been determined experimentally. The elastic energy per unit of volume Ge has been calculated as a function of the diameter of $Al_{86}Ni_9Y_5$ MG pillars and the results are depicted in Fig. 5.4e. For comparison, the similar dependence for $Zr_{61.8}Cu_{18}Ni_{10.2}Al_{10}$ has been plotted together with the curve for Al-based MG (Fig. 5.4e.).

Calculations of the critical elastic energy lead to a better understanding of the existence of a transition threshold as is argued as follows. After yielding the pillar undergoes plastic deformation via highly localized shear. In computer modeling and experiments have confirmed the existence of STZs.[24] These STZs have a certain distribution since the activation process does not start simultaneously for each of the potential STZ.[25] Additional energy could be needed for the activation of some of the STZs after yielding. It is logical to assume that there is a stress threshold needed to activate the particular number of STZs necessary for generation of major shear band. This barrier we call the transition threshold stress.

According to Fig. 5.4e, the amount of energy per 1 nm^3 stored in the small pillars in compression equal to units of 10^{-20} J and has the same order of magnitude, as the elastic energies in pillars with larger diameters. The dependence of G_e versus pillar diameters at a pillar diameter around 300 nm confirms the existence of the transition threshold from ductile to brittle upon increasing volume in terms of energy. Pillars with a certain diameter and consequently with sufficient strained volume enables the storage of enough energy (approximately 1.5×10^{-20} J/nm^3) to trigger a major shear band. If the pillar diameter is smaller than the transition threshold, STZs do not develop into the major shear band. According to these considerations a system with less energy stored in the volume with a certain pillar diameter should have less probability of generating the major shear band and therefore should show higher ductility.

Another issue is the influence of the chemical composition of MG on the ductility at the nanoscale. Due to the different sizes and redistribution of the atoms in different MG compositions, the localization map for STZs activation while loading will be different. Since energy is proportional to the yield stress

squared the MG with lower yield stress should have higher transition threshold since less amount of elastic energy is released during loading. Indeed for the $Al_{86}Ni_9Y_5$ MG composition with half the energy stored in the sample (Fig. 5.4e), the transition threshold is twice higher than that for the $Zr_{61.8}Cu_{18}Ni_{10.2}Al_{10}$ and equals 300 nm.

5.3.2 Mechanical performance of Al-based metallic glass nano-pillars as a function of aspect ratio

To investigate the stability under compression a set of pillars with a diameter 300±20 nm and different aspect ratios were tested. The stress-strain curves of $Al_{86}Ni_9Y_5$ MG pillars under compression are shown in Fig. 5.5 whereas Fig. 5.6 shows a nano-pillar prior and after compression.

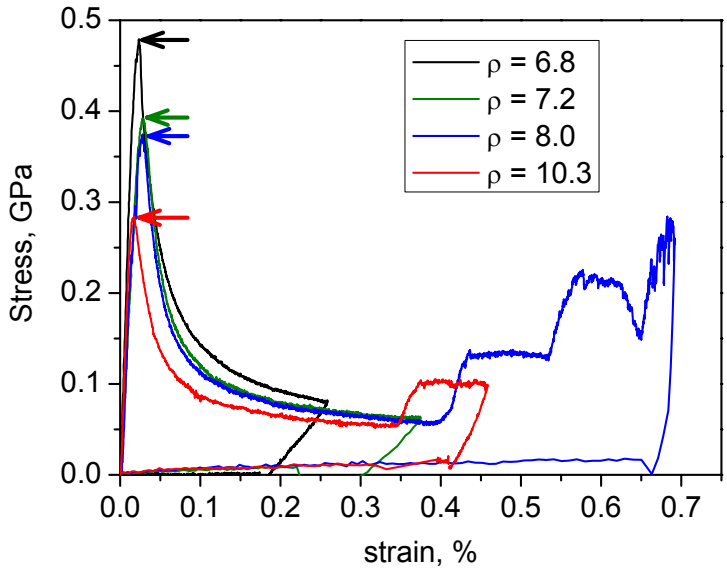

Fig. 5.5 Compression stress-strain curves of $Al_{86}Ni_9Y_5$ MG nano-pillars versus aspect ratio. The larger the aspect ratio, the lower the peak stress is (as indicated with the arrows).

The compression yield strength of the $Al_{86}Ni_9Y_5$ MG is equal to 770 MPa. As shown in Fig. 5.5, the peak stress that a MG nano-pillar can attain depends on the aspect ratio of the pillar. The larger the aspect ratio, the lower is the peak stress. The pillars may reach the yield stress at $\rho \leq 4$. In contrast, the peak stress observed of a pillar of large aspect ratio (e.g. $\rho = 10$) is only about 35 % of the actual yield stress at smaller aspect ratio.

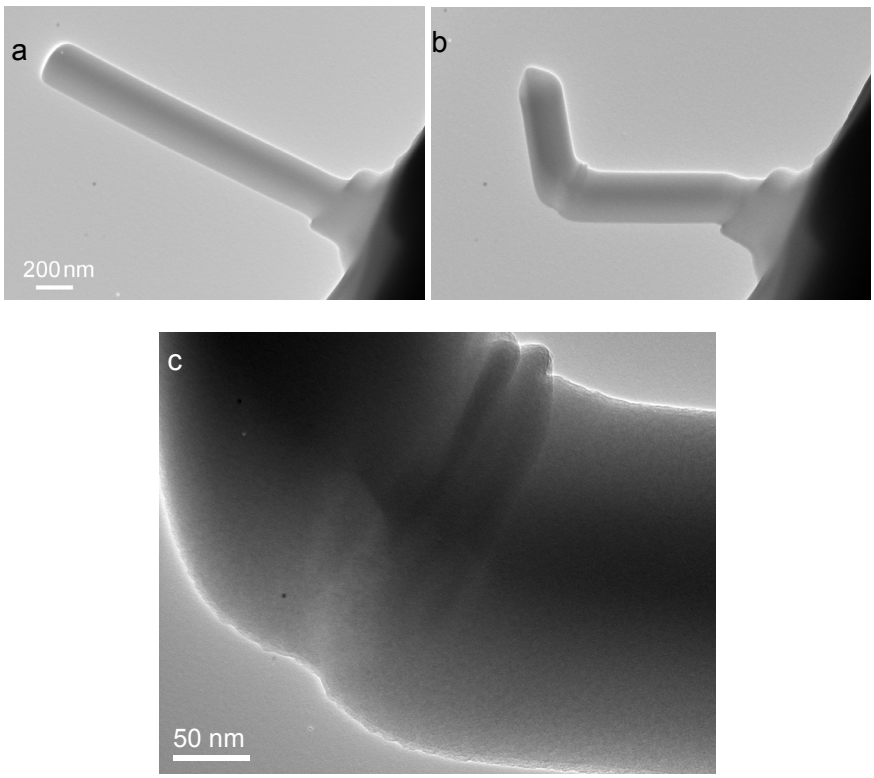

Fig. 5.6. TEM picture of $Al_{86}Ni_9Y_5$ MG ø 310 nm pillar: (a) before and (b) after compression, (c) a close view of the bending region of the pillar.

The nano-pilllars show high ductility and therefore the peak stress σ_p normalized with respect to the yield stress σ_y was chosen for the further analysis of the experiments. Fig. 5.7 reveals that the evolution of relative stress versus aspect ratio. There is a range of aspect ratios from 2 to 4 that are most suitable for proper compression experiments. The aspect ratios below 2 have a higher stability but a lower chance of forming shear band in the case of non-homogeneous deformation. Aspect ratios higher than the suitable range cause an uncontrollable buckling and bending mode.

From literature [26] it is known that in practice pillars rarely experience pure concentric axial compression. In fact the pillars experience always in practice both a bending moment and an axial force. As a result deflection is inevitable in addition to axial compression. Pillars of high aspect ratios subjected to a combined axial compression and bending will experience different modes of instability or material failure. In the current experiments a lateral sway is observed. Analysis of the lateral loads indicates that the pillar-

end translate relative to one another by a certain distance in addition to a rotation at the end. The axial forces acting on the pillar contribute to a sway and also the moment increases. The sway deformation and axial loading is referred to as P-Δ effects in mechanics. Plasticity under compression and the formation of multiple shear bands are also strongly affected by the aspect ratio of the MG samples at bulk scale. The lateral stress acts only close to the end of the pillar and it is expected that the lateral stress plays only a minor role in determining the peak stress, the plastic deformability and the shear fracture of the bulk MG samples. With decreasing aspect ratio of the MG samples, the lateral stress will continuously increase. Once a primary shear band is formed, its propagation will be hampered due to the constraint imposed by the lateral stress and the cross-head of the testing machine.

As expected the results obtained confirm the prediction made based on the Euler analysis: i.e. the critical stress for buckling according to Euler is

$$\frac{\sigma_c}{E_Y} = \frac{\pi^2}{64\rho^2} \tag{5.7}$$

where E_Y is the Young's modulus and ρ the aspect ratio of the column. Using E_Y = 57 GPa for Al-based glass, we get a good agreement with the peak stress plotted in Fig 5.7. Nevertheless, interesting is the bending behavior of these pillars given the concentration of large stresses in a small volume.

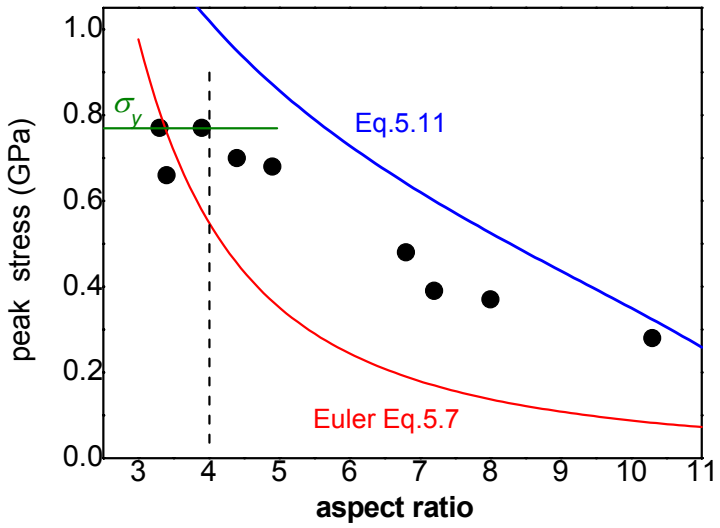

Fig. 5.7. Peak stress versus the aspect ratio of $Al_{86}Ni_9Y_5$ MG nano-pillars.

Finally, it has to be emphasized that the superior "ductility" we mention is within the framework of compression experiments whereas intrinsic ductility should be measured in tension, as shear bands in metallic glasses can be stabilized in this situation owing to the presence of a neutral axis in bending, the stabilizing effect of compression during dilatation within a shear band, and that the total strain following buckling is not representative of uniaxial loading in a stable configuration.

Following the same reasoning as Eqs.(5.1)-(5.5) the energy component which involved in the onset of bending:

$$U_{bend} = \frac{\sigma_p^2}{16E_Y} V_b \tag{5.8}$$

We assume that the volume involved in bending can be described approximately by:

$$V_b = \frac{1}{4}\pi d^2 l_b = (1-\varepsilon_b)\frac{1}{4}\pi d^2 l \tag{5.9}$$

where ε_b is the strain of the pillar. The energy involved in bending can be expressed in terms of aspect ratio:

$$U_{bend} = \frac{\sigma_p^2}{64E_Y}(1-\varepsilon_b)\pi\rho d^3 \tag{5.10}$$

By using Eqs.5.10, σ_p can be written as a function of the aspect ratio ρ:

$$\sigma_p \propto \sqrt{\frac{1}{\rho}} \tag{5.11}$$

The higher the aspect ratio, in the range from 4 to 12, the lower the peak stress level reached.

We believe that extrinsic factors have also an effect on the critical aspect ratio. Stiffness values of both the sample and the picoindenter should be taken into account as extrinsic characteristics that have an influence on the deformation behavior of MG samples with different aspect ratios. It has been demonstrated that the higher the instrument stiffness and the smaller the sample size, the more ductile failure tends to occur.[27] Assuming the same strength of shear transformation zones (STZs), the elastic strained volume needed to initiate the first major shear band is the same. It indicates that as soon as the number of STZs per unit of volume unit is high enough fracture will occurs.

5.3.3 Deformation induced ductility of metallic glasses

Typical behavior of thick $Al_{86}Ni_9Y_5$ pillars (diameter typically larger than ø300 nm) is catastrophic failure in single cycle compression due to localized deformation in shear banding, which is the characteristic behavior of metallic glasses at macroscopic dimension (see section 5.3.1). The results of the cyclic experiments are presented in Fig. 5.8 for three pillars of different diameters: ø552 nm, ø357 nm, and ø186 nm.

By applying cyclic deformation, the ductility of the large samples (~ø500 nm) was significantly increased, i.e. up to -100% true strain in total in 10 cycles of compression and yet without break down (Fig. 5.8g). Moreover, both the yielding and peak stresses continuously decrease from the first cycle of compression to the successive cycles. That is to say, noticeable strain softening was observed in cyclic deformation of MG pillars. Close-up examinations indicate that strain softening occurred in each individual cycle of compression, i.e. an observable decrease of flow stress was recorded in each of the true stress-strain curves. The same phenomena, i.e. strain induced ductility and softening, were observed on thinner Al-MG pillars as shown in Fig. 5.8h and 5.8i. The primary difference among the three pillars of different sizes is the compression cycles needed to convert them from brittle fracture to ductile failure. Thicker pillars need a larger number of deformation cycles to become ductile. As the diameter of pillars decreases to a threshold value (about 300 nm for $Al_{86}Ni_9Y_5$ MG), thin pillars may deform in a fully ductile manner ever in a single compression cycle.

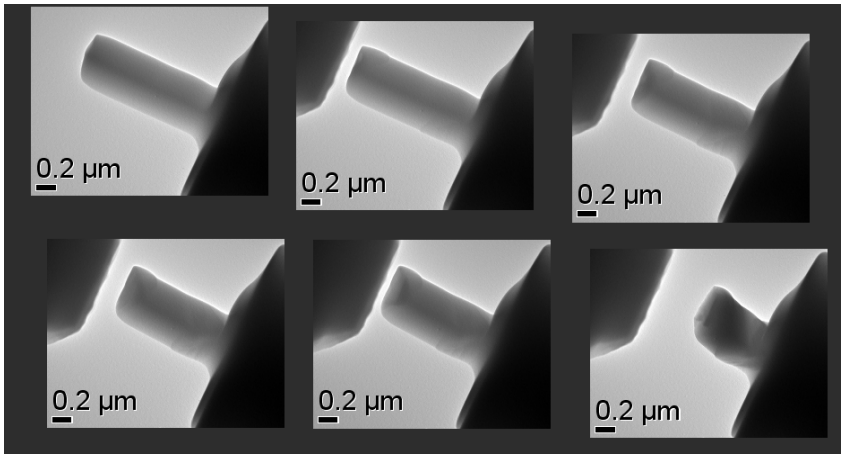

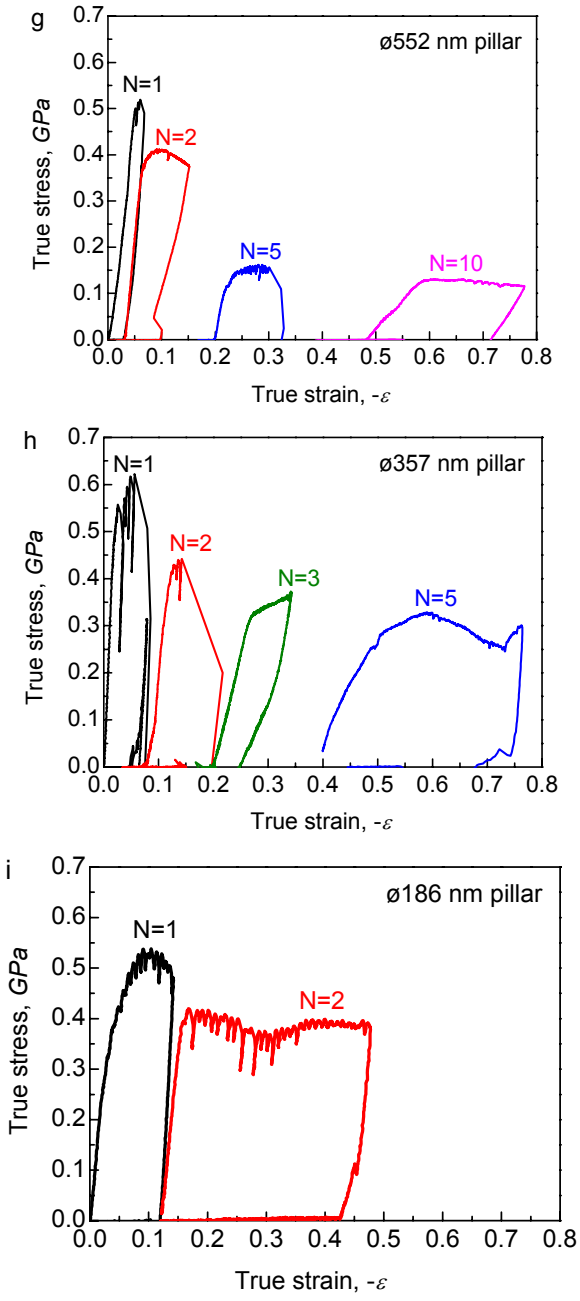

Fig.5.8. TEM video frames showing the deformation of a ø552 nm MG pillar after each of the first 5 cycles (a-f) and true stress-strain curves of cyclic loading-unloading tests: (g) 10 cycles compression of ø552 nm pillar, (h) 5 cycles compression of a ø357 nm pillar and (i) 2 cycles compression of a ø 186nm pillar.

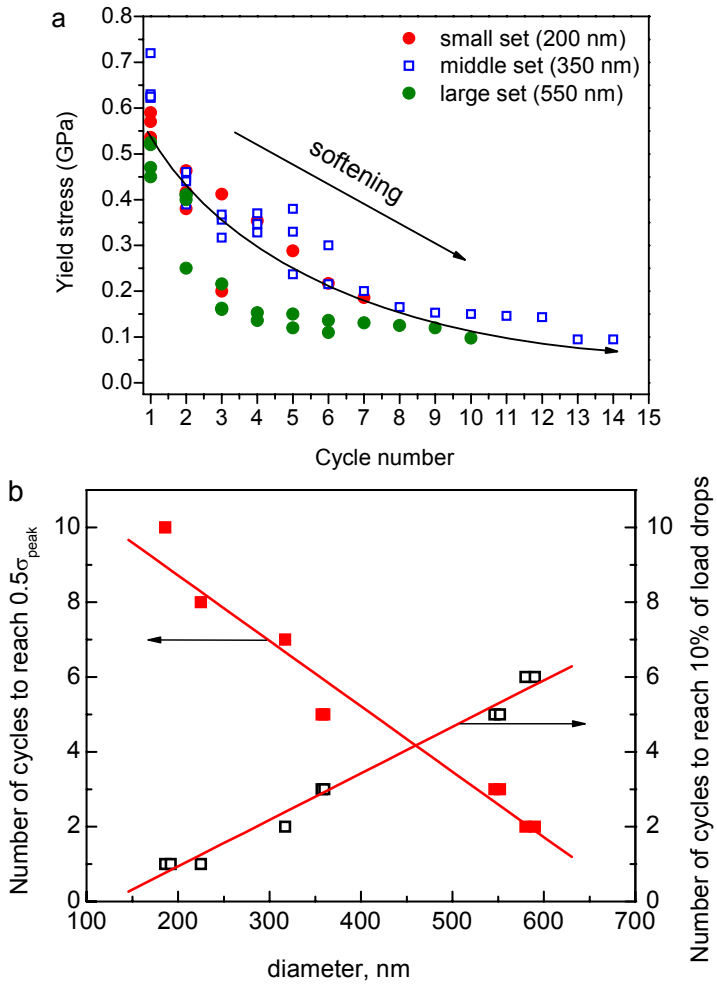

Fig.5.9. (a) Yield stress versus number of the cycle. Solid line is the theoretical curve (b) Number of cycles versus diameter of the pillar. The increase in toughness increases with increasing diameter (open squares, right side) whereas the number of cycles to reach half of the peak stress is decreasing with increasing diameter (solid squares, right side).

Fig. 5.9a shows the dependence of the yield stress on the number of cycles whereas Fig. 5.9b indicates the occurrence of softening and toughening effects in MG. For larger pillars the number of the cycles that is necessary to reach plastic flow was higher than for the smaller pillars. For each pillar size there is a certain number of cycles at which a more ductile behavior is attained. In order to avoid catastrophic failure a 10% load drops of the ultimate load have been selected as a reference point for the experiments. The reduction in yield stress to 50% has been chosen as a quantitative

characteristic to describe softening effects for each pillar size. The maximum value observed of the load drops for the small pillar diameters is 10%.

Since it is rather difficult to observe structural features in MG during compression, the discussion on the deformation mechanism of MGs is still under debate. We stick to the most commonly accepted theoretical description explaining the processes from a mechanistic viewpoint. The distribution of free volume in MGs is affected by the chemical composition and related to the glass transition temperature. When compressing MG a certain fraction of the material γ_k is activated as free volume in the k^{the} cycle resulting in a local shear transformation zones whereas the rest of the material of concentration 1-γ_k is only elastically strained. The collective behavior of these shear transformation zones, which combines the integration of the local shears, determines the macroscopic response in elastic, viscoelastic and plastic regimes.

For a large-sized sample, there is limited influence of free surface, and volume effects will predominant the influence on the deformation behavior. But when we downsize the specimen we argue that free surfaces become more important. Upon decreasing the size of the sample down to 100 nm, the total number of STZs decreases, assuming the same interaction of free atoms during compression as for bulk specimens. On the other hand, with decreasing sample size down to hundreds of nanometers, the distribution of the free volume density may also become rather inhomogeneous.

Fatigue failure of crystalline materials is usually related to subcritical crack growth described by Paris law.[28] Such an approach assumes that all structures contain flaws, and that cracks may initiate and propagate early in service life. Here we assume that after each unloading cycle, the stresses that were concentrated near the STZs areas are released. The structure will be changed after the first cycle and there is a lower probability that the next compression cycle will start near the former flow defect area, since that was already strengthened.

The local strengthening effect is followed by the release of the residual stresses upon unloading, i.e. resulting in softening. We propose that a visco-elastic model is appropriate to describe the softening. According to the Maxwell-Weichert model we assume a number of units N_k, each consisting of a spring and damping term placed in series. It follows that the relaxation modulus in response to instantaneous loading during the k-th cycle can be formulated as:

$$E_Y(t) = \sum_{i=1}^{N_k} E_{Y,i} \exp\left(-\frac{E_{Y,i}t}{\eta_i}\right) = \sum_{i=1}^{N_k} E_{Y,i} \exp\left(-\frac{t}{\tau_i}\right) \tag{5.12}$$

where η_i is the damping coefficient determining the relaxation time τ_i:

$$\tau_i = \frac{\eta_i}{E_{Y,i}} \tag{5.13}$$

Estimates of the parameters in the modified Kelvin-Maxwell-Weichert model (with a spring representing the elastic areas of concentration $(1-\gamma_k)$ and a dashpot representing the γ_k concentration of viscoelastic STZs in parallel) can be obtained by best-fitting to the experimental results of the relaxation modulus. The general expression for the stress as it depends on the relaxation modulus and the total stress is described by an elastic part of fraction $1-\gamma_k$ and a visco-elastic part of fraction γ_k related to the STZ:

$$\sigma_k = (1-\gamma_k)\sigma_k^e + \gamma_k \sigma_k^v \tag{5.14}$$

where $\dot{\varepsilon}$ is the strain rate and ***t'*** is an integration variable. The visco-elastic part of Eq. (5.18) then simplifies to:

$$\sigma_k^v = \dot{\varepsilon}\int_0^{t_0} E_{Y,k}(t-t')dt', t_0 < t \tag{5.15}$$

yielding:

$$\sigma_k^v = \dot{\varepsilon}\int_0^{t_0} \sum_{i=1}^{N_k} E_{Y,k,i} \exp\left(-\frac{t-t'}{\tau_i}\right)dt' = \dot{\varepsilon}\sum_{i=1}^{N_k} E_{Y,k,i}\tau_i \exp\left(-\frac{t}{\tau_i}\right)\left(\exp\left(\frac{t_0}{\tau_i}-1\right)\right), t_0 < t$$

(5.16)

or

$$\sigma_k^v = \dot{\varepsilon} \sum_{i=1}^{N_k} \eta_i \exp\left(-\frac{E_{Y,k,i}t}{\eta_i}\right)\left(\exp\left(\frac{E_{Y,k,i}t_0}{\eta_i}-1\right)\right), t_0 < t \tag{5.17}$$

Assuming that units of our system are equal to each other $i_1=i_2=\ldots=i_N$ we arrive at the simplified equation of stress:

$$\sigma_k = (1-\gamma_k)E_{Y,k}\varepsilon + \gamma_k \dot{\varepsilon}\,\eta \exp\left(-\frac{E_{Y,k}t_k}{\eta}\right)\exp\left(\frac{E_{Y,k}t_0}{\eta}-1\right) \tag{5.18}$$

Taking into account that after the first cycle t=t_0, and the concentration of activated events at the k-th cycle is γ_k, i.e. equal to N_k / N_o, and assuming that the process of compression is continuous with respect of the time, then:

$$t = \frac{\Lambda}{s} \tag{5.19}$$

where Λ is the total displacement for each cycle k and s is the speed of compression. The basic description of number of defects during the cyclic deformation at larger scale can be described by

$$\gamma_k = k^{\phi}\left(\frac{d_k}{d_0} - 1\right)^{\psi} \tag{5.20}$$

The dependence of number of defects were calculated experimentally, where parameter ψ is equal to 1.3. Eg.5.20 is valid only for the limited number of cycles (k). The component k^{ϕ} represents chemical composition dependence, where ϕ is constant determined from boundary conditions.

According to experimental fit the apparent Young's modulus E_Y also changes with the number of cycles

$$E_{Y,k} = E_Y (k^{\phi})^{-1} \tag{5.21}$$

The equation for the yield stress as a function of the number of cycles becomes:

$$\sigma_k = \left(\frac{1-k^{\phi}}{k^{\phi}}\right)\left(\frac{d_k}{d_0} - 1\right)^{\psi} E_Y \varepsilon + \dot{\varepsilon}\eta k^{\phi}\left(\frac{d_k}{d_0} - 1\right)^{\psi} \exp\left(-\frac{E_Y \Lambda}{\eta s k^{\phi}}\right)\exp\left(\frac{E_Y t_0}{\eta k^{\phi}} - 1\right) \tag{5.22}$$

The theoretical curve of σ^k has been plotted (Fig. 5.9) as a function of k^{ϕ} and it is seen that the theoretical curve plotted according to this model fits to the experimental results very well.

The central question addressed in this study is: What actually means the yield stress in a metallic glass upon repeated loading and unloading? Is this related to the stress level at which shear bands are formed and get reactivated? Is it linked to the stress, at which several non-correlated local shear events happen? In principle two mechanisms can be operational: homogeneous flow (at high temperatures and low strain rates) when the whole volume of the sample statistically contributes to plastic deformation, and non-homogeneous flow (low temperatures and high strain rates) when deformation gets localized into shear bands. If non-correlated deformations of STZ are assumed a

decreasing yield stress upon repeating loading and unloading is expected. Residual stresses are frozen in the microstructure from a previous loading that will contribute to the external stress and help to activate STZs. The existence of a residual stress supports the idea, that *homogenous* deformation is actually a visco-elastic deformation of STZ. It is reversible at its first moment, but due to a relaxation of internal stresses around STZ due to structural relaxation and/or visco-elastic deformation of neighborhood STZs this deformation becomes irreversible due to the 'loss of memory' in its surrounding. The increase in ductility might be explained in terms of absorbed mechanical energy. The energy per unit of volume which involved in compression is equal to $\int \sigma d\varepsilon$. Each compression cycle leads to softening $\sigma_{n+1} < \sigma_n$. Assuming that energy per unit of volume is about constant before failure the ductility with each cycle should increase $\varepsilon_{n+1} > \varepsilon_n$.

5.4 Conclusions

Extended investigations of nano-sized pillars fabricated and tested in-situ in a TEM with Al-base compositions and diameters ranging from 100 nm to 900 nm showed a strong dependence of mechanical properties on the pillar diameter. The $Al_{86}Ni_9Y_5$ taper-free metallic glass has shown extremely high values (around 300 nm) for the transition threshold of the ductility. In metallic glasses with these dimensions, such a high plasticity has never been observed before. It is relevant to note that we did not observe any change in the amorphous state due to the preparation conditions (FIB) and after deformation.

The pillar aspect ratio has a large influence on deformation behavior as well. Very high strains and ductility were achieved in bending at high aspect ratios, which reveals an interesting possibility for future application developments with materials based on $Al_{86}Ni_9Y_5$ MG.

It can be concluded that the deformation in MG, which becomes apparent through softening and toughening effects, is revealed and characterized through the cyclic micro- and nanopillar tests. The proposed experimental technique of loading and unloading cycles is capable of determining the mechanical properties in metallic glasses, and opens a new route to the characterization of the deformation behavior of metallic glasses down to the 100nm sizes.

References

1. C.C. Hays, C.P. Kim, and W.L. Johnson, Physical Review Letters, 84, 2901 (2000).
2. Y. Kawamura, T. Itoi, T. Nakamura and A. Inoue, Materials Science Engineering A 735, 304-306 (2001).
3. A.R. Yavari, K. Georgarakis , W.J. Botta, A. Inoue, G. Vaughan, Physical Review B 82, 172202 (2010).
4. N. Mattern, T. Gemming, J. Thomas, G. Goerigk, H. Franz, J. Eckert, Journal of Alloys and Composites 495, 299 (2010).
5. L.Y. Chen, Z.D. Fu, G.Q. Zhang, X. P. Hao, Q.K. Jiang, X.D.Wang, Q.P. Cao, H. Franz, Y.G. Liu, H.S. Xie, S.L. Zhang, B.Y. Wang, Y.W. Zeng, and J.Z. Jiang, Physical Review Letters 100, 075501 (2008).
6. D.T.A. Matthews, V. Ocelík, P.M. Bronsveld and J.Th.M. De Hosson, Acta Materialia. 56, 1762 (2008).
7. K. Mondal, T. Ohkubo, T. Toyama, Y. Nagai, M. Hasegawa and K. Hono, Acta Materialia 56, 5329 (2008).
8. D.H. Bae, S.W. Lee, J.W. Kwon, X.D. Wang and S. Yi, Materials Science Engineering A 111, 449-451 (2007).
9. C.Q. Chen, Y.T. Pei, O.V. Kuzmin, Z.F. Zhang, E. Ma, J.Th.M. De Hosson, Physical Review B 83, 180201(R) (2011).
10. O.V. Kuzmin, Y.T. Pei, J.Th.M. De Hosson, Applied Physics Letters 98, 233104 (2011).
11. D. Jang, C. T. Gross, and J. R. Greer, International Journal of Plasticity 27, 858 (2011).
12. D. Jang, and J. R. Greer, Nature Materials 9, 215 (2010).
13.R. Maass, R., D. Klaumunzer, G. Villard, P.M. Derlet , J.F. Loffler, Applied Physics Letters 100, 071904 (2012)
14 .D. Klaumunze, A. Lazarev, R. Maass, F.H. Dalla, A. Vinogradov,J.F. Loffler, Physical Review Letters 107, 185502 (2011).
15. C.Q. Chen, Y.T. Pei, J.Th.M. De Hosson, Acta Materialia 58, 189 (2010).
16. J.R. Greer, J. Th.M. De Hosson, Progress in Materials Science 56, 654–724 (2011).
17. A. Inoue, Progress in Materials Science 43, 365 (1998).
18. Z.F. Zhang, H. Zhang, X.F. Pan, J. Das, J. Eckert, Philosophical Magazine Letters, 85, 513 (2005).
19.. C.J. Gilbert, V. Schroeder, R.O. Ritchie, Metallurgical Materials Transactions 30A, 1739 (1999).
20.. R. J. Milne, A. J. Lockwood, B. J. Inkson Journal of Physics: Conference 241, 012059 (2010).
21. J.J. Lewandowski, W.H. Wang and A.L. Greer, Philosophical Magazine Letters 85, 77 (2005).
22. O.V. Kuzmin, Y.T. Pei, C.Q. Chen and J.Th.M. De Hosson, Acta Materialia. 60 (2012) 889.
23. Z. Han, W.F. Wu, Y. Li , Y.J. Wei, H.J. Gao, Acta Materialia 57, 1367 (2009).
24. W.L. Johnson, K. Samwer, Physics Review Letters 95, 195501 (2005).
25. Y. Wu, H.X. Li, Z.Y. Liu, G.L. Chen, Z.P. Lu, Intermetallics 18, 157 (2010).
26. P.J. Dowling, P.R. Knowles, G.W. Owens, Structural steel design, Butterworths, London, (1998).
27. Z. Han, W.F. Wu, Y. Li , Y.J. Wei, H.J. Gao, Acta Materialia 57, 1367–1372 (2009).

28.. P.C. Paris, M.P. Gomez, & W.E Anderson, Trend in Engineering 13, 9–14 (1961).

Chapter 6

Mechanical performance of metallic glass nano-pillars in tension

Metallic glasses have drawn considerable attention due to the ability to resist high mechanical stresses; however the lack of ductility remains the Achilles heel in the applicability to materials engineering and technology. This Chapter presents rather unique tensile experiments which were performed on $Al_{86}Ni_9Y_5$ and $Zr_{61.8}Cu_{18}Ni_{10.2}Al_{10}$ MG at nanoscale with diameters ranging between 100 and 500 nm. The in situ TEM observations were synchronized with picoindentation data and revealed a transition from brittleness on larger sizes to a plasticity performance while down sizing to hundreds of nanometers. Strain hardening effects were also observed. Our tensile experiments reveal the deformation behavior of MGs at nanoscale and address several relevant questions about the nature of intrinsic and extrinsic size effects at this length scale.

6.1 Introduction

Metallic glasses (MGs) have been widely studied as a new class of advanced materials owing to their desirable properties, such as outstanding yield strength and fracture strength, large elastic strain, and superior wear and corrosion resistance. Since the first publication by Paul Duwez and collaborators in the Sixties, metallic glasses have attracted considerable interest. However, their main drawback is the catastrophic and instantaneous brittle failure under tensile loading, originating from severe plastic-strain localization in a narrow region called a shear band.[1] As a consequence it is of fundamental scientific and engineering interests to find out whether and how, the strength of MG alters when the physical dimensions are becoming smaller.[2] Also, in terms of fundamentals of plasticity, the way in which the specimen dimensions affect the 'intrinsic' strength and plasticity of amorphous metals is an issue of scientific relevance.[3,4]

For bulk metallic glasses, the plastic deformation is thought being localized in a narrow region of localized shear. Following micro-compression experiments on crystalline materials, several research groups have carried out

similar compression experiments on metallic glassy micropillars and reported a correlation between reduced size and several mechanical properties: maximum plastic strain before failure, yield strength and deformation mode. Nonetheless, several papers are inconsistent, sometimes due to lack of sufficient accurate experimental data and lack of statistics. Also, the stress-strain response of micro- and nanopillars during compression can be characterized by significant stochastic effects, both in crystalline and in glassy pillars.[5] Another reason for the lack of agreement is the imperfect specimen geometry, which is, tapering and buckling of cylindrical pillars in compression tests.[6,7,8]

In tension the plastic elongation of MGs is usually very small, i.e. virtually equal to zero. However, a higher density of shear transformation zones (STZs) may produce local shear transformations that can mediate a plastic flow without immediate catastrophic failure. Despite this potential and the fact that under specific conditions MGs can indeed exhibit plastic deformation, the problem with MGs is that plastic strains are commonly observed in extremely thin shear bands. The concentrated deformation in softer regions trigger rapid failure as soon as major shear banding sets in, leaving a little opportunity for an observable ductility in tension.

In contrast to non-crystalline materials, effects of specimen size on the apparent strength of crystalline materials have received a lot of attention, in particular under compressive loading. For single-crystal metals in the micrometer and submicron regime, a "smaller is stronger" trend has been established, because the smaller the specimen size, deformation mechanism becomes dislocation nucleation and starvation controlled (assuming no pre-existing dislocations), elevating the stress field required to cause yielding and sustain plastic flow.[9,10] It is therefore intriguing whether an analogous "size effect" can also exist in MGs. A "the smaller the better" idea has arrived at the MGs research field. As such, small-volume MGs are especially attractive for applications such as in micro- and nano-electromechanical systems (MEMS and NEMS).[11,12] A number of experiments have already been carried out in recent years to look into the possibility that specimen size influences the apparent strength of MG.

A variety of alloy systems have been examined, including MGs based on Pd, Zr, Fe and Mg.[13,14,15] Unfortunately, the results have led to a controversial debate about deformation in compression as well as in tension. What happens if we decrease the geometrical size of the specimen close to or below the shear band size? Does the plastic flow mechanism change when its dimension goes

down to the minimum thickness of a shear band, and if so, how? Therefore, it is of importance to carry out careful tests to elucidate thoroughly quantitative measurements whether nanometer sized MG specimens, at least those made using a focused ion beam (FIB), are intrinsically ductile under uniaxial compression as well as tension. In contrast to the previous chapters the present chapter concentrates on tensile experiments but a comparison with compression experimental results presented in previous chapters will also be made.

In-situ TEM tensile experiments were performed using a Hysitron picoindenter TEM holder (Hysitron Inc., Minneapolis, MN, USA) equipped on JEOL 2010F TEM, with a home-developed Al-alloy tip holder and W tensile tip. Al-alloy holder was designed and developed in order to achieve good calibration and to avoid undesirable mechanical noise due to over weight during tensile experiments. A tungsten tensile tip was designed and made by electrochemical polishing and afterwards milled by FIB to the desired shape (Fig. 6.1). The dimensions of the tip were chosen in order to make tensile experiments of nanopillars with diameter range from 100 to 500 nm (Fig. 6.1). The tensile stage has several features, which are particularly critical to the present study. It is integrated with a miniature capacitive load–displacement transducer permitting load and displacement measurements of high resolution (~0.3 μN in load, ~1 nm in displacement). The experiments have been run in displacement controlled mode with constant strain rate ~ 10^{-2} s^{-1}.

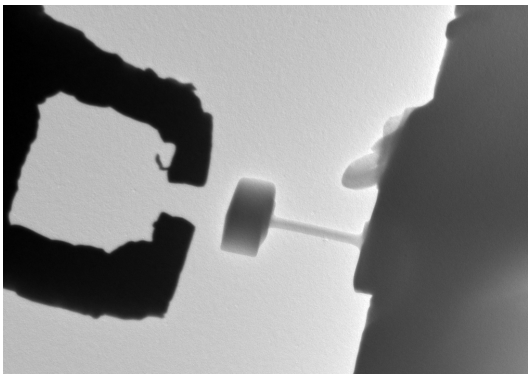

Fig. 6.1. TEM picture of Fib milled W tensile tip and $Al_{86}Ni_9Y_5$ MG nanopillar 250 nm in diameter

6.2 Results and discussion

Tensile experiment on Al-based and Zr-based MGs

In particular we discuss tensile experiments of $Al_{86}Ni_9Y_5$ and $Zr_{61.8}Cu_{18}Ni_{10.2}Al_{10}$ MG pillars with diameters ranging from 100 to 500 nm. Upon testing specimens of larger diameter, the load increases proportionally up to yielding followed by brittle failure. The fracture surface shows a major shear phenomenon under 45 degrees, i.e. similar to the behavior of mm-sized MG specimens. The localization of the fracture could occur stochastically on the specimen surface over entire length, depending on the local concentration of smaller pre-shear which contribute to major shear band (Fig. 6.2).

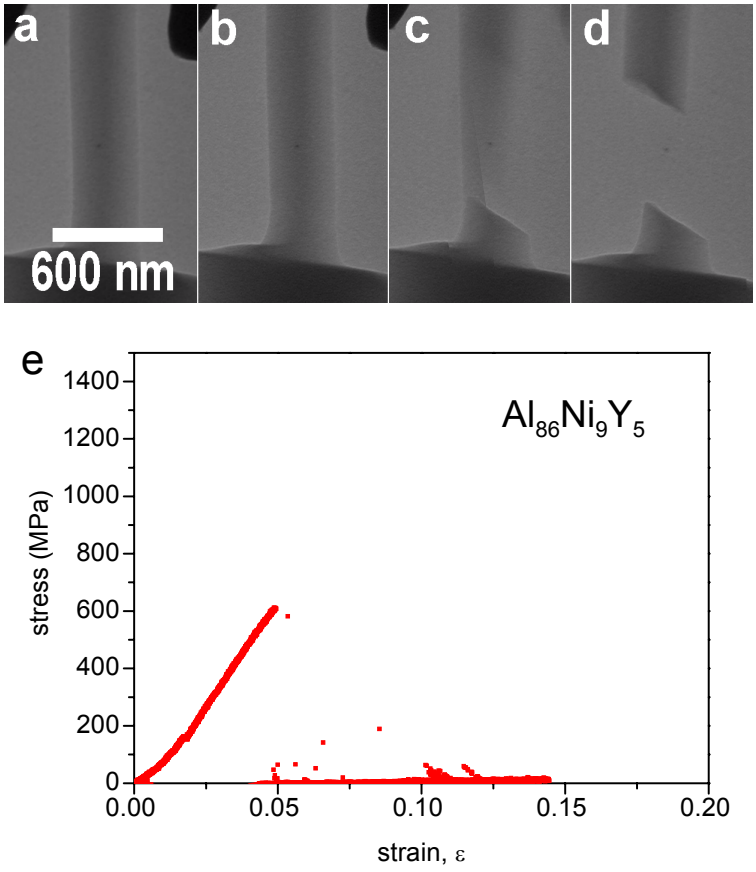

Fig. 6.2. Video frames recording the deformation of a ø400 nm $Al_{86}Ni_9Y_5$ MG pillar in tension at displacement rate controlled mode. Grabbed video frames show the deformation structures before, during and after tension (a-d). True stress-strain curve (e).

The deformation behavior alters in specimens with diameters around 250 nm. Upon tension, specimens show areas with a higher concentration of shear deformation (Fig. 6.3(a-d)). However, deformation results in catastrophic failure, as these areas interact with each other. The stress-strain curve (Fig. 6.3e) does not show any visible stress drops since the local deformation might occur at several positions on the specimen surface simultaneously and the picoindenter cannot resolve those when brittle failure occurs. An intriguing effect for these specimens is significant strain hardening (shown on Fig. 6.3e and Fig. 6.4e) that represents the size dependence in tension at this scale.

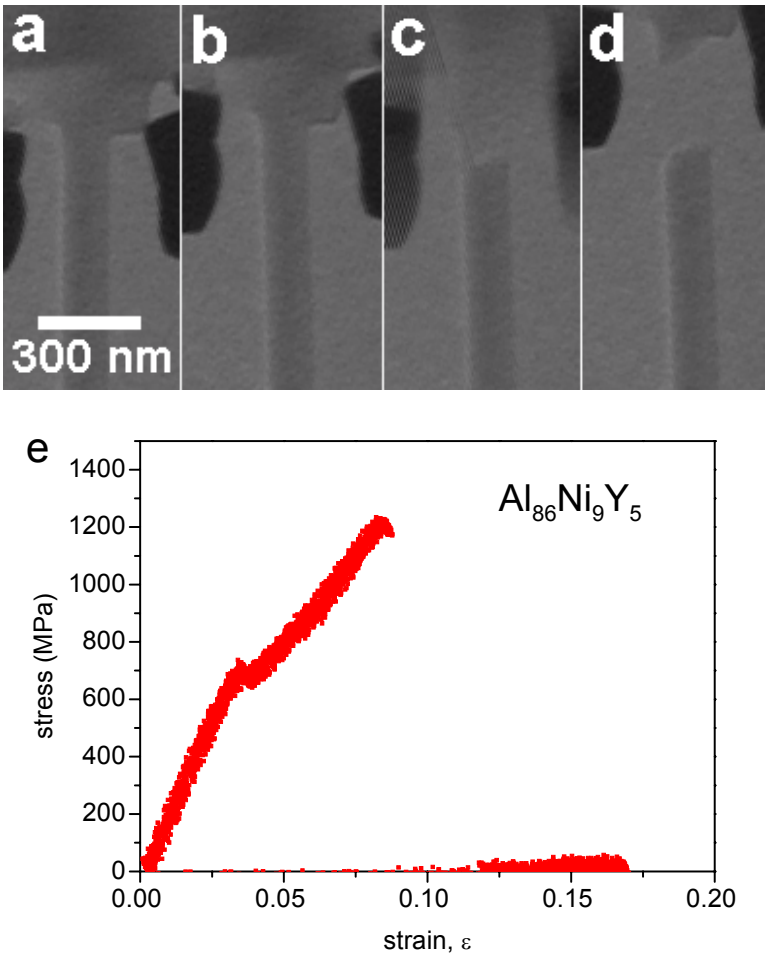

Fig. 6.3. Video frames recording the deformation of a ø220 nm $Al_{86}Ni_9Y_5$ MG pillar in tension at displacement rate controlled mode. Grabbed video frames show the deformation structures before, during and after tension (a-d). True stress-strain curve (e).

The localization of shear bands is different in larger pillars. The latter show more localized areas with shear bands, which propagate to one major shear band. The ultimate stress in smaller specimens is higher in comparison with larger diameter specimens. An increase of true strain up to 8 % was observed for this diameter range of MG pillar specimens (Fig.6.3e). The smallest specimen diameter in the range down to 100 nm shows more plasticity, necking and an increased strain hardening effect (Fig. 6.4e). Fracture behavior is similar to plastic crystalline materials, i.e. without a 45 degree fracture plane as occurs in larger specimens (Fig. 6.4(a-d)). The plastic strain reached is around 8%. The most important observation of tensile experiments is that no clear size effect is seen on the yield stress but a clear increase in the ultimate strength is observed with deceasing the diameter of MG pillars (Figs. 6.2e – 6.4e).

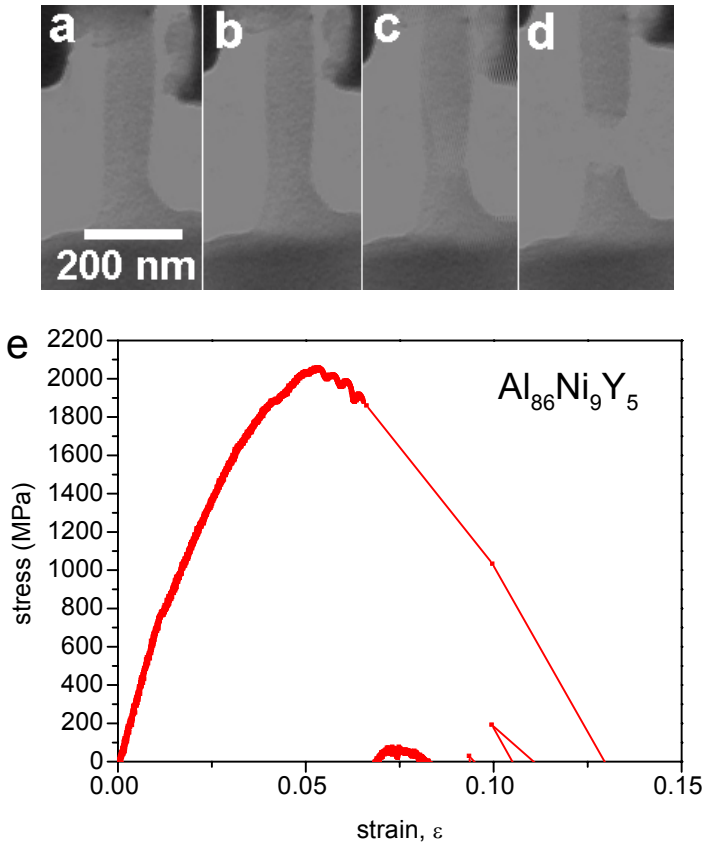

Fig. 6.4. Video frames recording the deformation of a ø100 nm $Al_{86}Ni_9Y_5$ MG pillar in tension at displacement rate controlled mode. Grabbed video frames show the deformation structures before, during and after tension (a-d). True stress-strain curve (e).

According to our previous results (see Section 4.3.3) the MG composition has a large influence on the change in deformation behavior at the nanoscale. Therefore tensile experiments of $Zr_{61.8}Cu_{18}Ni_{10.2}Al_{10}$ MG have been performed in order to compare with and also show strain hardening effects observed in $Al_{86}Ni_9Y_5$ MG.

At larger diameters and before the transition threshold of $Zr_{61.8}Cu_{18}Ni_{10.2}Al_{10}$ MG, the specimens undergo brittle fracture after reaching a yield point. Fig. 6.5(a-d) shows TEM video frames of a pillar 350 nm in diameter before, during yielding and after brittle fracture. The yield stress was about 1050 MPa (Fig. 6.5e)

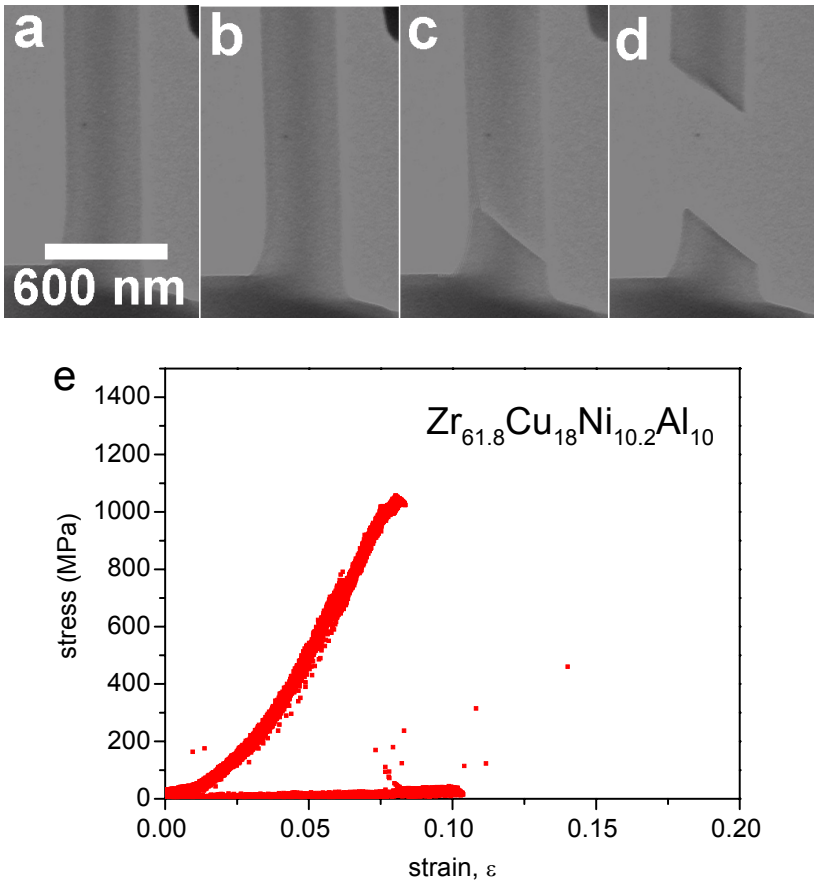

Fig.6.5. Video frames recording the deformation of a ø350 nm $Zr_{61.8}Cu_{18}Ni_{10.2}Al_{10}$ pillar in tension at displacement rate controlled mode. Grabbed video frames show the deformation structures before, during and after tension (a-d). True stress-strain curve (e).

Upon decreasing diameter $Zr_{61.8}Cu_{18}Ni_{10.2}Al_{10}$ specimens show up to 15% (relatively to the yield point) a strain hardening phenomenon before brittle fracture occurs (Fig. 6.6(a-d)). After yielding at ~ 1000 MPa specimens show strain hardening up to 1250 MPa and 4% of plastic strain (Fgi. 6.6e). Again, the stress-strain curves of Zr-based MG pillars in the diameter range studied indicate no size effects on the yield stress but a clear increase in the ultimate strength (Figs. 6.5e – 6.7e).

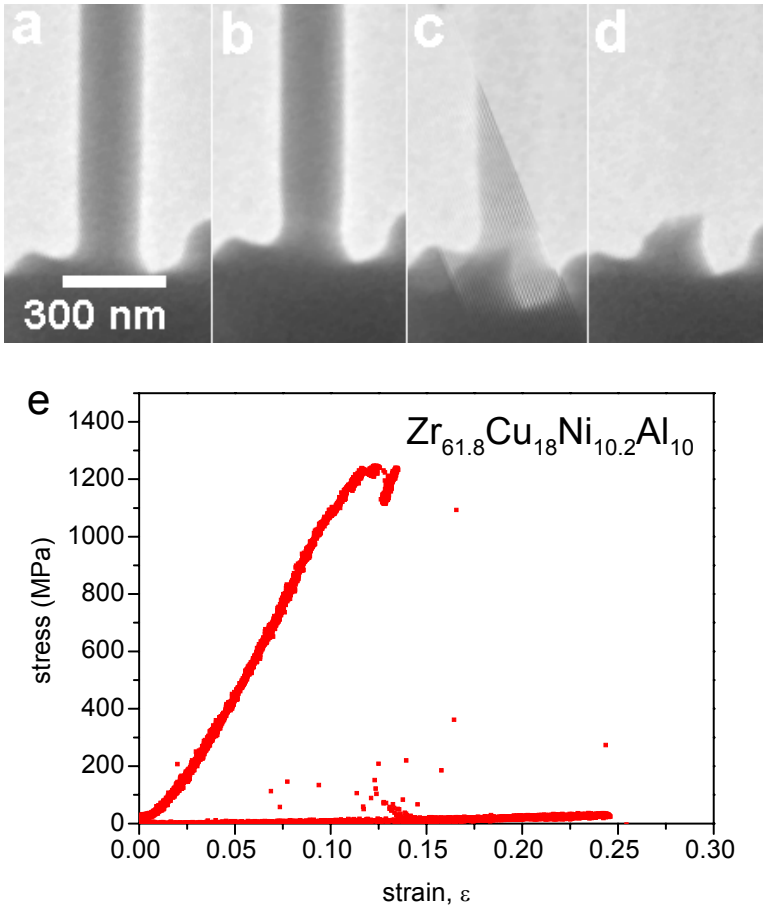

Fig.6.6. Video frames recording the deformation of a ø220 nm $Zr_{61.8}Cu_{18}Ni_{10.2}Al_{10}$ MG pillar in tension at displacement rate controlled mode. Grabbed video frames show the deformation structures before, during and after tension (a-d). True stress-strain curve (e).

Tensile specimens with the diameters smaller than 120 nm show work hardening and after yielding, they reach an ultimate tensile strength up to 25% and 7% of plastic strain after yielding.

The most intriguing behavior in tension was observed in $Al_{86}Ni_9Y_5$ specimens smaller than 120 nm in diameter. Notwithstanding that larger pillars show failure via localized shear bands after elastic loading, smaller sized specimens, below 120 nm, show a rather ductile behavior: plasticity, work hardening, ultimate tensile strengthening and necking. Plastic deformation was also confirmed by a rather homogeneous decrease in specimen diameter (up to 4%) over the full length.

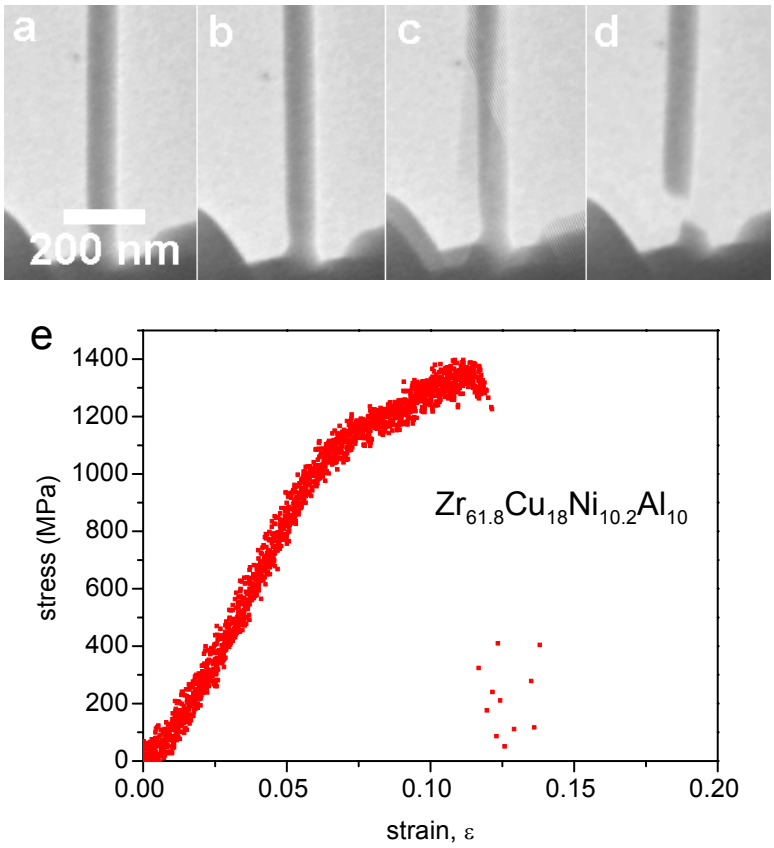

Fig.6.7. Video frames recording the deformation of a ø120 nm $Zr_{61.8}Cu_{18}Ni_{10.2}Al_{10}$ MG pillar in tension at displacement rate controlled mode. Grabbed video frames show the deformation structures before, during and after tension (a-d). True stress-strain curve (e).

The plasticity that was achieved is about 8%, which is a significant value for this type of MG composition. The yield stress reaches 1000 MPa for the smallest pillar diameter which is similar and consistent with larger diameters, however strain hardening effect is significantly increasing upon decreasing specimen size (Fig. 6.6e and Fig. 6.7e).

Indeed, under compression we have noted intrinsic and extrinsic size effects in the experiments on the $Al_{86}Ni_9Y_5$ and $Zr_{61.8}Cu_{18}Ni_{10.2}Al_{10}$ (see previous chapters) and importantly the current tensile experiments allow to avoid some artifacts (tapering, shear band formation due to friction).

The phenomena of size effects in MGs at nanoscale can be explained in following manner. In order to generate major shear the large energy and certain interaction volume is required. Large pillars ~ 500 nm have enough volume and thus stored elastic energy to generate major shear band similar to bulk mm-sized specimens. Our previous compression tests on specimens of about 350 nm in diameter (chapter 5) show that major shear bands occur by a collective behavior of a certain density of smaller ones. Upon decreasing the diameter to 120 nm the number of shear events increases; however, they do not generate a major shear band because of the limited interaction volume, which is even smaller than for compression tests.

Compression versus tension

The difference in the mechanical response depends on intrinsic and extrinsic properties of the material investigated. In this section the comparison between compression and tensile experiments of MGs at the nanoscale will be discussed. Even though some bulk metallic glasses can exhibit compressive strains of over 25% [12], they still fracture abruptly under uniaxial tensile stresses. This fact indicates that metallic glasses exhibit a tension-compression asymmetry as far as plasticity is concerned. The latter is usually interpreted by continuum mechanics, which neglects the atomic structure of materials. However, metallic glasses show an asymmetry that can be linked to the amorphous structure and pre-treatments.

The interesting deformation behavior of $Zr_{61.8}Cu_{18}Ni_{10.2}Al_{10}$ specimens with cross-sections 60 nm by 266 nm is presented in Fig. 6.8. Obviously the specimens with the same cross-section (square) 1.6×10^5 nm^2 did not show any plasticity at this chemical composition. The region at the bottom of the specimen Fig. 6.8(c-d) undergoes plastic behavior. This observation points at the influence of the rectangular cross section (i.s.o. squared), which is different for the compression experiments.

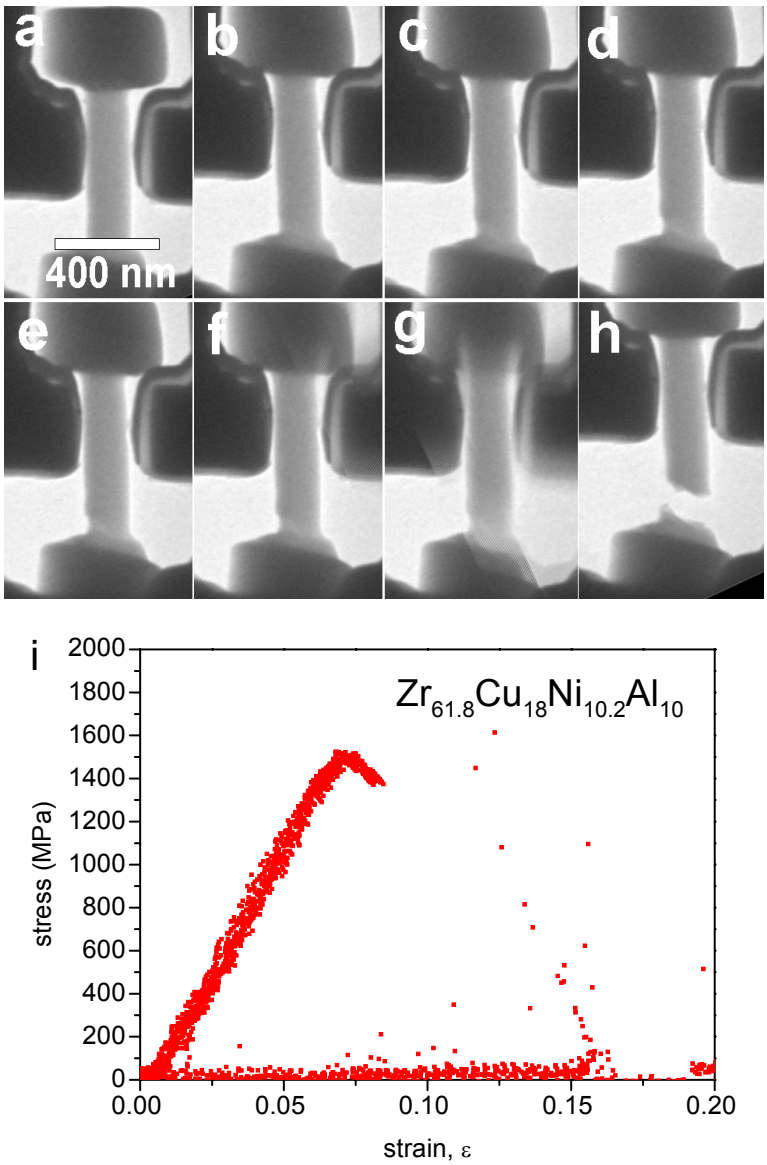

Fig. 6.8. Video frames recording the deformation of rectangular specimen (with dimensions 60 × 266 nm) of $Zr_{61.8}Cu_{18}Ni_{10.2}Al_{10}$ MG in tension at displacement rate controlled mode. Grabbed video frames show the deformation structures before, during and after tension (a-h). True stress-strain curve (i).

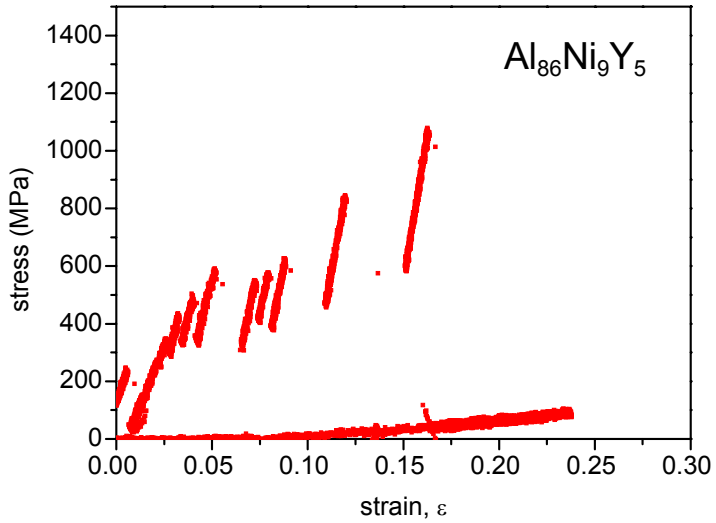

Fig. 6.9. True stress-strain curve of$Al_{86}Ni_9Y_5$ MG specimen of ø 200 nm in tension at displacement rate controlled mode.

Fig. 6.9 shows that another specimen does not exhibit the usual tensile behavior, i.e. release of intermittent shear bands and hardening effects (Fig. 6.9). Major fracture for this specimen has occurred at different places where smaller shear bands are released. Some of the shear bands released at the surface (Fig. 6.9). This is consistent with our compression experiments (Fig. 6.10). With increasing volume under compression the interaction between STZs has a larger chance to occur which leads to the build up and propagation of larger shear bands.

The comparison of stress level in compression and tensile experiments for two different compositions $Al_{86}Ni_9Y_5$ and $Zr_{61.8}Cu_{18}Ni_{10.2}Al_{10}$ MGs is displayed in Fig. 6.11. At both compositions there is no size effect of the yield stress observed, i.e. the same in tension and in compression. However both compositions show strain hardening upon reducing the specimen size (Fig. 6.11 (black curves)) under tension. There are several differences between the materials: Al-based specimens harden more than Zr-based, almost up to the same ultimate strength as for the bulk.

Both the tensile and compressive stresses increase the number of interactions among STZs. The specimens possess the same apparent Young's modulus under tension and compression. However, the experiments show that ultimate strength under tension is higher than under compression.

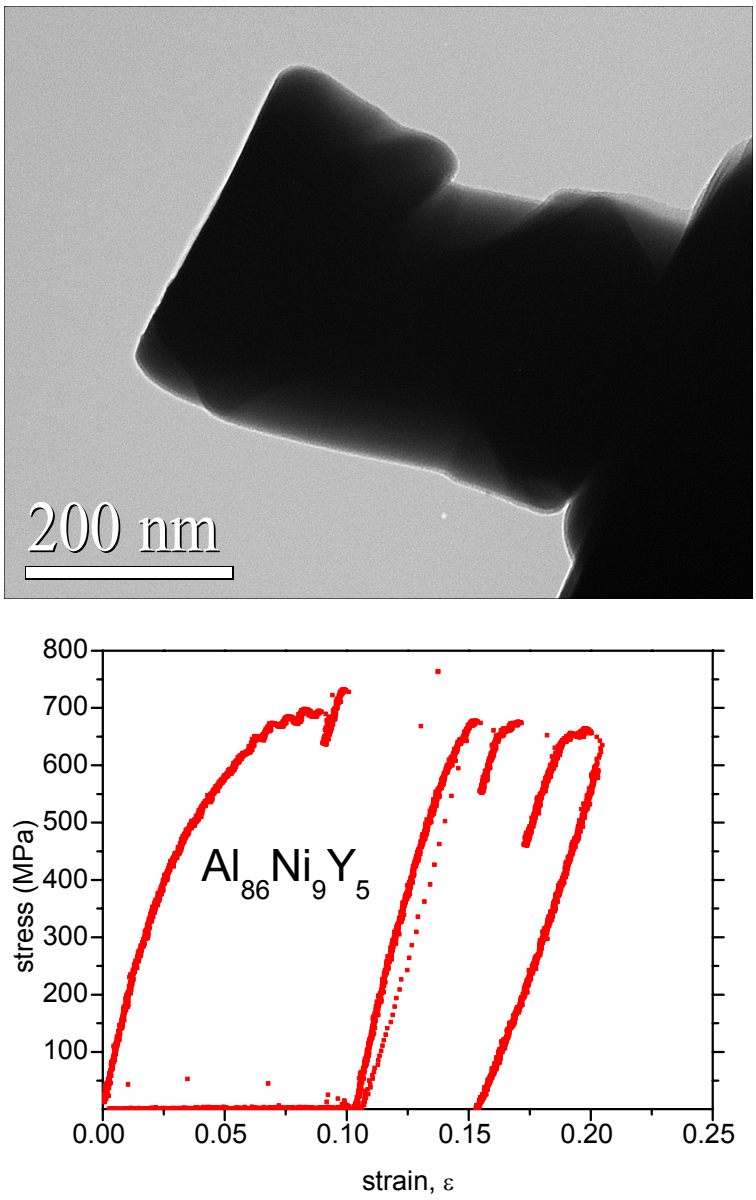

Fig. 6.10. Top: TEM picture of $Al_{86}Ni_9Y_5$ MG specimen of ø 250 nm in compression at displacement rate controlled mode; below: True stress-strain curve.

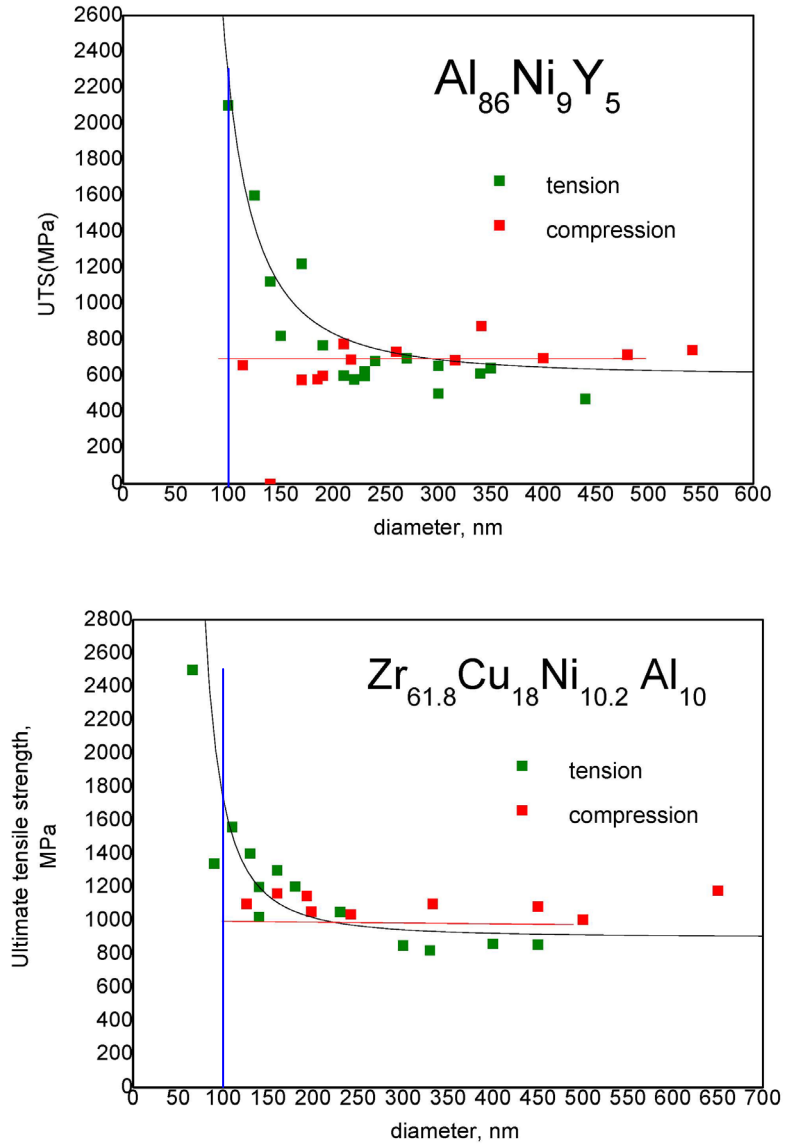

Fig. 6.11. Ultimate tensile stress vs pillar diameter of $Al_{86}Ni_9Y_5$ MG (a) and $Zr_{61.8}Cu_{18}Ni_{10.2}Al_{10}$ MG (b). Black curve indicates the hardening size effect, red graph refers to -yield stress.

In our explanation of the asymmetry between tensile and compression experiments the stress state of the starting material plays a predominant role. Generally speaking, in making comparisons between the mechanical performance of materials it is of utmost importance to know precisely the

residual stress state at the start of an experimental test, under compression as well as under tension. In this regards, the effect of ion irradiation caused by FIB in the preparation stage of specimens has to be considered.

Obviously, the influence of irradiation is increasing with decreasing size of the specimen, since the ratio $2d_{Ga}/d$ (where constant d_{Ga} is the penetration depth of Ga ions) is increasing upon decreasing the diameter d. For the smaller diameters $2d_{Ga}/d$ is reaching values equal to 1/4 or more and the outer layer will be under compression. Therefore it is important to include the influence of the FIB ion layer for the smaller specimens. The negative compressive stress of the outer layer will generate an offset for the positive applied stress under tension. The ultimate tensile stress will therefore increase upon decreasing diameter as experimentally observed. One would expect also an offset under compressive loading, i.e. a decreasing peak stress upon decreasing diameter. This was not really observed in practice because of the experimental difficulties to perform reliable compression tests on pillars with 1 free-end and diameters smaller than 100 nm. More experimental efforts are needed to clarify this point.

Fig. 6.11 shows a considerable difference between the UTS values of $Al_{86}Ni_9Y_5$ MG and $Zr_{61.8}Cu_{18}Ni_{10.2}Al_{10}$ MG upon decreasing size. The difference is about a factor of 2, i.e. much larger for $Al_{86}Ni_9Y_5$ and $Zr_{61.8}Cu_{18}Ni_{10.2}Al_{10}$, say roughly 1500 MPa for $Zr_{61.8}Cu_{18}Ni_{10.2}Al_{10}$ and 2500 MPa for $Al_{86}Ni_9Y_5$ at a diameter of 100 nm and the question is whether we can understand these differences in a more quantitative sense.

Our starting hypothesis is the mean projected range of defects induced by the FIB treatment that may affect the UTS. It is worth noting that thermal or charge-based effects are discarded here: in a transmission electron microscope thermal and charge conditions could surpass the FIB in intensity but no deformation was observed during static observations. Therefore the explanation is caused by the presence of defects introduced into the material during ion milling pre-treatment and the subsequent knock-on effects produced as ions traveled within the material.

Stopping Range of Ions in Matter (SRIM, version 2012.03,[16]) simulations allow us to see the effects of ions impinging upon a solid target. A typical result for SRIM of a material like Al exposed to a perpendicular 30kV Ga ion beam shows a projected damage range of 20 nm. Depending on the material, each ion generates an approximately fixed number of defects, the shape of the ion penetration distribution is then the same as the shape of the

distribution of defects created through ionic knock-on effects. The defect distribution induced can be modeled as symmetrical and triangular [17]

We take the stress σ and strain ε interrelated by linear elasticity and we relate the stress formed in the defect-rich region to the strain via the modulus E and Poisson's ratio ν:

$$\sigma(z) = \frac{E}{1-\nu} \cdot \varepsilon(z) \tag{6.1}$$

During ion exposure various types of defects will be formed. In a crystalline case it is easier to identify these defects as vacancies, self-interstitials and Ga defects. We can express the contribution of defects to strain as linear, and thus take the sum of each type of defect of concentration $C_{d_i}(z) = n_i / n$ and atomic volume Ω_i.

$$\varepsilon_d = \frac{1}{3} \sum_i \frac{\Delta\Omega_i}{\Omega} \cdot C_{d_i}(z) \tag{6.2}$$

where n_i / n is the number of defects over number of all lattice sites, where *i*, refers to the various defects like vacancies, interstitials and Ga+ defects, and $\Delta\Omega_i / \Omega$ refers to the relative volume change due to specific kind of defect *i*. Obviously in an amorphous system the reference state is not crystalline but a state of random disorderness. Therefore the damage cascade will be less localized due to less focused knock-on collisions as it will be in the crystalline state.

To predict $C_{d_i}(z) = n_i / n$ we take the displacement energy term E_d of a metal in the Kinchin-Pease equation that relates accelerated ion energy E_a to the amount of defects formed through E_d.

$$n_d = \frac{E_a}{2E_d} \tag{6.3}$$

E_d is mostly measured empirically, and a large amount of literature is available on experiments to measure E_d of various materials[18], e.g. using displacement energies of 16eV for Al the approximate amount of defects formed by a single ionic impact at 30kV is 1000. If we estimate the ion emission parameter of the FIB apparatus used at $2.08 \cdot 10^7$ ions per second to achieve an ionic current of 10pA, we can state that approximately $2 \cdot 10^{10}$ defects in crystalline aluminum would be generated. At low to medium dose the number of defects goes linear with the fluence.

With n_d taken from Eq. (6.3) and substituting its value into Eqs. 6.1 and 6.2 it seems rather trivial to predict the residual stress. However, there is at least one snake. The contribution of defects to the total strain/stress is assumed to be linear. The stress field of a *single* defect in an infinite linear elastic solid can be calculated based on the theory presented already 70 years ago by Love [19] and to date it can be done through atomistics. The latter predicts a stress of 0.18 MPa of a single defect in crystalline Al based alloy on the Daw-Baskes Embedded Atom Method (EAM) [20]. This would lead to an unrealistic high stress state and you may ask yourself: what is wrong here and where is the snake? The answer lies in the actual distribution. For a *uniform* distribution of defects in a *linear elastic medium*, the material will expand/contract uniformly leading to a stress-free material (assuming no other boundary conditions and constraints, e.g. surfaces etc). For a linear elastic solid this was worked out by 'Jock' Eshelby [21] assuming a homogeneous distribution and for a non-linear elastic solid surprisingly enough only recently. [22] The effective n_d for a triangular distribution and including a free surface is only 1% of the number predicted by the Kinchin-Pease equation.

Now we are in the position to make a fair estimate of the residual stress and to check our hypothesis concerning the increase of UTS upon decreasing size as displayed in Fig. 6.11.

In the milling process it is reasonable to estimate that only 15% of the Ga ions will impinge the surface perpendicularly. Therefore the effective dose is 4×10^{19} ions m^{-2} and based on Kinchin-Pease equation each incoming ion will generate for the stress build-up effectively: $0.015\times1000\times4\times10^{19} = 6\times10^{20}$ defects m^{-2} for $Al_{86}Ni_9Y_5$ MG and 3×10^{20} for $Zr_{61.8}Cu_{18}Ni_{10.2}Al_{10}$ (melting points and cohesive energies of Zr and Al differ a factor of 2). With a projected range of 20 nm at 30 kV Ga^+ and the external dimensions of the experimental pillars (diameter 100 nm, length 300nm) the effective strain build-up is 0.013 in $Al_{86}Ni_9Y_5$ MG and 0.007 in $Zr_{61.8}Cu_{18}Ni_{10.2}Al_{10}$, taking into account that the density of amorphous systems is about 0.9 of crystalline materials systems and a volumetric change of 12% being the average with respect to Ga.

Based on these data and the elastic moduli and Poisson's ratio as listed in Table 4.1 ($E = 57.10^9$ Pa, $\nu = 0.384$ for $Al_{86}Ni_9Y_5$; for $Zr_{61.8}Cu_{18}Ni_{10.2}Al_{10}$ $E = 84.10^9$ Pa, $\nu = 0.377$) we estimate an increase of the UTS in pillars with diameter of 100 nm due to a compressive stress of 2.6 GPa in $Al_{86}Ni_9Y_5$ and 1.3 GPa in $Zr_{61.8}Cu_{18}Ni_{10.2}Al_{10}$ which turns out to be in fair agreement with experiments (Fig. 6.11).

This analysis provides support to our hypothesis that residual stresses play an important role in the UTS value of smaller sized pillars (range 100 nm in diameter). As expected, basically because of the difference in bond strength, the effects of residual stresses due to pre-treatment are more visible in Al-based than in Zr-based MG and therefore the ion irradiation effect has the largest impact onto the mechanical performance of smaller sized Al- based specimens under tension.

Likewise hardening under tension is expected because the interacting volume of the STZs is actually decreasing even more rapidly upon decreasing size and in fact confined due to the (relatively) increasing volume fraction of negative compressive stress. Indeed, for both MGs the larger the $d_{Ga}/2d$ ratio, the larger the hardening effect.

6.3 Conclusions

In summary, in-situ tensile tests of $Al_{86}Ni_9Y_5$ and $Zr_{61.8}Cu_{18}Ni_{10.2}Al_{10}$ MG specimens with diameters ranging between 100 and 500 nm show a predominant inhomogeneous flow characterized by shear banding. However starting at specimens with 120 nm in diameter, $Al_{86}Ni_9Y_5$ MG exhibits a change in deformation behaviour from brittle fracture to plastic behaviour and inhomogeneous plasticity of necking.

The influence of chemical composition on the transition threshold in the tensile experiments was also observed, in accordance with compression tests. $Zr_{61.8}Cu_{18}Ni_{10.2}Al_{10}$ MG still shows plasticity around 60 nm, which is confirmed by the localized plastic necking. The unique increase in strength and strain hardening was observed for smaller sized specimens in tension which is different compared to compression experiments with the same MG compositions.

The observations described in this Chapter 6 confirm our predictions about volumetric size effect of MGs at nanoscale and can be explained by the competition between the nucleation and propagation of STZs at different stress fields and volumes. The study shows that the asymmetry in compression-tensile experiments is due to the residual stress state caused by the FIB pre-treatment.

6.4 References

1. W. Klement, R.H. Willens, P. Duwez, Nature 187, 869–870 (1960).
2. R .D. Conner, R.B. Dandliker, W.L. Johnson, Acta Materialia.46 , 6089 (1998)
3. J. Th. M. De Hosson, Microscopy Research and Technique, 72, 250 (2009).
4. O.V. Kuzmin, Y.T. Pei, C.Q. Chen, J.Th.M. De Hosson, Acta Materialia 60, 889 (2012).
5. A.A. Konstantinidis, K.E. Aifantis, J.Th.M. De Hosson, Capturing the stochastic mechanical behavior of micro and nanopillars, Mat. Sci Eng. A, (2014), accepted and in press.
6. S. Xie, E.P. George, Intermetallics 16, 485 (2008).
7. H-J. Lee, T. Çağin, W.L. Johnson, W.A. Goddard III, Journal of Chemistry and Physics 119, 9858–9870 (2003).
8. O.V. Kuzmin, Y.T. Pei, J.Th.M. De Hosson, Scripta Materialia 67, 344-347 (2012).
9. C.J. Gilbert, V. Schroeder, R.O. Ritchie, Metallurgical Materials Transactions 30A, 1739 (1999).
10. H.-K Lee, B.-B. Jung, Y.-D. Kim, W.-B. Hwang, H.-C. Park, Materials Science Engineering A 527, 339-343 (2009).
11. J. Th. M. De Hosson, C. Q. Chen, Y. T. Pei, V. Ocelik, D. Matthews, TMS Annu. Meet. Exhib. (2010).
12. O.V. Kuzmin, Y.T. Pei, J.Th.M. De Hosson, Applied Physics Letters 98, 233104 (2011).
13. C. Volkert, A. Donohue, F. Spaepen, Journal of Applied Physics 103, 083539 (2008).
14. D.C. Jang, C.T. Gross, J.R. Greer, International Journal of Plasticity 27, 858 (2011).
15. C. J. Lee, J. C. Huang, T. G. Nieh, Applied Physics Letters 91, 161913 (2007).
16. J F Ziegler, M D Ziegler, J P Biersack, Nuclear Instruments and Methods in Physics Research Section B: Beam Interactions with Materials and Atoms, 268, (11–12), 1818-1823 (2010)
17. S. Punzhin , Performance of ordered and disordered nanoporous metals, PhD thesis, University of Groningen, (2013).
18. G H Kinchin, R S Pease, Rep. Prog. Phys. 18 1 (1955).
19. A.H. Love, Mathematical theory of elasticity, Cambridge, UK: Cambridge University Press, (1927).
20. M.S. Daw, M. Baskes, Phys. Rev. B 29, 6443 (1984).
21. J.D. Eshelby, J. Appl. Phys. 25, 255–261 (1954).
22. A. Yavari, A. Goriely, Proc. R. Soc. A 468, 3902–3922 (2012).

Chapter 7

Summary and outlook

7.1 Summary

Investigation of the mechanical behavior of materials is an important key topic in nanoscience and nanotechnology. Most of the nanodevices fail due to (thermo)mechanical processes and therefore fundamental questions about size effects in these nano-objects are very relevant. Also, mechanical testing at larger scales differs significantly differ from testing at smaller specimens and therefore size effects open a new potentially interesting area for investigations.

A metallic glass (MG) represents an exceptional class of materials which possesses rather unique properties for metals. It allows producing of large amount of stresses within the specimen, but it lacks the plasticity and undergoes shear band deformation rapidly. Therefore investigations of size effects in metallic glasses plays important role. The recent developments of nano- and microscale manufacturing processing techniques using e.g. focused ion beam or electron beam have significantly increased the importance of materials with homogeneous structures (Chapter 2). By applying FIB-based techniques, various specimens with smooth surfaces on a nanometer scale can be fabricated from MGs. Chapter 3 presents new in-house developed methods for the preparation of nanopillars, which enable to avoid FIB milling artifacts such as tapering and redeposition.

Size effects can be grouped into intrinsic or extrinsic. Intrinsic size effects are commonly controlled by the inner structure and materials processing. In MGs, they are represented by the collective behavior of(shear transformation zone) STZs (discussed in chapters 3 and 5). In-situ quantitative compression tests which revealed intrinsic and strong size effects of taper-free metallic glass nanopillars inside a transmission electron microscope (TEM) on different MG compositions show predominantly an inhomogeneous and intermittent plastic flow characterized by shear banding events. The deformation is defect-nucleation-controlled in larger pillars but

becomes propagation-controlled in smaller pillars. Pillars with a diameter smaller than a certain diameter show a homogeneous flow behavior without shear banding during compression.

The initial structure and chemical composition of MGs also affect the deformation behavior at the nanoscale (Chapter 4). MG pillars of different alloy systems and compositions, Cu-based, Al-based, Zr-based alloys showed the shift in transition threshold depending on the bulk modulus and Poisson's ratio which also were affecting the deformation mode and ductility of MGs at the nanoscale. Higher values of Poisson's ratio, and consequently lower values of the μ/B ratio of MG composition, lead to a more ductile behavior. The $Al_{86}Ni_9Y_5$ taper-free metallic glass showed the highest transition threshold for brittle behavior, i.e. above pillar diameter of 300 nm (discussed in Chapter 5).

In accordance with our predictions $Al_{86}Ni_9Y_5$ MG shows plastic deformation becoming even more apparent through softening and toughening effects. These phenomena are revealed and characterized through the cyclic micro- and nanopillar tests. The proposed experimental technique of loading and unloading cycles is capable of determining the mechanical performance in metallic glasses, and opens a new route to the characterization of the deformation behavior of metallic glasses down to 100nm sizes.

Extrinsic size effects as opposite to intrinsic are caused by dimensional constraints due to preparation methods or influence of preparation technique on the sample during or before mechanical testing. These extrinsic constraints arise due to geometry of the specimens, aspect ratio or they are influenced by the FIB interface layer. The pillar aspect ratio has a large influence on deformation behavior representing a clear extrinsic size effect. Very high strains and ductility were achieved in bending at high aspect ratios, which reveals a possibility for future application developments with MGs.

Interactions between intrinsic and extrinsic size effects in MGs are particularly interesting, although the current understanding of this topic is limited. As argued in Chapter 3, tapering is a serious problem in investigating the deformation behavior of micro-pillars under compression. Tensile experiments were performed in order to separate the difference between extrinsic and intrinsic size effects (Chapter 6). The transition threshold from inhomogeneous flow which is characterized by shear banding events is shifting compare to compression experiments towards a lower diameter of the specimens. It indicates the separation of volumetric extrinsic size effect which

was concluded by compression experiments and intrinsic size effects on MG composition which is related to collective behavior of STZs.

7.2 Outlook

Based on the tensile experiments on $Al_{86}Ni_9Y_5$ and $Zr_{61.8}Cu_{18}Ni_{10.2}Al_{10}$ MG samples many questions about the mechanical behavior of MGs at nanoscale could be properly addresses. The change in deformation behavior from brittle fracture to necking starts at samples in tension at smaller diameters in comparison to the compression. The influence of chemical composition on the transition threshold for both regimes was also observed. It confirms our predictions about volumetric size effect of MGs at nano-scale and can be explained by the competition between the nucleation and propagation of STZs at different stress fields and volumes.

Despite of the constant yield stress in compression, tensile experiments show unique increase in strength. Strain hardening was observed for smaller sample sizes in tension. However tensile experiments at the smallest scale revealed the influence of FIB ion irradiation on specimens and suggest that it plays also a role in appearance of extrinsic size effects of MGs in tension.

From a theoretical viewpoint an interesting question to address is the influence of statistics. In crystalline materials the stress-strain response of micropillars during compression is characterized by significant stochastic effects, which are manifested through multiple strain bursts [1,2,3,4]. The stress-strain curves for same diameter pillars differ significantly, however, they can be enclosed within bounds, and therefore a size effect is noted. Recently it has been shown that the stochastic effects observed in the stress-strain behavior of both crystalline and glassy micropillars are successfully captured by implementing a gradient formulation in a cellular automaton and using a stochastic term to characterize the yield stress [5,6,7] . The numerical code was able to interpret the stochastic stress-drops observed during nanopillar compression and the observed size-dependent strengthening as well. In particular for glassy materials, having a proposed internal self-averaging structure when no mechanical stress is applied, this approach dealing with stochastic effects is worthy to examine in further detail.

The term size effect is used to distinguish all the cases when materials change the properties by reducing the dimensions of the specimen. Nowadays, material technologies emphasize miniaturization. Nano-system fabrication and developments are a very interesting and challenging field of scientific

research bridging microelectronic, physics, chemistry, mechanics. Recent progresses have allowed highly integrated and high-performance micro- and nano- electromehanical devices and the further development of such systems depends critically on the choice of appropriate materials. In this regard, properties of metallic glasses at nanoscale are providing a significant and unique potential. Understanding mechanical properties of MGs at nanoscale is therefore a high impact issue of material research. The investigations on different compositions in tension and in compression should be addressed. With respect to the sizes it is interesting also to reveal the influence of initial MG structure and temperature treatments on the transition thresholds. In summary, potential applications of this research are feasible and it offers a bright prospective for future work in materials science.

References

1. D.M. Dimiduk, M.D. Uchic and T.A. Parthasarathy, Acta Mater. 53 (2005) 4065–4077.
2. J.R. Greer and J.Th.M. De Hosson, Progress in Materials Science 56 654–724 (2011).
3. K.S. Ng, A.H.W. Ngan, Acta Mater. 56 (2008) 1712–1720.
4. R. Maaß, S. Van Petegem, H. Van Swygenhoven, P.M. Derlet, C.A. Volkert, D. Grolimund, Phys. Rev. Lett 99 (2007)145505.
5. A.A. Konstantinidis, K.E. Aifantis, J.Th.M. De Hosson, Capturing the stochastic mechanical behavior of micro and nanopillars, Mat. Sci Eng. A, (2014), accepted and in press,
6. O.V. Kuzmin, Y.T. Pei, C.Q. Chen and J.Th.M. De Hosson, Acta Mater. 60 (2012) 889-898.
7. C.Q. Chen, Y.T. Pei, O. Kuzmin, Z. Zhang, E. Ma, and J.Th.M. De Hosson, Physical Review B 83 (2011) 180201

List of publications

1. O.V. Kuzmin, Y. T. Pei, and J. Th. M. De Hosson , In situ compression study of taper-free metallic glass nanopillars, Applied Physics Letters, 98,233104 (2011)
2. O.V. Kuzmin, Y.T. Pei, C.Q. Chen and J.Th.M. De Hosson, Intrinsic and extrinsic size effects in the deformation of metallic glass nanopillars, Acta Materialia, 60, 889-898 (2012).
3. C. Q. Chen, Y. T. Pei, O. Kuzmin, Z. F. Zhang, E. Ma, J. T. M. De Hosson,Intrinsic size effects in the mechanical response of taper-free nanopillars of metallic glass, Phys. Rev. B, B 83, 180201(R) (2011).
4. O.V. Kuzmin, Y.T. Pei and J.Th.M. De Hosson, Size effects and ductility of Al-based metallic glass, Scripta Materialia 67 (2012) 344–347
5. O.V. Kuzmin, Y.T. Pei and J.Th.M. De Hosson, Strain softening and size effects of Al-based metallic glass pillars, (submitted).
6. O.V. Kuzmin, Y.T. Pei and J.Th.M. De Hosson, Aspect ratio and sizeeffects of Al-based metallic glass pillars, (submitted).
7. O.V. Kuzmin, Y.T. Pei and J.Th.M. De Hosson, Fabrication method of nanopillars through focused ion beam cutting, (submitted).
8. O.V. Kuzmin, Y.T. Pei and J.Th.M. De Hosson, Size effects of MGs at nanoscale in tension, (in preparation).

Acknowledgements

With the hope on future and the greetings to the past I would like to start my acknowledgments. A lot of good and bad things happened during these years but anyway I'll never forget an unbelievable life experience which I've got while studying in Groningen. Thank you all for the GREAT support!

First I would like to say many thanks to my supervisor Professor Jeff De Hosson. Without your grateful and exhaustive help it wouldn't be possible. You gave a great chance and ticket to life which will remember forever. Every conversation with you was inspiriting me so much, that I could do anything with a lot of joy and pleasure and spend hours by doing and thinking. The new ideas about solving of different experimental and theoretical issues were just bubbling up over and over again. Your ability to inject an enormous amount of energy to any person who you talk to is amazing and deserves the best acknowledgements. Needless to say, that I am very grateful for your understanding and help when my road due to circuit of terrible incidents was coming to the end. Without your tolerance my graduation simply would not exist. I am proud that I was supervised by a brilliant scientist and a greatest person simultaneously. THANK YOU, JEFF!

I would like to gratefully acknowledge my co-promotor Dr. Yutao Pei. Thank you, Yutao, for your suggestions and ideas which were very helpful for our research. Thank you a lot for useful advises and your motivated attitude always inspired me to do great experimental work. Along the same lines equally I wish to thank to David and Anatoly, you were always helping me in any kind of problem despite of whether it is work related or not. Especially, many thanks to David for his support on every issue and for providing the best solution to any situation.

I wish to thank members of thesis reading committee Professors Hans de Raedt, Petra Rudolf, Beatriz Noheda for the careful reading and evaluation of my work.

I take this opportunity to express my gratitude to my teachers and supervisors during Master and Bachelor studies: Igor Girka, Sergey Litovchenko, Vladimir Semenenko, Mikhail Tihonoskiy, Alexey Velikodnuy, for the professional guidance, strong theoretical base and valuable experimental skills, which you have transferred to me.

I wish express special thank to Paul for his particular and intriguing interests to my research and very valuable help at lab. Your positive attitude

to life was always helping me to go further and further and do not give up if something went wrong. Together with you we've made plenty of perfect and published specimens.

I wish to thank Mikhail Dutka for his infinite help in any request I was needed. Again and again I was asking for help, and you were always open to support me. You've helped me to get out from every trap, where I was in, Спасибо Миша!

I wish to thank Sergey Punzhin and to his parents for their endless help and support outside the work. I am very much appreciate your sincerity and graciousness. Thank you for every hour we have spent together!

I thank all other MK group members past and present, including Willem van Dorp, Willem-Pier Vellinga, Chang Qiang Chen, Diego Martinez-Martinez, Leo de Jeer, Vašek Ocelík, Jiancun Rao, Eric Detsi, Enne Faber, Ismail Hemmati, Jozef Vincenc Oboňa, Ivan Furar, Catalina Mansilla-Sanchez, Huajie Yang, Xiaohong Shao, Kalpak Shaha, Elly Eekhof, Sriram Venkatesan, Ondrej Nenadl, Jin Tao Shen, Winand Slingenbergh, Alessio Morelli, Tony Kazantzis.

I am highly indebted to Pavel Symbyrev, the specialist in complex biomechanical rehabilitation, for giving me a second chance to live.

My life would not be possible at all without three people to whom I'm eternally thankful! You are the only ones who didn't betray me in the hardest times. First of all I would like to thank to my friend Alexandr Zinchenko, who I know already for more than ten years. The destiny is ordered so, that most of our time we have spent together. Your unbelievably enthusiastic position in conversations was sopping me from thinking about any problem I've had, I was smiling even when dying. I wish to express great thank to Alexandr Turkin, we spend a lot of pleasant times with you playing tennis, doing gym and what is the most important is thinking together. Thank you for the best crazy experiences in my life! Many thanks to my friend and beachvolleyball partner Mark Jan Paulusma, we had the best times with you on the field, however the real friendship can be checked only when disaster is coming, thank you for keeping my life vital even when it was hurting your health. Зин, Саша и Марк, моя бесконечная БЛАГОДАРНОСТЬ ВАМ! (Mark, de laaste zin moet je maar zelf vertalen !)

I wish to thank my friends who always were supporting me in life. Thank you, Dimon, I'll never forget the BEST times in my life which we've spent together. I've learned a lot from you and hope you'll teach me more future. Thank you, Dmitriy Mesheryakov, You always will be a "Толстый" for me!

Thank you Pedro, we have played a plenty amount of awesome balls together, bro!

Света, спасибо за поддержку, и за твою бесконечную веру и надежду на будущее, всегда беру пример с тебя! Никита и Олег, спасибо вам, ровняйтесь на маму.

Мои ДОРОГИЕ и ЛЮБИМЫЕ родители СПАСИБО Вам за Вашу любовь и непоколебимую веру в меня.